



POLITECNICO DI MILANO
DEPARTMENT OF ELECTRONICS, INFORMATION AND
BIOENGINEERING
DOCTORAL PROGRAMME IN COMPUTER SCIENCE

DEEP RECURRENT NEURAL NETWORKS FOR
VISUAL SCENE UNDERSTANDING

Doctoral Dissertation of:
Francesco Visin

Supervisor:

Prof. Matteo Matteucci

Co-Supervisor:

Prof. Aaron Courville

Tutor:

Prof. Andrea Bonarini

The Chair of the Doctoral Program:

Prof. Andrea Bonarini

2016 – XXVIII

All models are wrong, but some are useful.

GEORGE E. P. BOX

Abstract

Machine Learning (ML) is a fascinating field of research. In the era of knowledge, being able to find the right information in enormous amounts of data (e.g., the internet) and summarize it in a form that is compact and yet retains all the content one is interested in, is a key factor of success or failure in many fields. I am particularly interested in applying ML to vision problems because we, as humans, rely heavily on vision for our daily operations. Improvements in the technology at our disposal to interpret visual data can have a direct and remarkably rapid impact on many practical applications such as assist or automate driving, analyze medical images, aid surgeons in the operating room or improve the quality of life for visually impaired people. This manuscript presents my work on Recurrent Neural Networks (RNNs) and RNN-based models applied to visual data, describing three models I proposed, namely ReNet, ReSeg and DEConvLSTM. The first is an RNN-based alternative to Convolutional Neural Networks (CNNs) for object classification. The carefully designed interaction between the RNNs in the architecture allows the model to capture the full context of the image in just two levels of hierarchy as opposed to the many layers typically required by CNN-based models. The evolution of this model for semantic segmentation, called ReSeg, takes advantage of a similar inner structure as ReNet, further improved by the adoption of pretrained CNNs as well as the addition of transposed convolutional layers. Finally, the DEConvLSTM architecture addresses the much harder task of semantic segmentation in videos. To address this task I proposed a model that merges direct convolutions, transposed convolutions and RNNs in a unique coherent structure. The DEConvLSTM model exploits the speed of CNNs to process spatial information and the ability of RNNs to retain information through several steps of computation, and proved to be a valid architecture for video semantic segmentation. For each model, the architecture is first presented in detail, followed by a description of the experimental settings and of the datasets used for its evaluation. Results on publicly available dataset are compared to the state-of-the-art and discussed thoroughly.

Contents

1	Introduction	1
1.1	Main contributions	3
1.2	Outline	4
2	Background	5
2.1	Artificial neural networks	5
2.1.1	Brief history of neural networks	6
2.1.2	MultiLayer Perceptron	8
2.1.3	Activation functions	9
2.1.4	Backpropagation	12
2.2	Convolutional networks	15
2.2.1	Discrete convolutions	16
2.2.2	Pooling	19
2.2.3	Convolution arithmetic	22
2.2.4	No zero padding, non-unit strides	24
2.2.5	Zero padding, non-unit strides	25
2.2.6	Pooling arithmetic	25
2.2.7	Transposed convolution arithmetic	27
2.2.8	Convolution as a matrix operation	27
2.2.9	Transposed convolution	27
2.2.10	No zero padding, unit strides, transposed	28
2.2.11	Zero padding, unit strides, transposed	29
2.2.12	No zero padding, non-unit strides, transposed	31
2.2.13	Zero padding, non-unit strides, transposed	31
2.3	Recurrent networks	33
2.3.1	Long Short Term Memory	35
2.3.2	Gated Recurrent Unit (GRU)	39
2.4	Metrics	40

Contents

3 Recurrent Neural Networks for Object Classification	43
3.1 Motivation	44
3.2 Model Description	45
3.2.1 Differences between LeNet and ReNet	47
3.3 Experiments	48
3.3.1 Datasets	48
3.3.2 Data Augmentation	50
3.3.3 Experimental settings	51
3.3.4 Results	52
3.4 Discussion	52
4 Recurrent Neural Networks for Semantic Segmentation	55
4.1 Motivation	58
4.2 Model Description	59
4.2.1 ReNet layer	60
4.2.2 Upsampling layer	61
4.3 Experiments	62
4.3.1 Datasets	62
4.3.2 Data augmentation and preprocessing	64
4.3.3 Experimental settings	65
4.3.4 Results	66
4.4 Discussion	68
5 Convolutional RNNs for Video Semantic Segmentation	71
5.1 Motivation	72
5.2 Model description	73
5.2.1 Convolutional LSTM	74
5.2.2 Transposed Convolutional LSTM	76
5.2.3 Bidirectional RNNs	76
5.2.4 Skip Connections	77
5.3 Experiments	77
5.3.1 Datasets	77
5.3.2 Data augmentation and preprocessing	79
5.3.3 Experimental settings	80
5.3.4 Results	81
5.4 Discussion	84
6 Conclusion	87
Bibliography	91

CHAPTER **1**

Introduction

I am convinced that machines can and will think. I don't mean that machines will behave like men. I don't think for a very long time we are going to have a difficult problem distinguishing a man from a robot. And I don't think my daughter will ever marry a computer. But I think that computers will be doing the things that men do when we say they are thinking. I am convinced that machines can and will think in our lifetime.

— The Thinking Machine (Artificial Intelligence in the 1960s),
O. SELFRIDGE (LINCOLN LABS, MIT)

The dream of machines that can think and act as substitutes for humans in their jobs dates back to the '60s, if not before. We are still not at that point, although in the last decade the field experienced outstanding advancements and has been the object of increasing interest.

Artificial Intelligence (AI) is a broad field that aims to develop intelligent software that can for instance acquire knowledge from its interaction with the world, find optimized strategies for problem solving, automate tasks, detect patterns in audio, video and textual data, play games, drive cars and much more. Machine Learning (ML), a subset of artificial intelligence, set the state-of-art in many fields, such as e.g., image classification (Krizhevsky *et al.*, 2012a; Szegedy *et al.*, 2016; Visin *et al.*, 2015), semantic segmentation (Chen *et al.*, 2015; Visin *et al.*, 2016), video understanding (Srivastava *et al.*, 2015a; Xu *et al.*, 2015), natural language processing and machine translation (Bahdanau *et al.*, 2014). Much of this research already led to commercial products we use every day, such as e.g., speech recognition and speech synthesis in phones, face detection in cameras

Chapter 1. Introduction

and social networks, or traffic signs enhancement in cars. Even more impressively, a ML algorithm recently won several games of go (Silver and Hassabis, 2016) – a game known for being extremely challenging – against one of the best human players.

Despite its many successes, machine learning is no lamp genie that can tackle any problem by simply providing it with enough data. To get results in machine learning requires a meticulous analysis of the characteristics of the problem, clever architecture modelling, smart engineering, as well as careful inspection of complex and extremely nonlinear compositions of transformations. Most of all, it requires good organization, intuition and patience, since many of the experiments can last days if not weeks – even on big clusters of GPUs.

Many areas of research could benefit from the application of machine learning techniques, I chose to focus my research on visual scene understanding. My claim is that understanding a visual scene – be it an image or a video – requires capturing the scene semantics, and that this has to be done by building an incremental representation of the context while processing the elements of the observed environment scene. For this reason I decided to focus on Recurrent Neural Networks (RNNs), a family of neural networks with memory – or state – that can decide autonomously when to store, retrieve or delete information from their memory.

As a first step to address the problem of image understanding, I focused on object classification, i.e., the problem of selecting the class an object in a scene belongs to. Historically, this problem was addressed by hand-engineering global and local descriptors as characteristic as possible, so that their presence or absence could be used as a proxy for the presence or absence of a specific class of objects. From 2012 onwards, handcrafted methods were abandoned in favour of convolutional neural networks (CNNs), after the CNN-based model presented in (Krizhevsky *et al.*, 2012a) improved the state of the art by 10%. Since then, CNNs-based models dominated the object classification panorama.

In (Visin *et al.*, 2015) I presented ReNet, an alternative to the ubiquitous CNNs for object classification. The model is based on 4 RNNs that scan the image in 4 directions. RNNs have the potential to store in their memory any information that is relevant to retain the context of the part of the image they have seen up to that moment. The first two RNNs scan each line of the image reading one pixel (or patch, depending on the configuration) at a time from left to right and from right to left, respectively. The two resulting feature maps (i.e., output of each of these RNNs) are concatenated in each position over the channel axis, yielding a composite feature map where each position has information on the context of the full row as, in each position, it is a concatenation of an RNN reaching the position from the right and of an RNN reaching the same position from the left.

The second two RNNs sweep over the composite feature map vertically, top-down and bottom-up respectively. By reading the composite feature map, each RNN has access in each position to a "summary" of the corresponding row. Once again, the two feature maps are concatenated, resulting in a final feature map where each position is specific to a pixel (or patch) of the image but has information on the full image. The ReNet architecture allow us to capture the full context of the image with just one layer (to be fair, two sublayers), as opposed to CNN based architectures that would need many layers to span the entire image. As usual, it is still possible to stack multiple ReNet layers to increase the capacity of the network. ReNet obtained comparable results to the CNN state-of-the-art on three widely used datasets.

Encouraged by the results of ReNet and the positive feedback from the scientific community, I worked on a second model based on ReNet, to perform fine-grained object segmentation (i.e., to classify each pixel of the image as belonging to a specific class). Being able to classify objects without losing information on their position in the image can be exploited to allow very precise pixel-level object localization, which is essential to many applications and to a proper understanding of the image.

ReSeg (Visin *et al.*, 2016) takes advantage of the inner structure of the ReNet layers that, in contrast to classical convolutional models, allows the propagation of information through several layers of computation, retaining the topological structure of the input. To speed up training, the image is first preprocessed with a CNN pretrained on big datasets for object classification, to extract meaningful features and exploit the extra training data. Those rich features are then processed by several ReNet layers. However this results in an intermediate feature map that has a smaller resolution than the image. To be able to classify each pixel, the original resolution has to be recovered. Thus, one or more transposed convolutional layers (Dumoulin and Visin, 2016) upsample the feature map to the desired size. ReSeg obtained state-of-the-art on three datasets and was selected for the best paper award at the DeepVision Workshop at CVPR 2016. Furthermore, an extended version of this work will become a chapter of the upcoming book on the CVPR 2016 DeepVision Workshop.

The natural next step in the direction of visual scene understanding is the processing of videos to exploit the temporal correlation between frames and improve the performance of the algorithm. It is not trivial to work with videos in the domain of semantic segmentation: big enough dataset are still lacking due to the very high cost of labelling each pixel of each frame of a video; in many cases labels are imprecise and noisy, or missing a well defined semantic (e.g. the classes "porous" and "vertical mix" of the Gatech dataset described in Section 5.3.1) are difficult to define unequivocally, which makes learning harder. Still, it is a challenging but important problem to tackle and there seems to be room for improvement with respect to the current state of the art on the path traced by ReSeg. The proposed model combines the benefits of CNNs – namely the exploitation of the topological structure in the images and the processing speed – and the ability to retain temporal and spatial context information of RNNs. The idea builds on (Xingjian *et al.*, 2015) that introduced an RNN model whose internal state is convolutional. We improved on the original model by stacking several convolutions inside the RNN state (as opposed to only one) and by introducing a *deconvolutional RNN*, whose state is a stack of multiple transposed convolutions. This model achieved so far comparable results with the state-of-the-art on one datasets and encouraging results on two others.

1.1 Main contributions

The main contribution of my research have been the analysis of RNN-based models in the context of visual data. The ReNet model proved to be an effective alternative to the ubiquitous CNNs for object classification and drew the attention of the research community. The subsequent ReSeg model tackled with success the much harder problem of semantic segmentation, where a fine-grained understanding of the image structure has to be gained. This paper was selected at the CVPR 2016 DeepVision Workshop for the best paper award and will be expanded with a more in-depth analysis of the properties of the architecture in a

Chapter 1. Introduction

chapter of the upcoming book on the CVPR 2016 DeepVision Workshop. Finally I moved to the analysis of videos for dense segmentation, a very challenging task characterized by a high computational burden and scarce amounts of labeled data. To address this task I proposed a model that merges direct convolutions, transposed convolutions and RNNs in a unique coherent structure. The DEConvLSTM model proved to be a valid architecture for video semantic segmentation, pairing the state of the art on one of the historically most used datasets on this task and achieving encouraging results on two other dataset with just cursory exploration.

1.2 Outline

The rest of this manuscript is organized as follows:

- Chapter 2: introduces the most important models and concepts needed to understand the work done;
- Chapter 3 introduces the problem of object classification and describes in detail the ReNet model and its results;
- Chapter 4 defines what is referred to as semantic segmentation and how ReSeg tackles that problem;
- Chapter 5 moves to video understanding and specifically the task of video semantic segmentation and highlights the advantages of convolutional-deconvolutional RNNs in this context;
- Chapter 6 summarizes the main contribution of this research and proposes some of the many possible future directions of research that can build on top of this work.

CHAPTER 2

Background

Machine learning is a complex subfield of AI that witnessed a very quick expansion in the recent years. It aims to enable computers to *learn* how to tackle problems by detecting patterns and regularities in the training data and trying to generalize this extracted knowledge to new, unseen data. Among its many powerful tools, artificial neural networks are models that take inspiration from what is known about the human brain, by mimicking its connectivity patterns, learning rules and signal propagation, under the constraints imposed by our limited knowledge of the brain and the intrinsically different "hardware" at our disposal.

While it is beyond the scope of this document to give a formal and in-depth introduction to every concept needed to fully comprehend machine learning, the following sections will introduce Artificial Neural Networks (ANNs), with a specific focus on two of the most used kinds of neural networks i.e., Convolutional Neural Networks (CNNs) and Recurrent Neural Networks (RNNs). The interested reader can find a more detailed overview of machine learning and of its subfield deep learning in the books by Bishop (2006) and Goodfellow *et al.* (2016) respectively.

2.1 Artificial neural networks

Biological brains are composed by a large number of simple elements, called neurons, that are highly interconnected. The number of neurons in the human brain is estimated to be around 10^{11} , each one connected to a little less than 10^4 other neurons, resulting in a total between 10^{14} and 10^{15} synapses (Drachman, 2005). The activity of each of these either excites or inhibits the surrounding neurons it is connected to, generating a complex

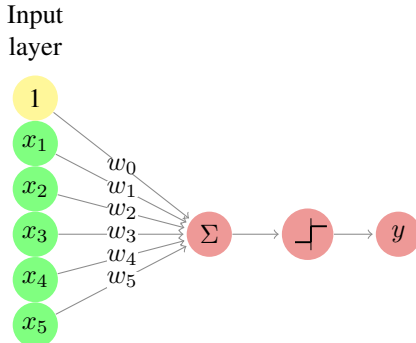


Figure 2.1: A representation of the Perceptron.

network of interactions. Artificial Neural Networks (ANNs) take inspiration from this understanding of the human brain, building networks composed of many artificial neurons, small elements that perform very simple operations on their inputs.

2.1.1 Brief history of neural networks

In 1943 McCulloch and Pitts defined a mathematical model of how a biological neuron works (McCulloch and Pitts, 1943). The artificial neuron they proposed was able to solve simple binary problems, but did not learn. In 1949 Hebb (1949) suggested that humans learn by enhancing the neural pathways between neurons that collaborate, and weakening the others. Only a decade later this learning rule inspired the Perceptron (see Figure 2.1), the first ANN that was able to vary its own weights, i.e., to find the setting that allowed it to exhibit the desired behavior (Rosenblatt, 1957).

The activation rule of the perceptron is very simple and is at the base of many modern neural networks. Given an n -dimensional input $\mathbf{x} = (x_1, \dots, x_n)$, the weighted sum of each dimension of the input x_i and its associated weight w_i is computed as

$$z = \sum_{i=1}^n (w_i \cdot x_i) + b,$$

where the weight w_i is often referred to as *preactivation* and to simplify the notation the bias term b will often be replaced by an equivalent input term $x_0 = 1$ weighted by $w_0 = b$. Note that this is simply the dot product of the weight vector $\mathbf{w} = (w_1, \dots, w_n)$ and the input vector \mathbf{x} . The result of this first affine transformation is then passed through a step function of the form

$$y = \begin{cases} 1, & \text{if } z \geq 0, \\ 0, & \text{otherwise,} \end{cases}$$

that determines the binary output of the Perceptron.

This can be used, for instance, to classify whether the input belongs to a specific class or not. Note that the model can be easily extended to handle multiple classes, by simply adding more dimensions to y and assigning each of them to a different class.

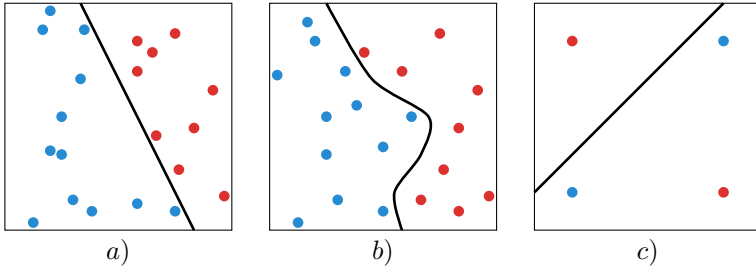


Figure 2.2: a) A linearly separable problem. b) A nonlinearly separable problem. c) The XOR problem with a tentative solution that fails at separating the points of the space.

The behavior of the Perceptron is indeed remarkable, but the biggest innovation of Rosenblatt (1957) is most probably the update algorithm that allowed one to modify the weights of the model. Given a training pair (\mathbf{x}, y) consisting of an input and its corresponding desired output, the weights and the bias – also called the *parameters* of the network – are *learned* according to the following rule:

$$w_i^{\text{new}} = w_i^{\text{old}} - \eta \cdot (\hat{y} - y) \cdot x_i, \quad (2.1)$$

where \hat{y} is the output of the Perceptron, y is the target (i.e., desired) value, x_i and w_i^{old} are respectively the i -th input and weight at the previous iteration and η is a scaling factor that allows to adjust the magnitude by which the weights are modified.

The introduction of a model that could learn from data was welcomed with excitement as the beginning of a new era and research in ANNs became very active for approximately a decade, until in 1969 Minsky and Papert published a detailed mathematical analysis of the Perceptron, demonstrating that a single layered Perceptron could not model basic operations like the XOR logic operation (Minsky and Papert, 1969). The limit of Perceptrons is that they can only solve linearly separable problems, and fail at tackling nonlinearly separable problems like the XOR (see Figure 2.2). This is not the case for Multi-Layer Perceptrons (MLP, depicted in Figure 2.3), an evolution of Perceptrons that introduces one or more intermediate layers (called *hidden layers*) between the input and the output. Since in each of these layers the preactivation is followed by a nonlinearity, the result is a nonlinear transformation that can project the input into a linearly separable space.

The excessive enthusiasm for the early successes of ANNs turned into strong disappointment: even if Minsky and Papert (1969) showed that an MLP could model the XOR bitwise operation, they also pointed out that Rosenblatt's learning algorithm was limited to single layered Perceptrons and could not autonomously learn how to solve the problem. The expectation of an artificial intelligence that could learn by itself to solve problems and interact with humans appeared suddenly unrealistic and most of the research community lost interest in ANNs. The field experienced a severe slow down and most of the fundings were cut.

After a decade known as the first AI Winter, in 1982 John Hopfield presented a model of human memory that did not only give insights on how the brain works, but was also useful in practical applications and had a sound and detailed mathematical grounding. At the same time, at the US-Japan Joint Conference on Cooperative/Competitive Neural

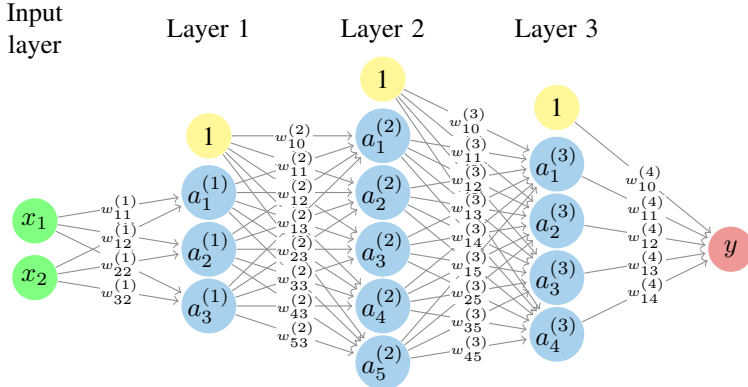


Figure 2.3: A MultiLayer Perceptron. The sum and the nonlinearity nodes have been omitted for the sake of clarity.

Networks, Japan announced a renewed effort in building neural networks and the fear that the US might be left behind renewed their effort on this topic.

The breakthrough that completely restored the interest in the field came in 1986, when Rumelhart *et al.* (1986a) rediscovered the backpropagation algorithm (Linnainmaa, 1970; Werbos, 1974) that allowed to train ANNs composed by multiple layers by performing gradient descent (see Section 2.1.4). However once again the expectation was set too high and AI was expected to allow to do things like translating languages, carrying on conversations and interpreting pictures. In late 80s and early 90s AI fundings were cut again when those very high demands had not been attended.

Despite that, many researcher were convinced by then of the potential of AI and kept working on it. By 2006 ANNs established the state of the art in many official international competitions in several domains, attracting again attention and fundings. Since then, they have been constantly the focus of study and innovation.

2.1.2 MultiLayer Perceptron

Consider the network in Figure 2.3. As opposed to the Perceptron in Figure 2.1, the MLP has multiple hidden layers, where each neuron of one hidden layer is connected to all the neurons of the previous and the next layer. Each connection from the i -th neuron of layer $l - 1$ to the j -th neuron of layer l is associated to a weight $w_{ij}^{(l)}$, and all the weights are stored in a matrix $\mathbf{W}^{(1)}$.

Similarly to the Perceptron case, each layer computes an affine transformation

$$\mathbf{z}^{(l)} = \mathbf{W}^{(l)} \cdot \mathbf{a}^{(l-1)}, \quad (2.2)$$

followed by a nonlinearity σ – usually more smooth than the one used in the Perceptron – called *activation function*

$$\mathbf{a}^{(l)} = \sigma(\mathbf{z}^{(l)}). \quad (2.3)$$

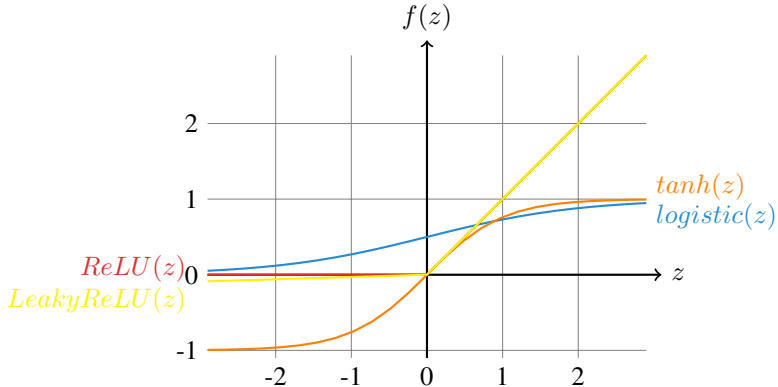


Figure 2.4: Some of the most common activation functions: sigmoid, tanh, ReLU and LeakyReLU. ReLU and LeakyReLU are overlapping for $z \geq 0$. Best viewed in colors.

One hidden layer can thus be seen as a function $h^{(l)}$ that depends on some *parameters* specific to that layer – namely a matrix of weights $\mathbf{w}^{(l)}$ and the bias vector $b^{(l)}$ – as well as some *hyperparameters*, such as the number of neurons and the choice of activation function. It is common to denote the set of trainable parameters that fully characterize a layer as $\theta^{(l)}$.

The processing performed by the hierarchy of layers of the MLP results in the output vector \mathbf{y} and is equivalent to a composition of multiple functions

$$\mathbf{y} = h_{\theta}^{(L)} \circ h_{\theta}^{(L-1)} \circ \dots \circ h_{\theta}^{(1)}. \quad (2.4)$$

Although very common and widely used, the MLP is not the only architecture for ANNs. In Section 2.2 and Section 2.3 two of the most used alternatives will be described.

Generally, each layer of an ANN computes some activation based on its input and a nonlinear activation function. The choice of which activation function to use in each layer can have a big impact on the performance of the model and is sometimes constrained by the semantic assigned to the output of some units. The most important activation functions will be introduced in the following section.

2.1.3 Activation functions

The activation function is one of the most important component of an ANN. As explained in the previous sections, to tackle nonlinearly separable problems it is imperative to map the input into a space that is linearly separable. The activation function does this by performing an *element-wise nonlinear transformation* of the pre-activation that comes from the affine transformation.

The affine transformation and the nonlinearity work together in a very tight interaction: the latter is fixed and does not evolve during training, but maps its input to a different space in a (usually highly) non-linear way; the former, is determined by the weights that are learned during training and exploits the latter to map the incoming activation into a new space where they are easier to separate. In addition to this it is interesting to point out that

Chapter 2. Background

if there was no activation function, since the composition of multiple affine transformation is an affine transformation, the layers of the MLP could be replaced by a single equivalent layer, and the MLP would become a Perceptron.

Many activation functions have been proposed in the years and even if our understanding of this component has improved, which one to use with the different architectures and tasks is still the object of active research.

Logistic

The logistic, often called *sigmoid*, is a differentiable monotonically increasing function that takes any real-valued number and maps it to $[0, 1]$. As evident from its representation in Figure 2.4, for large negative numbers it asymptotes to 0 while for large positive numbers it asymptotes to 1. It is defined as

$$\text{logistic}(\mathbf{z}) = \frac{1}{1 + \exp(-\mathbf{z})}. \quad (2.5)$$

The logistic function has probably been the most used nonlinearity historically due to its possible interpretation as the firing rate of a neuron, or its probability to fire, given its potential (i.e., the level of excitement provoked by its incoming spikes): when the potential is low the neuron fires less often whereas when the potential is high the frequency of the spikes increases.

Another very important property of the logistic function is that it is very fast to compute its derivative, once solved analytically:

$$\begin{aligned} \frac{\partial}{\partial \mathbf{z}} \text{logistic}(\mathbf{z}) &= \frac{\exp(-\mathbf{z})}{(1 + \exp(-\mathbf{z}))^2}, \\ &= \frac{1}{1 + \exp(-\mathbf{z})} \cdot \frac{\exp(-\mathbf{z})}{1 + \exp(-\mathbf{z})}, \\ &= \text{logistic}(\mathbf{z}) \cdot \frac{\exp(-\mathbf{z})}{1 + \exp(-\mathbf{z})}, \\ &= \text{logistic}(\mathbf{z}) \cdot \frac{1 + \exp(-\mathbf{z}) - 1}{1 + \exp(-\mathbf{z})}, \\ &= \text{logistic}(\mathbf{z}) \cdot \left(1 - \frac{1}{1 + \exp(-\mathbf{z})}\right), \\ &= \text{logistic}(\mathbf{z}) \cdot (1 - \text{logistic}(\mathbf{z})). \end{aligned} \quad (2.6)$$

The use of the logistic function is not as widespread as it used to be though, due to two major drawbacks:

- *Saturation kills the gradient*: backpropagation (see Section 2.1.4) relies on the gradient of the error to determine the parameters update. The logistic function saturates at both ends, resulting in a very small or zero gradient. This problem – often referred to as *vanishing gradient* – makes training very slow or prevents it in some cases. This also makes the logistic units very sensitive to the initialization of the weights of the network, that ideally should be such that the initial input of the logistic function is close to zero.

- *The output is not zero-centered:* the dynamics of ANNs are usually complex and difficult to inspect, but it is widely believed that normalizing the intermediate activations of the network (i.e., to zero-center their mean and impose unit variance) helps training (Ioffe and Szegedy, 2015; Laurent *et al.*, 2015; Arpit *et al.*, 2016; Cooijmans *et al.*, 2016). The output of the logistic function is always positive, which causes the mean activation to be non-zero. This could introduce undesirable dynamics that could slow down or prevent training.

Hyperbolic tangent (\tanh)

The hyperbolic tangent, typically shortened as \tanh , is a differentiable monotonically increasing function that maps any real-valued number to $[-1, 1]$. This nonlinear function suffers from the same vanishing problem as the logistic, but its mean is centered in zero. Furthermore, the \tanh is often chosen where it is desirable to be able to increase or decrease some quantity by small amounts, thanks to its codomain. It is defined as

$$\tanh(\mathbf{z}) = \frac{1 - \exp(-2\mathbf{z})}{1 + \exp(-2\mathbf{z})}. \quad (2.7)$$

Rectified Linear Unit (ReLU)

Since its introduction, the Rectified Linear Unit (ReLU) (Jarrett *et al.*, 2009; Nair and Hinton, 2010) has become the nonlinearity of choice in many applications (Krizhevsky *et al.*, 2012a; LeCun *et al.*, 2015; Glorot *et al.*, 2011). It is defined as

$$relu(\mathbf{z}) = \max(0, \mathbf{z}). \quad (2.8)$$

Although very simple, it has some very interesting properties and only a few drawbacks:

- *No positive saturation:* the ReLU is zero for non-positive inputs, but does not saturate otherwise. This ensures a flow of gradient whenever the input is positive, that was found to significantly speed up the convergence of training.
- *Cheap to compute:* as opposed to many other activation functions that require expensive operations, such as for instance exponentials, ReLU's implementation simply amounts to thresholding at zero. Another important characteristic is that the gradient is trivial to compute:

$$\nabla(relu(\mathbf{z}^{(l)})) = \begin{cases} \mathbf{a}^{(l-1)}, & \text{if } \mathbf{z}^{(l)} > 0, \\ 0, & \text{if } \mathbf{z}^{(l)} < 0, \\ \text{undefined}, & \text{if } \mathbf{z}^{(l)} = 0. \end{cases} \quad (2.9)$$

- *Induce sparsity:* ReLU units induce sparsity, indeed whenever the input preactivation is negative their activation is zero. Sparsity is usually a desired property: as opposed to dense encoding, sparsity will produce representations where only a few entries change upon small variations of the input, i.e., it will produce a representation that is more consistent and robust to perturbations. Furthermore, sparsity allows

for a more compact encoding, which is desirable in many contexts such as, e.g., data compression and efficient data transfer. Finally, it is also usually easier to linearly separate sparse representations (Glorot *et al.*, 2011).

- *ReLU units can die:* when a large gradient flows through a ReLU unit it can change its weights in such a way that will prevent it from ever being active again. In this case every input will put the ReLU unit on the flat zero side. This will prevent any gradient flow and the unit will never leave this state becoming *de facto* "dead". This can be alleviated by using a lower learning rate or choosing some modification of ReLU less sensitive to this problem.

Leaky Rectified Linear Unit (Leaky ReLU)

Leaky ReLUs are one of the most adopted alternatives to ReLUs. They have been proposed as a way to alleviate the dying units problem of ReLUs, by preventing the unit from saturating thus allowing a small gradient to always flow through the unit, potentially recovering extreme values of the weights. Leaky ReLUs are defined as

$$\text{leaky_relu}(\mathbf{z}) = \max(\beta * \mathbf{z}, \mathbf{z}), \quad (2.10)$$

where β is a small constant.

Softmax

One peculiar nonlinearity that deserves a particular mention is the softmax. This function differs from the previously described activations in that it does not only depend on the value of the preactivation in one dimension (i.e., the value of one unit), but rather on the preactivation in all the dimensions altogether. The softmax is a *squashing function* that maps its input to a categorical distribution. It is defined as

$$\text{softmax}(z_i) = \frac{\exp(z_i)}{\sum_{k=0}^K \exp(z_k)}, \quad (2.11)$$

where K is the number of classes, i.e., of dimensions (or neurons).

Note that it is possible to add a temperature parameter T to the softmax that allows it to control its steepness (see Figure 2.5), i.e., to control the randomness of predictions. When T is high the distribution over the classes will be more uniform - with the extreme case of $T = \inf$, where all the classes have equal probability. When T is low, the probability curve is more peacky on the class with higher probability and has a light tail on the other classes.

$$\text{softmax}(z_i) = \frac{\exp(z_i/T)}{\sum_{k=0}^K \exp(z_k/T)}. \quad (2.12)$$

2.1.4 Backpropagation

The learning rule originally introduced with Perceptrons did not allow one to train models with multiple layers (i.e., with *hidden* layers), such as the one depicted in Figure 2.3.

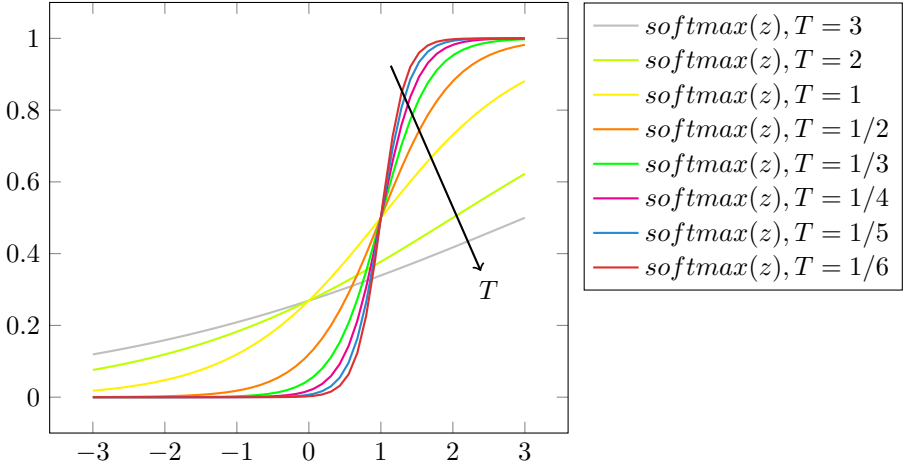


Figure 2.5: The behaviour of softmax as temperature T grows. The plots have been obtained considering a bidimensional input setting where the preactivation associated to the second class z_1 is always 1. As T decreases, the function becomes steeper.

This was not possible since to compute the variation of the weights of a layer with Equation 2.1 it is necessary to know the correct value of its output, which is given only for the last layer.

To address this obstacle it suffices to notice that the computation performed by each activation function is a nonlinear, but differentiable function of the inputs. This allows for the computation of the partial derivatives of the error (e.g., the expected value of the quadratic loss) with respect to the weights of the network. In other words, it is possible to use calculus to determine the amount by which each neuron of the last layer contributed to causing the error, and then further split the responsibility of each of them among the ones of the preceding layer. In this way, the error can be *propagated backwards* through the layers of the network, assigning to each weight its amount of blame. This information can be used by an *optimization algorithm* to iteratively change the weights to minimize the error.

The backpropagation algorithm (see, e.g., Rumelhart *et al.*, 1986b) has some resemblance with the learning rule of the Perceptron (Equation 2.1). The main idea in that case was to modify each weight of the network by a factor proportional to the error ($E = \hat{y} - y$, in the Perceptron) and to the input. Even if in MLPs it is usually common to consider different kinds of cost functions, the same concept applies: the learning procedure tries to modify the weights in order to minimize some error

$$\mathbf{W}|_t = \mathbf{W}|_{t-1} - \eta \left. \frac{\partial E}{\partial \mathbf{W}} \right|_{t-1}, \quad (2.13)$$

where η is a scaling factor typically referred to as *learning rate* that determines the size of the gradient descent steps.

It is easier to understand backpropagation with a practical example. Consider once again Figure 2.3: the network processes a bidimensional input \mathbf{x} and, after three layers

Chapter 2. Background

of affine transformations followed by nonlinearities, returns a scalar value \hat{y} . To keep the narrative as general as possible a 1×1 vector $\hat{\mathbf{y}}$ will be used to denote the output to encompass the case of multiple output units. The correct output \mathbf{y} is given and is used to compute the error, or *cost*, with some *differentiable* metric. For this example consider the mean squared error (MSE)

$$E_{mse} = \frac{1}{M} \sum_{\mathcal{D}} \frac{1}{2} \|\mathbf{y} - \hat{\mathbf{y}}\|_2, \quad (2.14)$$

the summation is done over a dataset \mathcal{D} of M samples, each composed by an input \mathbf{x} and its associated desired output \mathbf{y} . $\hat{\mathbf{y}}$ is used as a compact notation for $\hat{\mathbf{y}}(\mathbf{x})$ and represents the output of the network for one input sample \mathbf{x} .

It is possible to compute the fraction of the error that can be attributed to each weight of the network by taking the derivative of the error with respect to it

$$\begin{aligned} \frac{\partial E_{mse}}{\partial w_{ij}^{(l)}} &= \frac{\partial}{\partial w_{ij}^{(l)}} \left(\frac{1}{m} \sum_{\mathcal{D}} \left[\frac{1}{2} \|\mathbf{y} - \hat{\mathbf{y}}\|_2 \right] \right), \\ &= \frac{1}{m} \sum_{\mathcal{D}} \left[\frac{1}{2} \frac{\partial}{\partial w_{ij}^{(l)}} \left[(\mathbf{y} - \hat{\mathbf{y}})^T (\mathbf{y} - \hat{\mathbf{y}}) \right] \right], \\ &= \frac{1}{m} \sum_{\mathcal{D}} \left[(\mathbf{y} - \hat{\mathbf{y}})^T \frac{\partial(-\hat{\mathbf{y}})}{\partial w_{ij}^{(l)}} \right]. \end{aligned} \quad (2.15)$$

Backpropagation allows one to compute the partial derivative $-\frac{\partial \hat{\mathbf{y}}}{\partial w_{ij}^{(l)}}$ exploiting the chain rule of derivation. Consider, e.g., one weight of the second layer $w_{ij}^{(2)}$

$$\begin{aligned} -\frac{\partial \hat{\mathbf{y}}}{\partial w_{ij}^{(2)}} &= -\frac{\partial \hat{\mathbf{y}}}{\partial \mathbf{z}^{(4)}} \cdot \frac{\partial \mathbf{z}^{(4)}}{\partial w_{ij}^{(2)}}, \\ &= -\frac{\partial \hat{\mathbf{y}}}{\partial \mathbf{z}^{(4)}} \cdot \frac{\partial \mathbf{z}^{(4)}}{\partial \mathbf{a}^{(3)}} \cdot \frac{\partial \mathbf{a}^{(3)}}{\partial w_{ij}^{(2)}}, \\ &= -\frac{\partial \hat{\mathbf{y}}}{\partial \mathbf{z}^{(4)}} \cdot \frac{\partial \mathbf{z}^{(4)}}{\partial \mathbf{a}^{(3)}} \cdot \frac{\partial \mathbf{a}^{(3)}}{\partial \mathbf{z}^{(3)}} \cdot \frac{\partial \mathbf{z}^{(3)}}{\partial w_{ij}^{(2)}}, \\ &= -\frac{\partial \hat{\mathbf{y}}}{\partial \mathbf{z}^{(4)}} \cdot \frac{\partial \mathbf{z}^{(4)}}{\partial \mathbf{a}^{(3)}} \cdot \frac{\partial \mathbf{a}^{(3)}}{\partial \mathbf{z}^{(3)}} \cdot \frac{\partial \mathbf{z}^{(3)}}{\partial \mathbf{a}^{(2)}} \cdot \frac{\partial \mathbf{a}^{(2)}}{\partial w_{ij}^{(2)}}, \\ &= -\frac{\partial \hat{\mathbf{y}}}{\partial \mathbf{z}^{(4)}} \cdot \frac{\partial \mathbf{z}^{(4)}}{\partial \mathbf{a}^{(3)}} \cdot \frac{\partial \mathbf{a}^{(3)}}{\partial \mathbf{z}^{(3)}} \cdot \frac{\partial \mathbf{z}^{(3)}}{\partial \mathbf{a}^{(2)}} \cdot \frac{\partial \mathbf{a}^{(2)}}{\partial \mathbf{z}^{(2)}} \cdot \frac{\partial \mathbf{z}^{(2)}}{\partial w_{ij}^{(2)}}. \end{aligned} \quad (2.16)$$

Replacing $\hat{\mathbf{y}}$ with the corresponding activation (i.e., $\mathbf{a}^{(4)}$ in this example), from Equation 2.2 and Equation 2.3 follows

$$-\frac{\partial \hat{\mathbf{y}}}{\partial w_{ij}^{(2)}} = -\frac{\partial \mathbf{a}^{(4)}}{\partial \mathbf{z}^{(4)}} \cdot \mathbf{W}^{(4)} \cdot \frac{\partial \mathbf{a}^{(3)}}{\partial \mathbf{z}^{(3)}} \cdot \mathbf{W}^{(3)} \cdot \frac{\partial \mathbf{a}^{(2)}}{\partial \mathbf{z}^{(2)}} \cdot [a_j^{(1)}]_i, \quad (2.17)$$

with $[a_j^{(1)}]_i$ a vector of the same size as $\mathbf{z}^{(2)}$ whose i -th element is equal to $a_j^{(1)}$ and all the other elements are 0. Each derivative $\frac{\partial \mathbf{a}^{(l)}}{\partial \mathbf{z}^{(l)}}$ corresponds to an $n \times n$ matrix

$$\frac{\partial \mathbf{a}^{(l)}}{\partial \mathbf{z}^{(l)}} = \begin{bmatrix} \frac{\partial \sigma_0(\mathbf{z}^{(l)})}{\partial z_0^{(l)}} & \dots & \frac{\partial \sigma_0(\mathbf{z}^{(l)})}{\partial z_n^{(l)}} \\ \vdots & \ddots & \vdots \\ \frac{\partial \sigma_n(\mathbf{z}^{(l)})}{\partial z_0^{(l)}} & \dots & \frac{\partial \sigma_n(\mathbf{z}^{(l)})}{\partial z_n^{(l)}} \end{bmatrix}, \quad (2.18)$$

with n the cardinality of $\mathbf{z}^{(l)}$ and $\mathbf{a}^{(l)}$. Note that the derivative of the nonlinear function of choice can be computed analytically as done in Equation 2.6 and Equation 2.9 and applied directly in the formula. Interestingly, when σ is a function applied elementwise (e.g. in the case of logistic, tanh and ReLU activations), $\sigma_i(\mathbf{z}^{(l)}) = \sigma(z_i^{(l)})$, i.e. $\sigma_i(\mathbf{z}^{(l)})$ only depends on the i -th element of z . When this is the case Equation 2.18 is a diagonal matrix

$$\frac{\partial \mathbf{a}^{(l)}}{\partial \mathbf{z}^{(l)}} = \begin{bmatrix} \sigma'(z_0^{(l)}) & & 0 \\ & \ddots & \\ 0 & & \sigma'(z_n^{(l)}) \end{bmatrix}, \quad (2.19)$$

which can be exploited to speed up computation.

2.2 Convolutional networks

Deep CNNs have been at the heart of spectacular advances in deep learning. Although CNNs have been used as early as the nineties to solve character recognition tasks (Le Cun *et al.*, 1997), their current popularity is due to much more recent work, when a deep CNN was used to beat state-of-the-art in the ImageNet image classification challenge (Krizhevsky *et al.*, 2012b).

Section 2.1.2 introduced MLPs, a powerful and very common ANN architecture that computes at each layer an affine transformation of its inputs followed by an activation function. One property of MLPs is that they are dense, in the sense that they often connect all the units of one layer to all the units of the next layer (often referred to as being *fully connected*). When the input has a structure, a dense connectivity pattern might be wasteful and it is usually preferable to be able to exploit the data structure. The reason for this is twofold: first, adapting the connectivity pattern to the structure of the data reduces the number of parameters and of operations performed by the network and, consequently, the memory usage and the computation time; second, constraining the connectivity pattern can have the effect of forcing the network to focus on what is important, yielding faster training and better performance.

Convolutional neural networks (CNNs) are an example of models that exploit the structure of the data. The intuition behind CNNs is that many kinds of data – such as images or audio clips – have a *local* topological structure that does not depend on the specific location in the global reference system. In the case of images, for example, this means that a hand can appear in the center of the image as well as in one of the corners, and is not less of a hand in either cases. Similarly, the sound of the word *hand* should be detected the same way when pronounced with a high or low pitch.

CNNs exploit this understanding of the data by applying the same pattern detector at many locations in the image. This is formally done through a *convolution* (hence the name CNN), a signal processing operation that superimposes a pattern detector – usually called *filter*, *kernel* or *mask* – on different locations of the image and emits an activation in each position. In the previous example this would mean applying a "hand detector" on every location of the image to produce a matrix of activations, typically referred to as *feature map*. In any real-world application though, it would be common to apply multiple kernels at once with the same convolution, hence obtaining a tensor of feature maps.

The convolution operation can be seen as the repetition of two operations: the superimposition of one or more kernels in one position, followed by a shift – or *stride* – of the kernels to allow their subsequent applications in the next position. This system works successfully in most cases, but it would most likely fail to e.g., detect hands that are not completely contained in the image. The typical solution adopted to overcome this limitation is to *pad* the image by adding a frame (usually of zeros) around it on every side. This ensures that on the borders of the image the convolution performs both a complete superimposition of the kernel on every position in the image, as well as partial ones (that is, a superimposition that is partially on the image and partially on the padding). In the padded half hand scenario, this partial superimposition over the image would cause an activation that is not as strong as in the case of a full overlap, but not zero either.

The elements described so far fully define a convolution. The shape of the feature maps produced by a convolutional layer is affected by the shape of its input as well as the choice of kernel shape, zero padding and strides, and the relationship between these properties is not always trivial to infer. This contrasts with fully-connected layers, whose output size is independent of the input size.

Additionally, CNNs also usually feature *pooling* layers, adding yet another level of complexity with respect to fully-connected networks. Finally, so-called transposed convolutional layers (also known as fractionally strided convolutional layers) have been employed in more and more work as of late (Zeiler *et al.*, 2011b; Zeiler and Fergus, 2014a; Long *et al.*, 2015a; Radford *et al.*, 2015; Visin *et al.*, 2016; Im *et al.*, 2016), and their relationship with convolutional layers has been explained with various degrees of clarity.

The convolution operation will be formally introduced in Section 2.2.1 followed by a description of pooling in Section 2.2.2. The rest of this section will focus on the arithmetic to compute the output shape of a convolution given its parameters. In particular Section 2.2.7 targets transposed convolutions, a smart application of convolutions to upsampling. For an in-depth treatment of the subject, see Chapter 9 of the Deep Learning textbook (Goodfellow *et al.*, 2016).

2.2.1 Discrete convolutions

The bread and butter of neural networks is *affine transformations*: a vector is received as input and is multiplied with a matrix to produce an output (to which a bias vector is usually added before passing the result through a nonlinearity). This is applicable to any type of input, be it an image, a sound clip or an unordered collection of features; whatever their dimensionality, their representation can always be flattened into a vector before the transformation.

Images, sound clips and many other similar kinds of data have an intrinsic structure. More formally, they share these important properties:

- They are stored as multi-dimensional arrays.
- They feature one or more axes for which ordering matters (e.g., width and height axes for an image, time axis for a sound clip, etc, ..).
- One axis, called the channel axis, is used to access different views of the data (e.g., the red, green and blue channels of a color image, or the left and right channels of a stereo audio track).

These properties are not exploited when an affine transformation is applied; in fact, all the axes are treated in the same way and the topological information is not taken into account. Still, taking advantage of the implicit structure of the data may prove very handy in solving some tasks, like computer vision and speech recognition, and in these cases it would be best to preserve it. This is where discrete convolutions come into play.

A discrete convolution is a linear transformation that preserves this notion of ordering. It is sparse (only a few input units contribute to a given output unit) and reuses parameters (the same weights are applied to multiple locations in the input). Figure 2.6 provides an example of a discrete convolution. The light blue grid is called the *input feature map*. To keep the drawing simple, a single input feature map is represented, but it is not uncommon to have multiple feature maps stacked one onto another.¹

A *kernel* (shaded area) with the following weights:

0	1	2
2	2	0
0	1	2

slides across the input feature map. At each location, the product between each element of the kernel and the input element it overlaps is computed and the results are summed up to obtain the output in the current location. The procedure can be repeated using different kernels to form as many output feature maps as desired (Figure 2.8). The final outputs of this procedure are called *output feature maps*.² If there are multiple input feature maps, the kernel will have to be 3-dimensional – or, equivalently, each one of the feature maps will be convolved with a distinct kernel – and the resulting feature maps will be summed up elementwise to produce the output feature map. The convolution depicted in Figure 2.6 is an instance of a 2-D convolution, but it can be generalized to N-D convolutions. For instance, in a 3-D convolution, the kernel would be a *cuboid* and would slide across the height, width and depth of the input feature map.

The collection of kernels defining a discrete convolution has a shape corresponding to some assignment of (n, m, k_1, \dots, k_N) , where

¹An example of this is what was referred to earlier as *channels* for images and sound clips.

²While there is a distinction between convolution and cross-correlation from a signal processing perspective, the two become interchangeable when the kernel is learned. For the sake of simplicity and to stay consistent with most of the machine learning literature, the term *convolution* will be used in this guide.

Chapter 2. Background

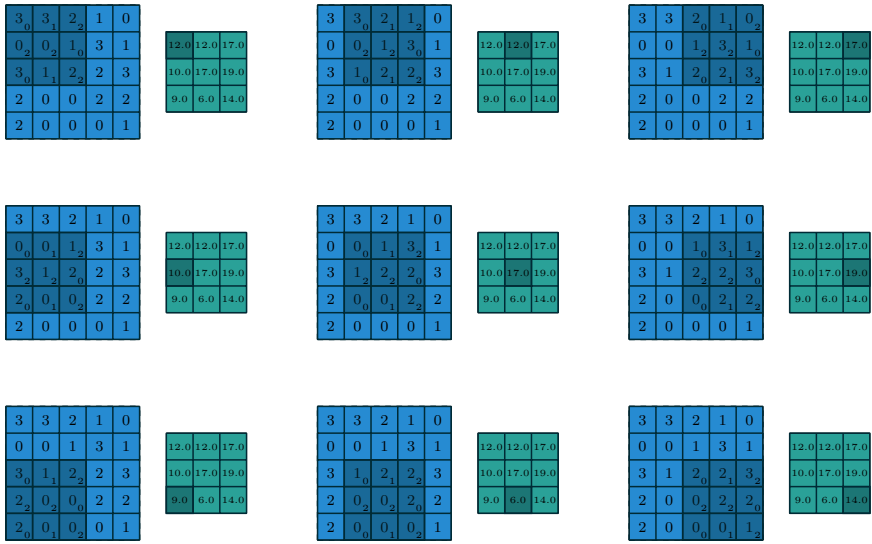


Figure 2.6: Computing the output values of a discrete convolution.

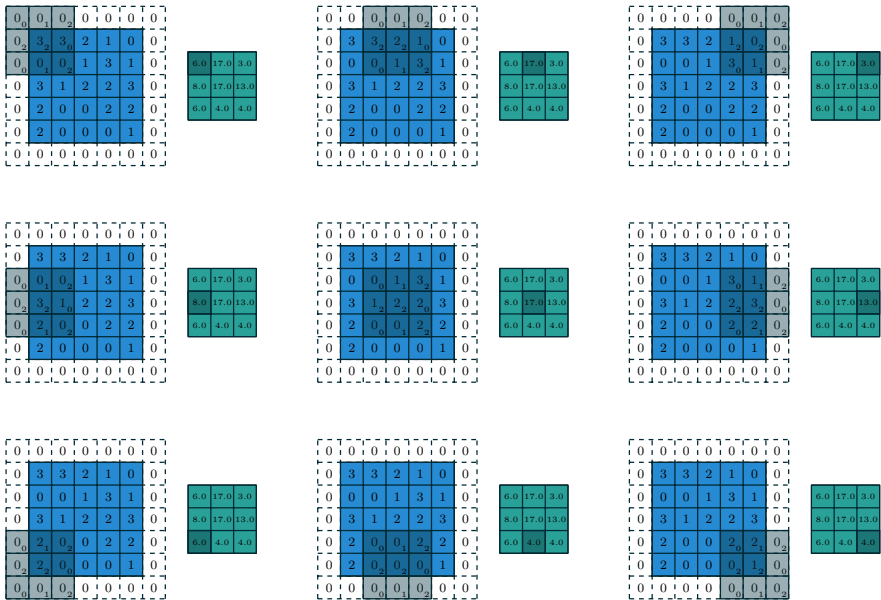


Figure 2.7: Computing the output values of a discrete convolution for $N = 2$, $i_1 = i_2 = 5$, $k_1 = k_2 = 3$, $s_1 = s_2 = 2$, and $p_1 = p_2 = 1$.

$$\begin{aligned} n &\equiv \text{number of output feature maps}, \\ m &\equiv \text{number of input feature maps}, \\ k_j &\equiv \text{kernel size along axis } j. \end{aligned}$$

The following properties affect the output size o_j of a convolutional layer along axis j :

- i_j : input size along axis j ,
- k_j : kernel size along axis j ,
- s_j : stride (distance between two consecutive positions of the kernel) along axis j ,
- p_j : zero padding (number of zeros concatenated at the beginning and at the end of an axis) along axis j .

For instance, Figure 2.7 shows a 3×3 kernel applied to a 5×5 input padded with a 1×1 border of zeros using 2×2 strides.

Note that strides constitute a form of *subsampling*. As an alternative to being interpreted as a measure of how much the kernel is translated, strides can also be viewed as how much of the output is retained. For instance, moving the kernel by hops of two is equivalent to moving the kernel by hops of one but retaining only odd output elements (Figure 2.9).

2.2.2 Pooling

In addition to discrete convolutions themselves, *pooling* operations constitute another important building block in CNNs. Pooling operations reduce the size of feature maps by using some function to summarize subregions, such as taking the average or the maximum value.

Pooling works by sliding a window across the input and feeding the content of the window to a *pooling function*. In some sense, pooling works very much like a discrete convolution, but replaces the linear combination described by the kernel with some other function. Figure 2.10 provides an example for average pooling, and Figure 2.11 does the same for max pooling.

The following properties affect the output size o_j of a pooling layer along axis j :

- i_j : input size along axis j ,
- k_j : pooling window size along axis j ,
- s_j : stride (distance between two consecutive positions of the pooling window) along axis j .

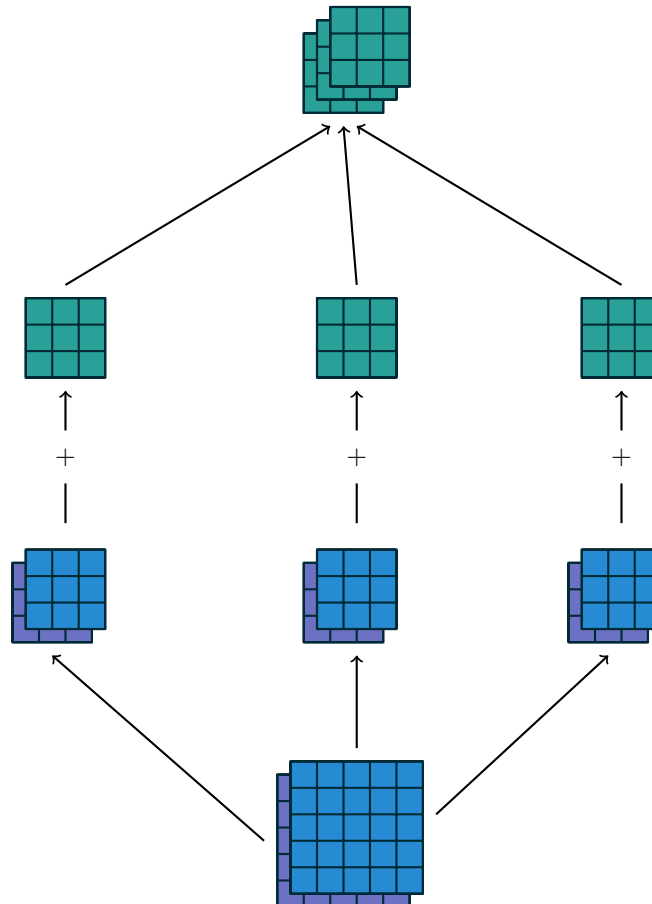


Figure 2.8: A convolution mapping from two input feature maps to three output feature maps using a $3 \times 2 \times 3 \times 3$ collection of kernels w . In the left pathway, input feature map 1 is convolved with kernel $w_{1,1}$ and input feature map 2 is convolved with kernel $w_{1,2}$, and the results are summed together elementwise to form the first output feature map. The same is repeated for the middle and right pathways to form the second and third output feature maps, and all three output feature maps are grouped together to form the output.

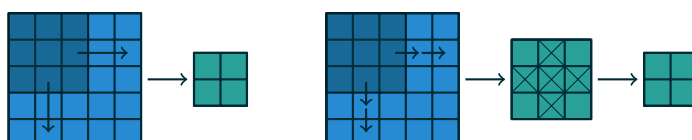


Figure 2.9: An alternative way of viewing strides. Instead of translating the 3×3 kernel by increments of $s = 2$ (left), the kernel is translated by increments of 1 and only one in $s = 2$ output elements is retained (right).

2.2. Convolutional networks

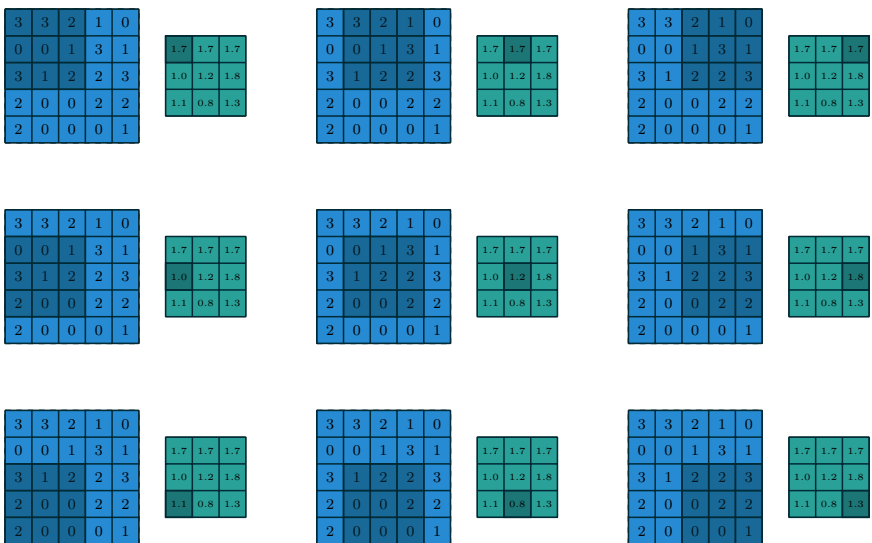


Figure 2.10: Computing the output values of a 3×3 average pooling operation on a 5×5 input using 1×1 strides.



Figure 2.11: Computing the output values of a 3×3 max pooling operation on a 5×5 input using 1×1 strides.

2.2.3 Convolution arithmetic

The analysis of the relationship between convolutional layer properties is eased by the fact that they do not interact across axes, i.e., the choice of kernel size, stride and zero padding along axis j only affects the output size of axis j . Because of that, this chapter focuses on the following simplified setting to facilitate the analysis and the visualization, but keep in mind that the results outlined here also generalize to the N-D and non-square cases:

- 2-D discrete convolutions ($N = 2$),
- square inputs ($i_1 = i_2 = i$),
- square kernel size ($k_1 = k_2 = k$),
- same strides along both axes ($s_1 = s_2 = s$),
- same zero padding along both axes ($p_1 = p_2 = p$).

No zero padding, unit strides

The simplest case to analyze is when the kernel just slides across every position of the input (i.e., $s = 1$ and $p = 0$). Figure 2.12 provides an example for $i = 4$ and $k = 3$.

One way of defining the output size in this case is by the number of possible placements of the kernel on the input. Let's consider the width axis: the kernel starts on the leftmost part of the input feature map and slides by steps of one until it touches the right side of the input. The size of the output will be equal to the number of steps made, plus one, accounting for the initial position of the kernel (Figure 2.19a). The same logic applies for the height axis. More formally, the following relationship between the parameters of the convolution, the input shape i and the output shape o can be inferred:

Relationship 1. *For any i and k , and for $s = 1$ and $p = 0$,*

$$o = (i - k) + 1.$$

Zero padding, unit strides

To factor in zero padding (i.e., only restricting to $s = 1$), let's consider its effect on the effective input size: padding with p zeros changes the effective input size from i to $i + 2p$. In the general case, Relationship 1 can then be used to infer the following relationship:

Relationship 2. *For any i , k and p , and for $s = 1$,*

$$o = (i - k) + 2p + 1,$$

Figure 2.13 provides an example for $i = 5$, $k = 4$ and $p = 2$.

In practice, two specific instances of zero padding are used quite extensively because of their respective properties. Let's discuss them in more detail.

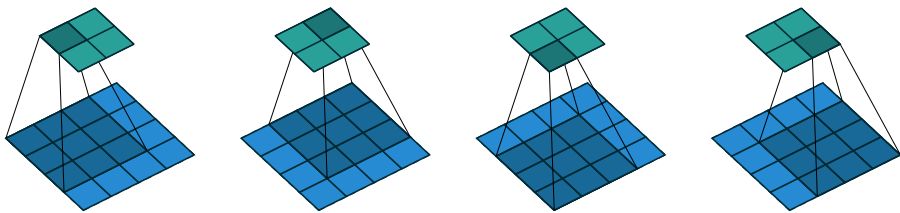


Figure 2.12: (No padding, unit strides) Convolving a 3×3 kernel over a 4×4 input using unit strides (i.e., $i = 4$, $k = 3$, $s = 1$ and $p = 0$).

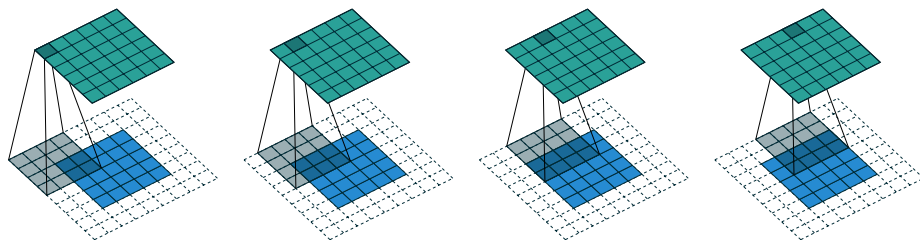


Figure 2.13: (Arbitrary padding, unit strides) Convolving a 4×4 kernel over a 5×5 input padded with a 2×2 border of zeros using unit strides (i.e., $i = 5$, $k = 4$, $s = 1$ and $p = 2$).

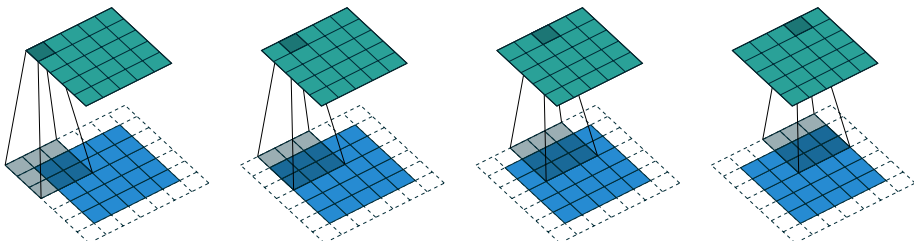


Figure 2.14: (Half padding, unit strides) Convolving a 3×3 kernel over a 5×5 input using half padding and unit strides (i.e., $i = 5$, $k = 3$, $s = 1$ and $p = 1$).

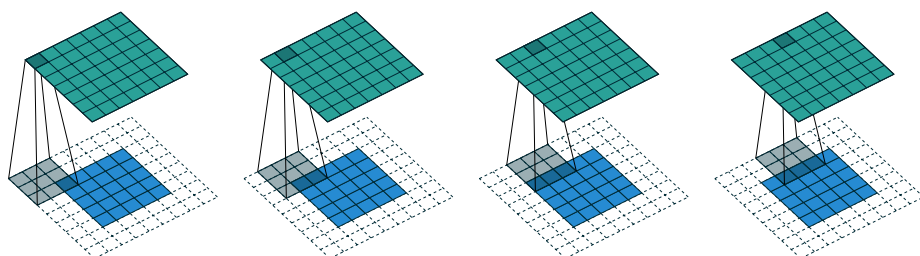


Figure 2.15: (Full padding, unit strides) Convolving a 3×3 kernel over a 5×5 input using full padding and unit strides (i.e., $i = 5$, $k = 3$, $s = 1$ and $p = 2$).

Half (same) padding

Having the output size be the same as the input size (i.e., $o = i$) can be a desirable property:

Relationship 3. For any i and for k odd ($k = 2n + 1$, $n \in \mathbb{N}$), $s = 1$ and $p = \lfloor k/2 \rfloor = n$,

$$\begin{aligned} o &= i + 2\lfloor k/2 \rfloor - (k - 1), \\ &= i + 2n - 2n, \\ &= i. \end{aligned}$$

This is sometimes referred to as *half* (or *same*) padding. Figure 2.14 provides an example for $i = 5$, $k = 3$ and (therefore) $p = 1$.

Full padding

While convolving a kernel generally *decreases* the output size with respect to the input size, sometimes the opposite is required. This can be achieved with proper zero padding:

Relationship 4. For any i and k , and for $p = k - 1$ and $s = 1$,

$$\begin{aligned} o &= i + 2(k - 1) - (k - 1), \\ &= i + (k - 1). \end{aligned}$$

This is sometimes referred to as *full* padding, because in this setting every possible partial or complete superimposition of the kernel on the input feature map is taken into account. Figure 2.15 provides an example for $i = 5$, $k = 3$ and (therefore) $p = 2$.

2.2.4 No zero padding, non-unit strides

All relationships derived so far only apply for unit-strided convolutions. Incorporating non unitary strides requires another inference leap. To facilitate the analysis, let's momentarily ignore zero padding (i.e., $s > 1$ and $p = 0$). Figure 2.16 provides an example for $i = 5$, $k = 3$ and $s = 2$.

Once again, the output size can be defined in terms of the number of possible placements of the kernel on the input. Let's consider the width axis: the kernel starts as usual on the leftmost part of the input, but this time it slides by steps of size s until it touches the right side of the input. The size of the output is again equal to the number of steps made, plus one, accounting for the initial position of the kernel (Figure 2.19b). The same logic applies for the height axis. From this, the following relationship can be inferred:

Relationship 5. For any i , k and s , and for $p = 0$,

$$o = \left\lfloor \frac{i - k}{s} \right\rfloor + 1.$$

The floor function accounts for the fact that sometimes the last possible step does *not* coincide with the kernel reaching the end of the input, i.e., some input units are left out (see Figure 2.18 for an example of such a case).

2.2.5 Zero padding, non-unit strides

The most general case (convolving over a zero padded input using non-unit strides) can be derived by applying Relationship 5 on an effective input of size $i + 2p$, in analogy to what was done for Relationship 2:

Relationship 6. *For any i, k, p and s ,*

$$o = \left\lfloor \frac{i + 2p - k}{s} \right\rfloor + 1.$$

As before, the floor function means that in some cases a convolution will produce the same output size for multiple input sizes. More specifically, if $i + 2p - k$ is a multiple of s , then any input size $j = i + a$, $a \in \{0, \dots, s - 1\}$ will produce the same output size. Note that this ambiguity applies only for $s > 1$.

Figure 2.17 shows an example with $i = 5, k = 3, s = 2$ and $p = 1$, while Figure 2.18 provides an example for $i = 6, k = 3, s = 2$ and $p = 1$. Interestingly, despite having different input sizes these convolutions share the same output size. While this does not affect the analysis for *convolutions*, this will complicate the analysis in the case of *transposed convolutions*.

2.2.6 Pooling arithmetic

In a neural network, pooling layers provide invariance to small translations of the input. The most common kind of pooling is *max pooling*, which consists in splitting the input in (usually non-overlapping) patches and outputting the maximum value of each patch. Other kinds of pooling exist, e.g., mean or average pooling, which all share the same idea of aggregating the input locally by applying a nonlinearity to the content of some patches (Boureau *et al.*, 2010a,b, 2011; Saxe *et al.*, 2011).

Notice that the treatment of convolution arithmetic only relies on the assumption that some function is repeatedly applied onto subsets of the input. This means that the relationships derived in the previous chapter can be reused in the case of pooling arithmetic. Since pooling does not involve zero padding, the relationship describing the general case is as follows:

Relationship 7. *For any i, k and s ,*

$$o = \left\lfloor \frac{i - k}{s} \right\rfloor + 1.$$

This relationship holds for any type of pooling.

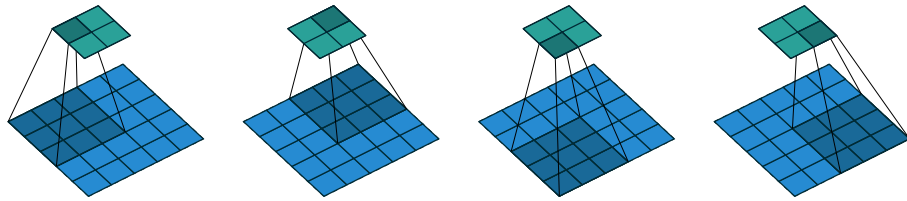


Figure 2.16: (No zero padding, arbitrary strides) Convolving a 3×3 kernel over a 5×5 input using 2×2 strides (i.e., $i = 5$, $k = 3$, $s = 2$ and $p = 0$).

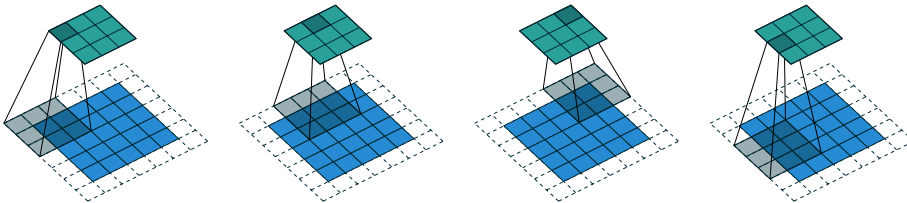


Figure 2.17: (Arbitrary padding and strides) Convolving a 3×3 kernel over a 5×5 input padded with a 1×1 border of zeros using 2×2 strides (i.e., $i = 5$, $k = 3$, $s = 2$ and $p = 1$).

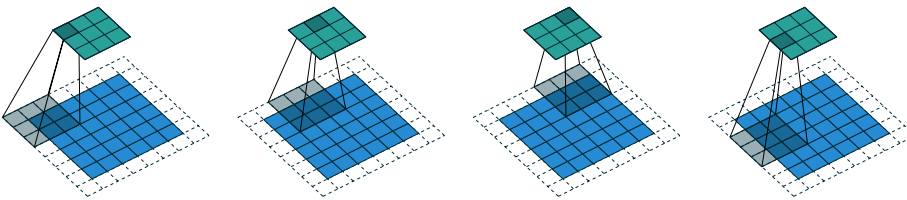
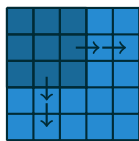
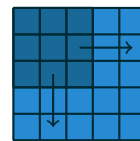


Figure 2.18: (Arbitrary padding and strides) Convolving a 3×3 kernel over a 6×6 input padded with a 1×1 border of zeros using 2×2 strides (i.e., $i = 6$, $k = 3$, $s = 2$ and $p = 1$). In this case, the bottom row and right column of the zero padded input are not covered by the kernel.



- (a) The kernel has to slide two steps to the right to touch the right side of the input (and equivalently downwards). Adding one to account for the initial kernel position, the output size is 3×3 .



- (b) The kernel has to slide one step of size two to the right to touch the right side of the input (and equivalently downwards). Adding one to account for the initial kernel position, the output size is 2×2 .

Figure 2.19: Counting kernel positions.

2.2.7 Transposed convolution arithmetic

The need for transposed convolutions generally arises from the desire to use a transformation going in the opposite direction of a normal convolution, i.e., from something that has the shape of the output of some convolution to something that has the shape of its input while maintaining a connectivity pattern that is compatible with said convolution. For instance, one might use such a transformation as the decoding layer of a convolutional autoencoder or to project feature maps to a higher-dimensional space.

Once again, the convolutional case is considerably more complex than the fully-connected case, which only requires to use a weight matrix whose shape has been transposed. However, since every convolution boils down to an efficient implementation of a matrix operation, the insights gained from the fully-connected case are useful in solving the convolutional case.

Like for convolution arithmetic, the dissertation about transposed convolution arithmetic is simplified by the fact that transposed convolution properties do not interact across axes. The usual simplified setting will be taken in account, but as before the results outlined generalize to the N-D and non-square cases.

2.2.8 Convolution as a matrix operation

Take for example the convolution represented in Figure 2.12. If the input and output were to be unrolled into vectors from left to right, top to bottom, the convolution could be represented as a sparse matrix \mathbf{C} where the non-zero elements are the elements $w_{i,j}$ of the kernel (with i and j being the row and column of the 3×3 kernel $K = (w_{0,0}..w_{2,2})$ respectively):

$$\begin{pmatrix} w_{0,0} & w_{0,1} & w_{0,2} & 0 & w_{1,0} & w_{1,1} & w_{1,2} & 0 & w_{2,0} & w_{2,1} & w_{2,2} & 0 & 0 & 0 & 0 & 0 \\ 0 & w_{0,0} & w_{0,1} & w_{0,2} & 0 & w_{1,0} & w_{1,1} & w_{1,2} & 0 & w_{2,0} & w_{2,1} & w_{2,2} & 0 & 0 & 0 & 0 & 0 \\ 0 & 0 & 0 & 0 & w_{0,0} & w_{0,1} & w_{0,2} & 0 & w_{1,0} & w_{1,1} & w_{1,2} & 0 & w_{2,0} & w_{2,1} & w_{2,2} & 0 \\ 0 & 0 & 0 & 0 & 0 & w_{0,0} & w_{0,1} & w_{0,2} & 0 & w_{1,0} & w_{1,1} & w_{1,2} & 0 & w_{2,0} & w_{2,1} & w_{2,2} \end{pmatrix}$$

This linear operation takes the input matrix flattened as a 16-dimensional vector and produces a 4-dimensional vector that is later reshaped as the 2×2 output matrix. Using this representation, the backward pass is easily obtained by transposing \mathbf{C} ; in other words, the error is backpropagated by multiplying the loss with \mathbf{C}^T . This operation takes a 4-dimensional vector as input and produces a 16-dimensional vector as output, and its connectivity pattern is compatible with \mathbf{C} by construction.

Notably, the kernel \mathbf{w} defines both the matrices \mathbf{C} and \mathbf{C}^T used for the forward and backward passes.

2.2.9 Transposed convolution

Let's now consider what would be required to go the other way around, i.e., map from a 4-dimensional space to a 16-dimensional space, while keeping the connectivity pattern of the convolution depicted in Figure 2.12. This operation is known as a *transposed convolution*.

Transposed convolutions – also called *fractionally strided convolutions* – work by swapping the forward and backward passes of a convolution. One way to put it is to note

that the kernel defines a convolution, but whether it is a direct convolution or a transposed convolution is determined by how the forward and backward passes are computed.

For instance, although the kernel w defines a convolution whose forward and backward passes are computed by multiplying with C and C^T respectively, it *also* defines a transposed convolution whose forward and backward passes are computed by multiplying with C^T and $(C^T)^T = C$ respectively.³

Finally note that it is always possible to emulate a transposed convolution with a direct convolution. The disadvantage is that it usually involves adding many columns and rows of zeros to the input, resulting in a much less efficient implementation.

Building on what has been introduced so far, this section will derive the properties of each transposed convolution by referring to the direct convolution with which it shares the kernel, and defining the equivalent direct convolution.

2.2.10 No zero padding, unit strides, transposed

The simplest way to think about a transposed convolution is by computing the output shape of the direct convolution for a given input shape first, and then inverting the input and output shapes for the transposed convolution.

Let's consider the convolution of a 3×3 kernel on a 4×4 input with unitary stride and no padding (i.e., $i = 4$, $k = 3$, $s = 1$ and $p = 0$). As depicted in Figure 2.12, this produces a 2×2 output. The transpose of this convolution will then have an output of shape 4×4 when applied on a 2×2 input.

Another way to obtain the result of a transposed convolution is to apply an equivalent – but much less efficient – direct convolution. The example described so far could be tackled by convolving a 3×3 kernel over a 2×2 input padded with a 2×2 border of zeros using unit strides (i.e., $i' = 2$, $k' = k$, $s' = 1$ and $p' = 2$), as shown in Figure 2.20. Notably, the kernel's and stride's sizes remain the same, but the input of the transposed convolution is now zero padded.⁴

One way to understand the logic behind zero padding is to consider the connectivity pattern of the transposed convolution and use it to guide the design of the equivalent convolution. For example, the top left pixel of the input of the direct convolution only contribute to the top left pixel of the output, the top right pixel is only connected to the top right output pixel, and so on. To maintain the same connectivity pattern in the equivalent convolution it is necessary to zero pad the input in such a way that the first (top-left) application of the kernel only touches the top-left pixel, i.e., the padding has to be equal to the size of the kernel minus one.

Proceeding in the same fashion it is possible to determine similar observations for the other elements of the image, giving rise to the following relationship:

³The transposed convolution operation can be thought of as the gradient of *some* convolution with respect to its input, which is usually how transposed convolutions are implemented in practice.

⁴Note that although equivalent to applying the transposed matrix, this visualization adds a lot of zero multiplications in the form of zero padding. This is done here for illustration purposes, but it is inefficient, and software implementations will normally not perform the useless zero multiplications.

Relationship 8. A convolution described by $s = 1$, $p = 0$ and k has an associated transposed convolution described by $k' = k$, $s' = s$ and $p' = k - 1$ and its output size is

$$o' = i' + (k - 1).$$

Interestingly, this corresponds to a fully padded convolution with unit strides.

2.2.11 Zero padding, unit strides, transposed

Knowing that the transpose of a non-padded convolution is equivalent to convolving a zero padded input, it would be reasonable to suppose that the transpose of a zero padded convolution is equivalent to convolving an input padded with *less* zeros. It is indeed the case, as shown in Figure 2.21 for $i = 5$, $k = 4$ and $p = 2$.

Formally, the following relationship applies for zero padded convolutions:

Relationship 9. A convolution described by $s = 1$, k and p has an associated transposed convolution described by $k' = k$, $s' = s$ and $p' = k - p - 1$ and its output size is

$$o' = i' + (k - 1) - 2p.$$

Half (same) padding, transposed

By applying the same inductive reasoning as before, it is reasonable to expect that the equivalent convolution of the transpose of a half padded convolution is itself a half padded convolution, given that the output size of a half padded convolution is the same as its input size. Thus the following relation applies:

Relationship 10. A convolution described by $k = 2n + 1$, $n \in \mathbb{N}$, $s = 1$ and $p = \lfloor k/2 \rfloor = n$ has an associated transposed convolution described by $k' = k$, $s' = s$ and $p' = p$ and its output size is

$$\begin{aligned} o' &= i' + (k - 1) - 2p, \\ &= i' + 2n - 2n, \\ &= i'. \end{aligned}$$

Figure 2.22 provides an example for $i = 5$, $k = 3$ and (therefore) $p = 1$.

Full padding, transposed

Knowing that the equivalent convolution of the transpose of a non-padded convolution involves full padding, it is unsurprising that the equivalent of the transpose of a fully padded convolution is a non-padded convolution:

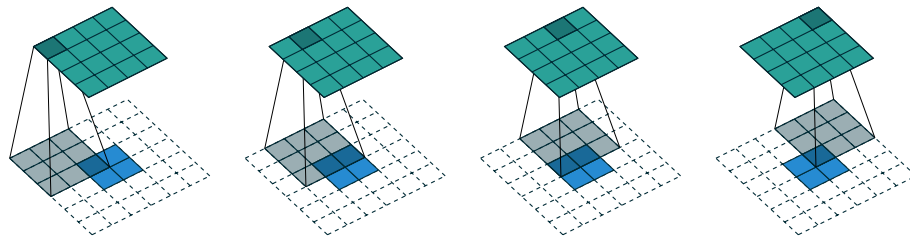


Figure 2.20: The transpose of convolving a 3×3 kernel over a 4×4 input using unit strides (i.e., $i = 4$, $k = 3$, $s = 1$ and $p = 0$). It is equivalent to convolving a 3×3 kernel over a 2×2 input padded with a 2×2 border of zeros using unit strides (i.e., $i' = 2$, $k' = k$, $s' = 1$ and $p' = 2$).

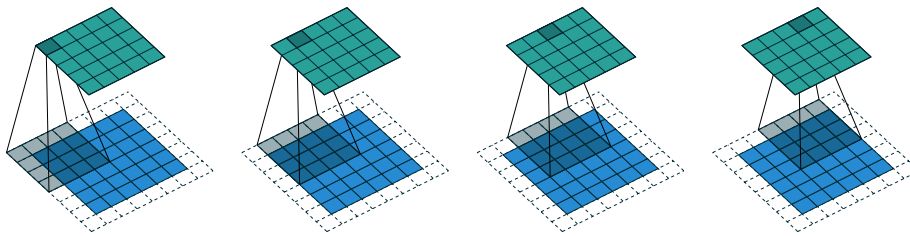


Figure 2.21: The transpose of convolving a 4×4 kernel over a 5×5 input padded with a 2×2 border of zeros using unit strides (i.e., $i = 5$, $k = 4$, $s = 1$ and $p = 2$). It is equivalent to convolving a 4×4 kernel over a 6×6 input padded with a 1×1 border of zeros using unit strides (i.e., $i' = 6$, $k' = k$, $s' = 1$ and $p' = 1$).

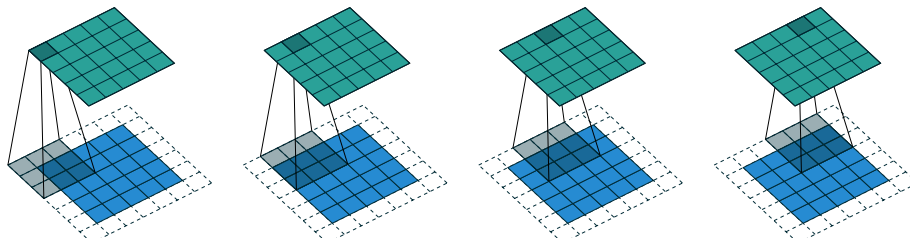


Figure 2.22: The transpose of convolving a 3×3 kernel over a 5×5 input using half padding and unit strides (i.e., $i = 5$, $k = 3$, $s = 1$ and $p = 1$). It is equivalent to convolving a 3×3 kernel over a 5×5 input using half padding and unit strides (i.e., $i' = 5$, $k' = k$, $s' = 1$ and $p' = 1$).

Relationship 11. A convolution described by $s = 1$, k and $p = k - 1$ has an associated transposed convolution described by $k' = k$, $s' = s$ and $p' = 0$ and its output size is

$$\begin{aligned} o' &= i' + (k - 1) - 2p, \\ &= i' - (k - 1). \end{aligned}$$

Figure 2.23 provides an example for $i = 5$, $k = 3$ and (therefore) $p = 2$.

2.2.12 No zero padding, non-unit strides, transposed

Using the same kind of inductive logic as for zero padded convolutions, one might expect that the transpose of a convolution with $s > 1$ involves an equivalent convolution with $s < 1$. As will be explained, this is a valid intuition, which is why transposed convolutions are sometimes called *fractionally strided convolutions*. Figure 2.24 provides an example for $i = 5$, $k = 3$ and $s = 2$ which helps understand what fractional strides involve: zeros are inserted *between* input units, which makes the kernel move around at a slower pace than with unit strides.⁵

For the moment, it will be assumed that the convolution is non-padded ($p = 0$) and that its input size i is such that $i - k$ is a multiple of s . In that case, the following relationship holds:

Relationship 12. A convolution described by $p = 0$, k and s and whose input size is such that $i - k$ is a multiple of s , has an associated transposed convolution described by \tilde{i}' , $k' = k$, $s' = 1$ and $p' = k - 1$, where \tilde{i}' is the size of the stretched input obtained by adding $s - 1$ zeros between each input unit, and its output size is

$$o' = s(\tilde{i}' - 1) + k.$$

2.2.13 Zero padding, non-unit strides, transposed

When the convolution's input size i is such that $i + 2p - k$ is a multiple of s , the analysis can be extended to the zero padded case by combining Relationship 9 and Relationship 12:

Relationship 13. A convolution described by k , s and p and whose input size i is such that $i + 2p - k$ is a multiple of s has an associated transposed convolution described by \tilde{i}' , $k' = k$, $s' = 1$ and $p' = k - p - 1$, where \tilde{i}' is the size of the stretched input obtained by adding $s - 1$ zeros between each input unit, and its output size is

$$o' = s(\tilde{i}' - 1) + k - 2p.$$

Figure 2.25 provides an example for $i = 5$, $k = 3$, $s = 2$ and $p = 1$.

⁵Doing so is inefficient and real-world implementations avoid useless multiplications by zero, but conceptually it is how the transpose of a strided convolution can be thought of.

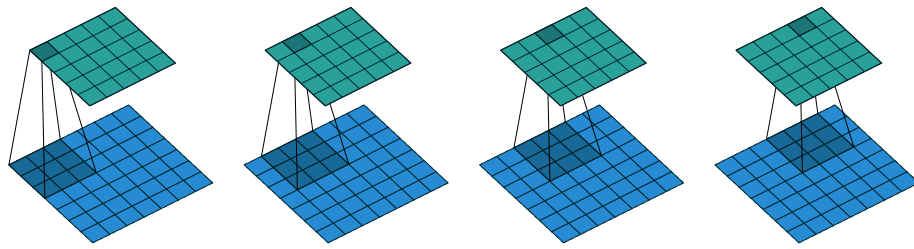


Figure 2.23: The transpose of convolving a 3×3 kernel over a 5×5 input using full padding and unit strides (i.e., $i = 5$, $k = 3$, $s = 1$ and $p = 2$). It is equivalent to convolving a 3×3 kernel over a 7×7 input using unit strides (i.e., $i' = 7$, $k' = k$, $s' = 1$ and $p' = 0$).

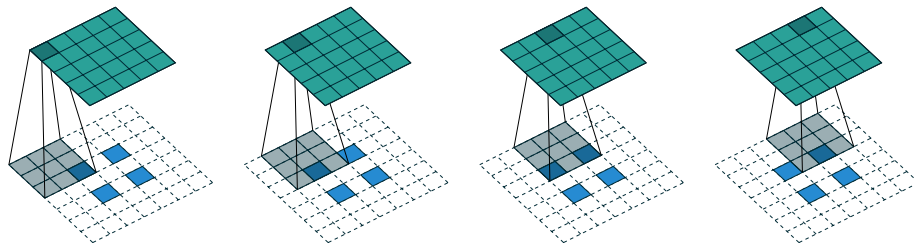


Figure 2.24: The transpose of convolving a 3×3 kernel over a 5×5 input using 2×2 strides (i.e., $i = 5$, $k = 3$, $s = 2$ and $p = 0$). It is equivalent to convolving a 3×3 kernel over a 2×2 input (with 1 zero inserted between inputs) padded with a 2×2 border of zeros using unit strides (i.e., $i' = 2$, $\tilde{i}' = 3$, $k' = k$, $s' = 1$ and $p' = 2$).

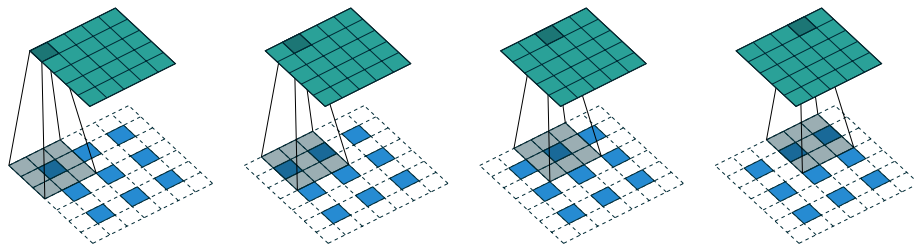


Figure 2.25: The transpose of convolving a 3×3 kernel over a 5×5 input padded with a 1×1 border of zeros using 2×2 strides (i.e., $i = 5$, $k = 3$, $s = 2$ and $p = 1$). It is equivalent to convolving a 3×3 kernel over a 2×2 input (with 1 zero inserted between inputs) padded with a 1×1 border of zeros using unit strides (i.e., $i' = 3$, $\tilde{i}' = 5$, $k' = k$, $s' = 1$ and $p' = 1$).

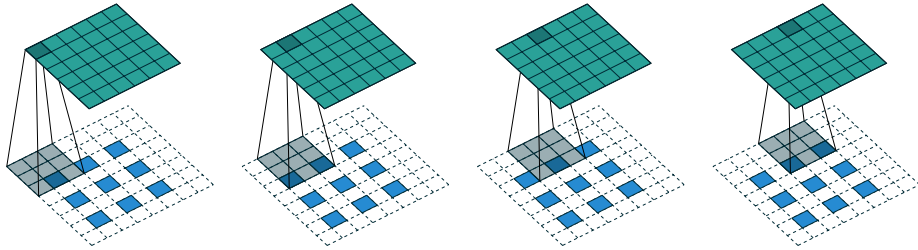


Figure 2.26: The transpose of convolving a 3×3 kernel over a 6×6 input padded with a 1×1 border of zeros using 2×2 strides (i.e., $i = 6$, $k = 3$, $s = 2$ and $p = 1$). It is equivalent to convolving a 3×3 kernel over a 2×2 input (with 1 zero inserted between inputs) padded with a 1×1 border of zeros (with an additional border of size 1 added to the top and right edges) using unit strides (i.e., $i' = 3$, $\tilde{i}' = 5$, $a = 1$, $k' = k$, $s' = 1$ and $p' = 1$).

The constraint on the size of the input i can be relaxed by introducing another parameter $a \in \{0, \dots, s - 1\}$ that allows to distinguish between the s different cases that all lead to the same i' :

Relationship 14. A convolution described by k , s and p has an associated transposed convolution described by a , \tilde{i}' , $k' = k$, $s' = 1$ and $p' = k - p - 1$, where \tilde{i}' is the size of the stretched input obtained by adding $s - 1$ zeros between each input unit, and $a = (i + 2p - k) \bmod s$ represents the number of zeros added to the top and right edges of the input, and its output size is

$$o' = s(i' - 1) + a + k - 2p.$$

Figure 2.26 provides an example for $i = 6$, $k = 3$, $s = 2$ and $p = 1$.

2.3 Recurrent networks

It is well known that the brain is organized in functional areas and sub-areas that process the incoming signal in an incremental fashion. These areas of the brain are typically connected both in a *feedforward*, i.e., towards neurons belonging to deeper (i.e., further away from the sensory input) layers, and in a *feedback* fashion (i.e., to previous layers in the hierarchy). This is believed to help processing temporal data and allow for an iterative refinement of the computation.

Similarly, ANNs are not constrained to process the input data in a feedforward way. Recurrent Neural Networks (RNNs) implement feedback loops (see Figure 2.27 ⁶) that propagate some information from one step to the next. It is customary to refer to these steps as time-steps, as RNNs are often considered in the context of a discretized time evolving domain, but nothing prevents from using RNNs with any kind of sequential data.

⁶This and the following RNN figures, are taken or modified from the awesome introduction to RNNs and LSTMs by Chris Olah (Olah, 2015)

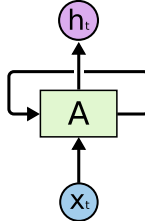


Figure 2.27: A Recurrent Neural Network (RNN).

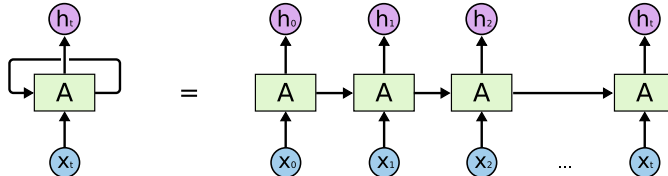


Figure 2.28: A Recurrent Neural Network unrolled for t steps.

Suppose to model some sequential data $x_0, x_1, \dots, x_t, x_{t+1}, \dots$ such as an English sentence. At time t it is possible to model the probability distribution over a dictionary of English words, conditioned on the words seen up that moment – namely x_0, x_1, \dots, x_{t-1} . This can be used, for instance, in a smart keyboard application to suggest the next most probable words to the user or, in an automatic help desk, to generate a meaningful answer to a question.

It might not be immediately obvious what it means in practice to put a loop in an ANN and how to backpropagate through it. To better comprehend how RNNs work it is useful to consider its behavior explicitly by *unrolling* the RNN, as shown in Figure 2.28

An RNN applies the same model to each time step of the sequence or, equivalently, applies different models at each time step, which share their weights. This is similar to what CNNs do over space with convolutions, but is rather done over time with feedback connections.

The activation of an RNN (see Figure 2.28) at time t depends on the input at time t as well as on the information coming from the previous step $t - 1$. RNNs have a very simple internal structure, that usually amounts to applying some affine transformation to the input and to the previous output, and computing some non-linearity (typically a tanh) of their sum.

To train it it suffices to unroll the computation graph and use the backpropagation algorithm (see Section 2.1.4) to proceed from the most recent time step, backward in time. This algorithm is usually referred to as *Backpropagation through time (BPTT)*.

The problem of BPTT is that it requires the application of the chain rule all the way from the current time step to $t = 0$ to propagate the gradients through time. This results in a long chain of products that can easily go to infinity or become zero if the elements of the multiplication are greater or smaller than 1 respectively. These two issues, i.e., going to infinity and becoming zero, are known in the literature as *exploding gradient* and *vanishing gradient* respectively, and have been studied extensively in the past (see e.g., Hochreiter, 1991; Bengio *et al.*, 1994). The first one can be partially addressed by *clipping the gradient* when it becomes too large, but the second is not easy to overcome and can make training

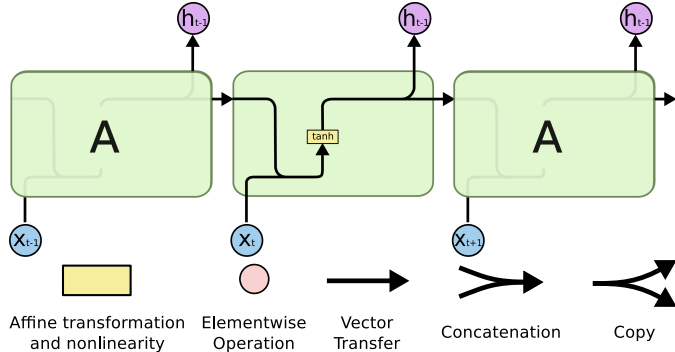


Figure 2.29: The internal structure of an RNN.

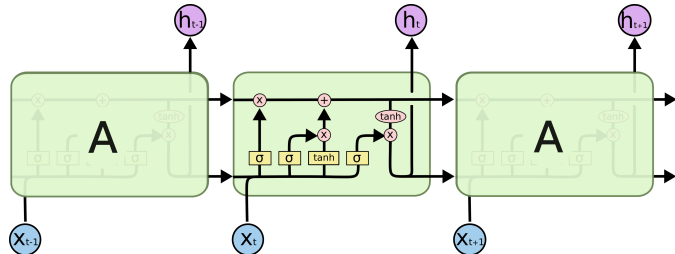


Figure 2.30: A Long Short Term Memory (LSTM).

these kind of models very hard if not impossible.

2.3.1 Long Short Term Memory

Long Short Term Memory (LSTM) networks (see Figure 2.30) have been proposed to solve (or at least alleviate) the problems of RNNs in modeling long term dependencies. LSTMs have been designed to have an internal memory, or *state*, that can be updated and consulted at each time step. As opposed to vanilla RNNs, this allows LSTMs to separate their output from the information they want to carry over to future steps.

Figure 2.31 highlights the internal memory path. It can be seen how the internal memory of the previous time step c_{t-1} is carried over to the current time step, where it is updated through a multiplicative and an additive interaction and concurs to determine the current state of the memory c_t . This is then, once again, propagated to the next time step.

LSTMs interact with memory through *gates*, computational nodes that determine the behavior of the model. The *forget gate* (Figure 2.32) determines how much of the previous step's memory to forget or, equivalently, how much of the previous state to retain. This is modeled through a sigmoid layer (depicted as σ) that takes the current input x_t and the output of the previous step h_{t-1} and produces an activation vector between 0 and 1

$$f_t = \sigma(\mathbf{W}_f \cdot [h_{t-1}, x_t] + b_f), \quad (2.20)$$

this activation is multiplied by the previous state c_{t-1} and results in an intermediate mem-

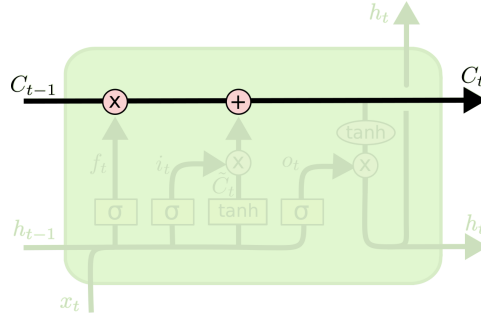


Figure 2.31: The internal state of LSTMs.

ory state where some of the activations can be weaker than those in \mathbf{c}_{t-1} and some others are potentially zeroed out.

The forget gate allows the LSTM to discard information that is not relevant anymore. Symmetrically, LSTMs have a mechanism to add new information to the memory. This behavior is controlled by an *input gate* (see Figure 2.33) that modulates the amount of the current input that is going to be stored in the memory. This operation is split over two computation paths: similarly to the forget gate, the input gate takes the current input \mathbf{x}_t and the output of the previous step \mathbf{h}_{t-1} and exploits a sigmoid layer to produce an activation vector between 0 and 1. Simultaneously, a tanh layer generates a state update $\tilde{\mathbf{c}}_t$ between -1 and 1 . This is governed by the equations

$$\begin{aligned}\mathbf{i}_t &= \sigma(\mathbf{W}_i \cdot [\mathbf{h}_{t-1}, \mathbf{x}_t] + \mathbf{b}_i), \\ \tilde{\mathbf{c}}_t &= \tanh(\mathbf{W}_c \cdot [\mathbf{h}_{t-1}, \mathbf{x}_t] + \mathbf{b}_c).\end{aligned}\quad (2.21)$$

The input gate modulates how much of this state update will be applied to the old state to generate the current state. The forget gate \mathbf{f}_t and the input gate \mathbf{i}_t , together with the state update $\tilde{\mathbf{c}}_t$ and the previous state \mathbf{c}_{t-1} fully determine the state at time t through

$$\mathbf{c}_t = \mathbf{f}_t \odot \mathbf{c}_{t-1} + \mathbf{i}_t \odot \tilde{\mathbf{c}}_t. \quad (2.22)$$

The last gate of LSTMs is the *output gate* (Figure 2.34) \mathbf{o}_t that, as the name reveals, manipulates the output of the LSTM at time t . The usual sigmoid layer determines the state of the output gate

$$\begin{aligned}\mathbf{o}_t &= \sigma(\mathbf{W}_o \cdot [\mathbf{h}_{t-1}, \mathbf{x}_t] + \mathbf{b}_o), \\ \mathbf{h}_t &= \mathbf{o}_t \odot \tanh(\mathbf{c}_t),\end{aligned}\quad (2.23)$$

and the memory resulting from the transformations due to the forget and input gates goes through a tanh nonlinearity and is multiplied by the output gate to finally produce the output.

Putting it all together, the equations that govern the behavior of an LSTM are

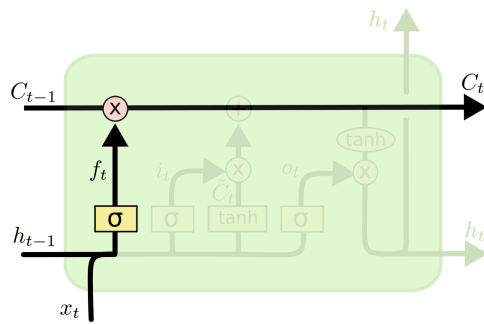


Figure 2.32: The LSTM forget gate.

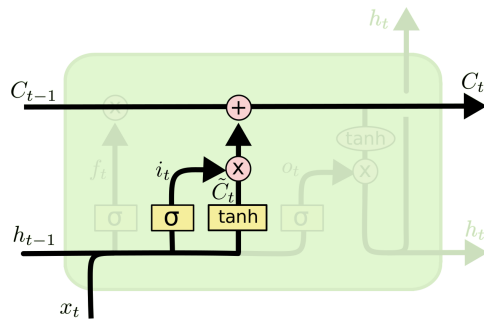


Figure 2.33: The LSTM input gate.

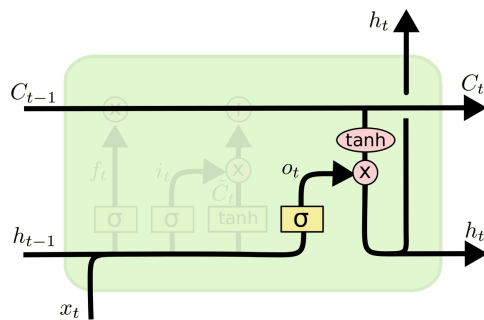


Figure 2.34: The LSTM output gate.

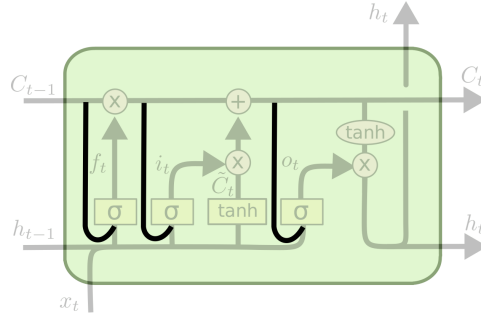


Figure 2.35: LSTM with peepholes.

$$\begin{aligned}
 \mathbf{i}_t &= \sigma(\mathbf{W}_i \cdot [\mathbf{h}_{t-1}, \mathbf{x}_t] + \mathbf{b}_i), \\
 \mathbf{f}_t &= \sigma(\mathbf{W}_f \cdot [\mathbf{h}_{t-1}, \mathbf{x}_t] + \mathbf{b}_f), \\
 \tilde{\mathbf{c}}_t &= \tanh(\mathbf{W}_c \cdot [\mathbf{h}_{t-1}, \mathbf{x}_t] + \mathbf{b}_c), \\
 \mathbf{c}_t &= \mathbf{f}_t \odot \mathbf{c}_{t-1} + \mathbf{i}_t \odot \tilde{\mathbf{c}}_t, \\
 \mathbf{o}_t &= \sigma(\mathbf{W}_o \cdot [\mathbf{h}_{t-1}, \mathbf{x}_t] + \mathbf{b}_o), \\
 \mathbf{h}_t &= \mathbf{o}_t \odot \tanh(\mathbf{c}_t).
 \end{aligned} \tag{2.24}$$

LSTMs with peepholes

Gers and Schmidhuber (2000) suggests one variant of LSTMs where the gates also have information about the state of the LSTM. Note that, as illustrated in Figure 2.35, the output gate peeps into \mathbf{c}_t , i.e., the state after the input and forget gate updates

$$\begin{aligned}
 \mathbf{i}_t &= \sigma(\mathbf{W}_i \cdot [\mathbf{h}_{t-1}, \mathbf{x}_t] + \mathbf{W}_{ic} \odot \mathbf{c}_{t-1} + \mathbf{b}_i), \\
 \mathbf{f}_t &= \sigma(\mathbf{W}_f \cdot [\mathbf{h}_{t-1}, \mathbf{x}_t] + \mathbf{W}_{fc} \odot \mathbf{c}_{t-1} + \mathbf{b}_f), \\
 \tilde{\mathbf{c}}_t &= \tanh(\mathbf{W}_c \cdot [\mathbf{h}_{t-1}, \mathbf{x}_t] + \mathbf{b}_c), \\
 \mathbf{c}_t &= \mathbf{f}_t \odot \mathbf{c}_{t-1} + \mathbf{i}_t \odot \tilde{\mathbf{c}}_t, \\
 \mathbf{o}_t &= \sigma(\mathbf{W}_o \cdot [\mathbf{h}_{t-1}, \mathbf{x}_t] + \mathbf{W}_{oc} \odot \mathbf{c}_{t-1} + \mathbf{b}_o), \\
 \mathbf{h}_t &= \mathbf{o}_t \odot \tanh(\mathbf{c}_t).
 \end{aligned} \tag{2.25}$$

LSTMs with coupled forget and input gates

Another variant of LSTMs (Greff *et al.*, 2015) replaces the input gate with $1 - \mathbf{f}_t$ (see Figure 2.36), so that the forget gate governs both behaviors. This boils down to forgetting only when a new input is going to be written. The modified state update equation is

$$\mathbf{c}_t = \mathbf{f}_t \odot \mathbf{c}_{t-1} + (1 - \mathbf{f}_t) \odot \tilde{\mathbf{c}}_t. \tag{2.26}$$

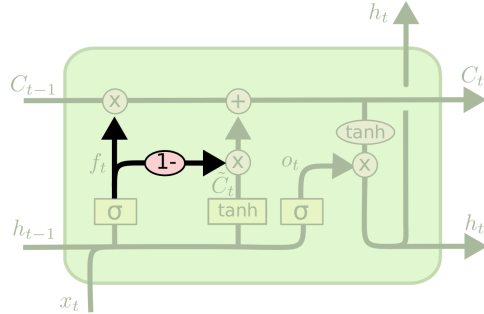


Figure 2.36: LSTM with coupled forget and input gate.

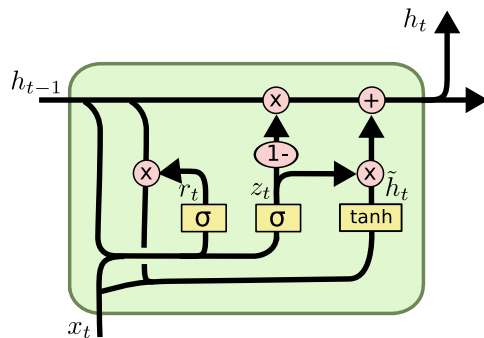


Figure 2.37: Gated Recurrent Units (GRUs).

2.3.2 Gated Recurrent Unit (GRU)

In 2014 Cho *et al.* (2014b) proposed a new kind of recurrent network called Gated Recurrent Unit (GRU) (see Figure 2.37) with less gates than LSTMs and a different internal structure. Along the lines of Section 2.3.1, in GRUs the forget and input gates are coupled into an *update gate* \mathbf{z}_t . The memory and output are also merged into a single state and the internal structure is modified to cope with these changes

$$\begin{aligned} \mathbf{z}_t &= \sigma(\mathbf{W}_z \cdot [\mathbf{h}_{t-1}, \mathbf{x}_t]), \\ \mathbf{r}_t &= \sigma(\mathbf{W}_r \cdot [\mathbf{h}_{t-1}, \mathbf{x}_t]), \\ \tilde{\mathbf{h}}_t &= \tanh(\mathbf{W}_o \cdot [\mathbf{r}_t \odot \mathbf{h}_{t-1}, \mathbf{x}_t]), \\ \mathbf{h}_t &= (1 - \mathbf{z}_t) \odot \mathbf{h}_{t-1} + (\mathbf{z}_t) \odot \tilde{\mathbf{h}}_t. \end{aligned} \tag{2.27}$$

The advantage of GRUs over LSTMs is the smaller number of gates that makes them less memory as well as computationally intense, which is often a critical aspect for ANNs. GRUs have been shown to perform as well as LSTMs in some settings (see (Chung *et al.*, 2014)).

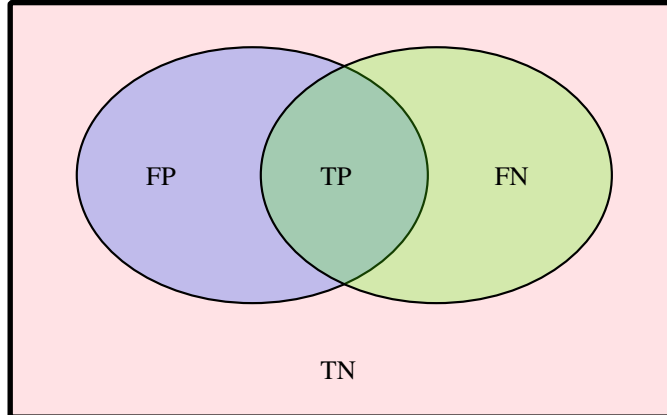


Figure 2.38: Intersection over Union (IoU). The blue set represents the values labeled as True by the algorithm, the green one represents the True values according to the ground truth, while the red ones are the False values according to the ground truth. The intersection between the green and the blue set are the values that are True and were labeled as such by the algorithm. These are called the True Positives (TP). The values wrongly labeled as positive are instead the False Positive (FP) while the ones wrongly labeled as negative are the False Negatives (FN). Finally, the values correctly labeled as False are the True Negatives (TN).

2.4 Metrics

Metrics allow to evaluate the effectiveness of a model on a given task and to compare its performance against the competing models. This section will introduce the most common metrics typically used to measure the performance of an algorithm in computer vision related tasks.

In classification tasks, where the algorithm is required to label the input as belonging to a class among a set of classes, one of the most used performance measure is *accuracy*. This metric corresponds to the ratio of correctly classified inputs to the total number of inputs. More formally, accuracy can be defined as

$$acc = \frac{TP + TN}{TP + TN + FP + FN}, \quad (2.28)$$

where *TP* corresponds to the *true positives*, i.e., the number of positive samples that were classified correctly as such; *TN* corresponds to the *true negatives*, i.e., the number of false samples that were correctly classified as such; *FP* corresponds to the *false positive*, i.e., the number of negative samples incorrectly classified as positive; and finally *FN* corresponds to the *false negatives*, i.e., the number of positive samples incorrectly classified as positive.

One shortcoming of accuracy is that it can poorly reflect the performance on the task. Consider for example a challenge where the goal is to distinguish between foreground and background, or equivalently to detect the core part of a visual scene. If the images are such that the foreground is typically much smaller than the background, a trivial way to obtain fairly high accuracy is to always classify the whole image as background. This fixed

heuristic that ignores the input image altogether can achieve 70% or even 80% accuracy on some datasets.

In detection or segmentation tasks, i.e., where the goal is to locate an object of interest in an image by either inscribing it into a bounding box or by selecting each pixel that belongs to the object, a more accurate metric is *Intersection over Union (IoU)*. This metric penalizes wrong classifications and is computed as the ratio of the intersection to the union of the area classified as positive by the algorithm and the one that is actually positive according to the ground truth. This is equivalent to

$$IoU = \frac{TP}{TP + FN + FP}, \quad (2.29)$$

and is also known as *Jaccard index* in the literature.

CHAPTER 3

Recurrent Neural Networks for Object Classification

Classification is a broad task that consists in predicting to which category an input belongs to, out of some k given categories. The system is usually required to compute a function $f : \mathbb{R}^d \rightarrow \{\Omega_0, \dots, \Omega_{(k-1)}\}$ that assigns each input to a class Ω_i . This can be thought as a discrimination task, where the algorithm is expected to learn similarities and differences between categories in order to characterize each class.

Some examples of classification are spam detection (classify a message as being spam or not), credit card fraud detection (identify if a transaction is legit or not), Optical Character Recognition (OCR) (convert hand-written text to an electronic document, by classifying each character), speech understanding (given an utterance from a user, detect the sentence that was pronounced), medical diagnosis (given the symptoms predict the illness and suggest a cure), stock trading (determine if a stock should be bought, held or sold, from current and historical data), shape detection (classify a hand-drawn drawing from, e.g., a touch screen, as a specific shape) and sentiment analysis (given a text, classify it as being positive, neutral or negative)

Object recognition is an instance of the classification task that takes an image as an input and is expected to return the id of the main class represented in the image. This is usually achieved by computing the probability distribution over the classes – i.e., the confidence of the algorithm for each class to be the main class in the scene – and then picking the one with highest score. One downside of this method is that small and big mistakes are penalized the same, i.e., the prediction is considered wrong whether the right class is the

second most probable class in the distribution or is considered extremely unlikely by the algorithm. For this reason, some competitions such as e.g., ImageNet (Deng *et al.*, 2009; Russakovsky *et al.*, 2014), propose multiple challenges where the top-3 or top-5 guesses are considered, i.e., where an image is considered correctly predicted if the correct class is in the top 3 or 5 guesses of the network.

Traditionally the computer vision community used to address this task with heavily hand-engineered systems that typically resorted to finding easily detectable elements in the image – such as e.g. edges or corners – and computing a descriptor of the surrounding patch. Many detectors (Dufournaud *et al.*, 2000; Harris and Stephens, 1988; Mikolajczyk and Schmid, 2001; Lowe, 2004; Mikolajczyk and Schmid, 2005) and descriptors (Lowe, 1999; Mikolajczyk and Schmid, 2005; Belongie *et al.*, 2002) have been proposed to this end, until in 2012 a deep convolutional neural network markedly shifted the balance towards learned ANNs (Krizhevsky *et al.*, 2012a). Since then CNN-based models dominated the object recognition scene.

This chapter presents ReNet, one of the main contributions of this thesis. The ReNet model is a deep neural network architecture for object recognition, based on recurrent neural networks. The main idea behind this model is to propose an alternative to the typical CNN-based approach to object classification problems. In fact, the ReNet model replaces ubiquitous convolution+pooling layers of deep CNNs with four recurrent neural networks that sweep horizontally and vertically in both directions across the image.

The following sections motivate the model in the context of the state of the art at the time it was conceived, describe the ReNet model in detail and present the results of its evaluation on three widely-used object recognition benchmarks, namely MNIST (LeCun *et al.*, 1999), CIFAR-10 (Krizhevsky and Hinton, 2009) and SVHN (Netzer *et al.*, 2011). The experiments reveal that the ReNet model performs comparably to convolutional neural networks on all these datasets, suggesting the potential of RNNs as a competitive alternative to the conventional deep convolutional neural networks for image related tasks.

3.1 Motivation

Convolutional neural networks (CNN, Fukushima, 1980; LeCun *et al.*, 1989) have become the method of choice for object recognition after the impressive improvement on the state of the art by Krizhevsky *et al.* (2012a). CNNs have proven to be successful at a variety of benchmark problems including, but not limited to, handwritten digit recognition (see, e.g., Ciresan *et al.*, 2012b), natural image classification (see, e.g., Lin *et al.*, 2014a; Simonyan and Zisserman, 2015; Szegedy *et al.*, 2014a), house number recognition (see, e.g., Goodfellow *et al.*, 2014), traffic sign recognition (see, e.g., Ciresan *et al.*, 2012a), as well as for speech recognition (see, e.g., Abdel-Hamid *et al.*, 2012; Sainath *et al.*, 2013; Tóth, 2014). Furthermore, image representations from CNNs trained to recognize objects on a large set of more than one million images (Simonyan and Zisserman, 2015; Szegedy *et al.*, 2014a) have been found to be extremely helpful in performing other computer vision tasks such as image caption generation (see, e.g., Vinyals *et al.*, 2014; Xu *et al.*, 2015), video description generation (see, e.g., Yao *et al.*, 2015b) and object localization/detection (see, e.g., Sermanet *et al.*, 2014).

While CNNs have been especially successful in computer vision, recurrent neural networks (RNN) have become the method of choice for modeling sequential data, such as

text and sound. Natural language processing (NLP) applications include language modeling (see, e.g., Mikolov, 2012), and machine translation (Sutskever *et al.*, 2014; Cho *et al.*, 2014a; Bahdanau *et al.*, 2015). Other popular areas of application include offline handwriting recognition/generation (Graves and Schmidhuber, 2009; Graves *et al.*, 2008; Graves, 2013) and speech recognition (Chorowski *et al.*, 2014; Graves and Jaitly, 2014). RNNs have also been used together with CNNs in speech recognition (Sainath *et al.*, 2015). The recent revival of RNNs has largely been due to advances in learning algorithms (Pascanu *et al.*, 2013; Martens and Sutskever, 2011) and model architectures (Pascanu *et al.*, 2014; Cho *et al.*, 2014a).

The architecture of ReNet is related and inspired by this earlier work, but relies on purely uni-dimensional RNNs coupled in a novel way, rather than on a multi-dimensional RNN. The basic idea behind the ReNet model is to replace each convolutional layer (with convolution+pooling making up a layer) in the CNN with four RNNs (i.e., two bidirectional RNNs) that sweep over lower-layer features in different directions: (1) bottom to top, (2) top to bottom, (3) left to right and (4) right to left. The recurrent layer ensures that each feature activation in its output is an activation at the specific location *with respect to the whole image*, in contrast to the usual convolution+pooling layer which only has a local context window. The lowest layer of the model sweeps over the input image, with subsequent layers operating on extracted representations from the layer below, forming a hierarchical representation of the input.

Graves and Schmidhuber (2009) have demonstrated an RNN-based object recognition system for offline Arabic handwriting recognition. The main difference between ReNet and the model of Graves and Schmidhuber (2009) is that it uses the usual sequence RNN, instead of the multidimensional RNN. The way ReNet has been conceived allows in fact to capture the context of the image without being forced to resort to multidimensional RNNs, indeed the latter two RNNs (or, equivalently, the last bidirectional RNN), work on the hidden states computed by the first two RNNs (or the first bidirectional RNN). This allows to use plain RNNs instead of the more complex multidimensional ones, while making each output activation of the layer be computed with respect to the whole input image.

One important consequence of the proposed approach compared to the multidimensional RNN is that the number of RNNs at each layer scales linearly with respect to the number of dimensions d of the input image ($2d$). A multidimensional RNN, on the other hand, requires an exponential number of RNNs at each layer (2^d). Furthermore, the proposed variant is more easily parallelizable, as each RNN is dependent only along a horizontal or vertical sequence of patches. This architectural distinction results in the ReNet model being much more amenable to distributed computing than that of Graves and Schmidhuber (2009).

3.2 Model Description

Let us denote by $\mathbf{X} = \{x_{i,j}\}$ the input image or the feature map from the previous layer, where $\mathbf{X} \in \mathbb{R}^{w \times h \times c}$ with w , h and c the width, height and number of channels, or the feature dimensionality, respectively. Given a receptive field (or patch) size of $w_p \times h_p$, the image \mathbf{X} is split into a set of $I \times J$ (non-overlapping) patches $P = \{\mathbf{p}_{i,j}\}$, where $I = \frac{w}{w_p}$, $J = \frac{h}{h_p}$ and $\mathbf{p}_{i,j} \in \mathbb{R}^{w_p \times h_p \times c}$ is the (i, j) -th patch of the input image. The first index i is

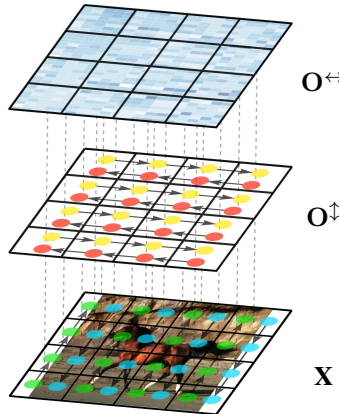


Figure 3.1: A ReNet layer. The green and blue dots on the input image/feature map represent the steps of f^{\uparrow} and f^{\downarrow} respectively. On the concatenation of the resulting feature maps, the two RNNs f^{\rightarrow} (yellow dots) and f^{\leftarrow} (red dots) are subsequently swept. The output of the feature maps are finally concatenated to form the output of the ReNet layer; depicted as a blue heatmap in the figure.

the horizontal index and the other index j is the vertical index.

First, the image is swept vertically with two RNNs, with one RNN working in a bottom-up direction and the other working in a top-down direction. Each RNN takes as an input one (flattened) patch at a time and updates its hidden state c^* (in the usual way, depending on the RNN implementation), working *along each column j* of the split input image \mathbf{X} to produce two output vectors o^{\uparrow} and o^{\downarrow} defined as follows

$$\mathbf{o}_{i,j}^{\uparrow} = f^{\uparrow}(\mathbf{c}_{i,j-1}^{\uparrow}, \mathbf{p}_{i,j}), \text{ for } j = 1, \dots, J, \quad (3.1)$$

$$\mathbf{o}_{i,j}^{\downarrow} = f^{\downarrow}(\mathbf{c}_{i,j+1}^{\downarrow}, \mathbf{p}_{i,j}), \text{ for } j = J, \dots, 1. \quad (3.2)$$

Note that the functions f^{\uparrow} and f^{\downarrow} return the activation of the recurrent hidden unit, and may be implemented either as a simple tanh layer, as a gated recurrent layer (Cho *et al.*, 2014a) or as a long short-term memory layer (Hochreiter and Schmidhuber, 1997), as detailed in Section 2.3, Section 2.3.1 and Section 2.3.2).

After this vertical, bidirectional sweep, the intermediate hidden states $\mathbf{o}_{i,j}^{\uparrow}$ and $\mathbf{o}_{i,j}^{\downarrow}$ are concatenated at each location (i, j) to get a composite feature map $\mathbf{O}^{\dagger} = \{\mathbf{o}_{i,j}^{\uparrow}, \mathbf{o}_{i,j}^{\downarrow}\}_{i=1, \dots, I}^{j=1, \dots, J}$, where each element $\mathbf{o}_{i,j}^{\dagger} \in \mathbb{R}^{2d}$ and d is the number of recurrent units. Each $\mathbf{o}_{i,j}$ is now the activation of a feature detector at the location (i, j) with respect to all the patches in the j -th column of the original input ($\mathbf{p}_{i,j}$ for all i).

Next, the obtained composite feature map \mathbf{O}^{\dagger} is swept horizontally with two different RNNs (f^{\rightarrow} and f^{\leftarrow}). In a similar manner as for the vertical sweep, these RNNs work along each row of \mathbf{O}^{\dagger} and produce an output feature map $\mathbf{O}^{*\leftrightarrow} = \{\mathbf{o}_{i,j}^{*\leftrightarrow}\}$, where $\mathbf{o}_{i,j}^{*\leftrightarrow} \in \mathbb{R}^{2d}$. In this representation, each vector $\mathbf{o}_{i,j}^{*\leftrightarrow}$ represents the features of the original image patch $\mathbf{p}_{i,j}$ in the context of the whole image.

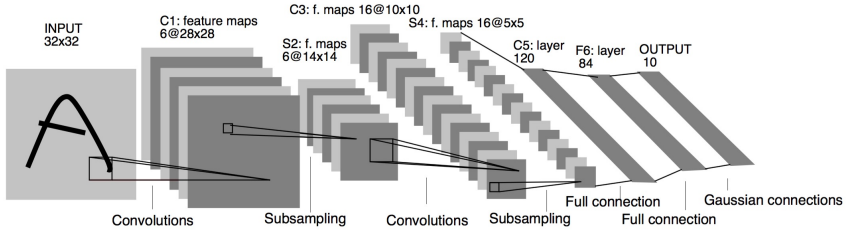


Figure 3.2: The LeNet network.

This is a critical feature of this model, in fact just one layer (to be precise, two sub-layers) allows to capture the full context of the image, irrespective of the image size. This is possible thanks to the (potential) ability of RNNs to store in their memory any information that is relevant to retain the context of the part of the image that has been processed. The first two RNNs capture the vertical dependencies in both directions. By reading their composite feature map, the second pair of RNNs has access in each position to a "summary" of the corresponding row. This is processed horizontally, to capture the missing dependencies between rows. This intra- and inter-row processing results in a final composite feature map where each position is specific to a pixel (or patch) of the image but has information on the full image. Conversely, to span over the whole image with CNN-based architectures would require many more layers, whose number depend on the size of the input image.

Even if each ReNet layer captures the full input context, it is clearly still possible to stack multiple ReNet layers on top of each other into a deep network. Let us denote by ϕ the function from the input image (or feature map) X of one ReNet layer to the output feature map O^\leftarrow (see Figure 3.1 for a graphical illustration). It is possible to compute a composition of functions $\Phi = \phi_1(\phi_2(\phi_3(\dots)))$ by stacking multiple ReNet layers, to capture increasingly complex features of the input image. After any number of recurrent layers are applied to an input image, the activation at the last recurrent layer may be flattened and fed into a differentiable classifier to solve an object recognition task. The experiments on this model, presented in Section 3.3, used several fully-connected layers followed by a softmax classifier, as shown in Figure 3.6.

The deep ReNet is a smooth, continuous function, and the parameters (those from the RNNs as well as from the fully-connected layers) can be estimated by the stochastic gradient descent algorithm with the gradient computed by backpropagation algorithm described in Section 2.1.4 to maximize the log-likelihood.

3.2.1 Differences between LeNet and ReNet

This section will use LeNet (see Figure 3.2) as a reference to the canonical convolutional neural network as shown by LeCun *et al.* (1989). There are many similarities and differences between the ReNet model and a convolutional neural network. The main key points of comparison will be highlighted in the following.

At each layer, both networks apply the same set of filters to patches of the input image or of the feature map generated by the layer below. ReNet, however, propagates information through lateral connections that span across the whole image, while LeNet exploits

local information only. The lateral connections should help extract a more compact feature representation of the input image at each layer, which can be accomplished by the lateral connections removing/resolving redundant features at different locations of the image. This should allow ReNet resolve small displacements of features across multiple consecutive patches. Also, the lack of this type of lateral connection in LeNet may lead to many more levels of convolution+pooling layers in order to detect redundant features from different parts of the image.

LeNet max-pools the activations of each filter over a small region to achieve local translation invariance. In contrast, the proposed ReNet does not use any pooling due to the existence of learned lateral connections. The lateral connection in ReNet can emulate the local competition among features induced by the max-pooling in LeNet. This does not mean that it is not possible to use max-pooling in ReNet. The use of max-pooling in the ReNet could be helpful in reducing the dimensionality of the feature map, resulting in a lower computational cost.

Max-pooling as used in LeNet may prove problematic when building a convolutional autoencoder whose decoder is an inverse¹ of LeNet, as the max operator is not invertible. The proposed ReNet is end-to-end smooth and differentiable, making it more suited to be used as a decoder in the autoencoder or any of its probabilistic variants (see e.g., Kingma and Welling, 2014).

In some sense, each layer of the ReNet can be considered as a variant of a usual convolution+pooling layer, where pooling is replaced with lateral connections, and convolution is done without any overlap. Similarly, Springenberg *et al.* (2014) recently proposed a variant of a usual LeNet which does not use any pooling. They used convolution with a larger stride to compensate for the lack of dimensionality reduction by pooling at each layer. However, this approach still differs from the proposed ReNet in the sense that each feature activation at a layer is only with respect to a subset of the pixels of the input image rather than the whole input image.

The main disadvantage of ReNet is that it is not easily parallelizable, due to the sequential nature of the recurrent neural network. LeNet, on the other hand, is highly parallelizable due to the independence of computing activations at each layer. The introduction of sequential, lateral connections, however, may result in more efficient parametrization, requiring a smaller number of parameters with overall fewer computations, although this needs to be further explored. Note that this limitation on parallelization applies only to model parallelism, and any technique for data parallelism may be used for both the proposed ReNet and the LeNet.

3.3 Experiments

3.3.1 Datasets

The ReNet model has been evaluated on three widely-used benchmark datasets; MNIST, CIFAR-10 and the Street View Housing Numbers (SVHN). This section describes each dataset in detail.

¹All the forward arrows from the input to the output in the original LeNet are reversed.



Figure 3.3: Some digits from the MNIST dataset.

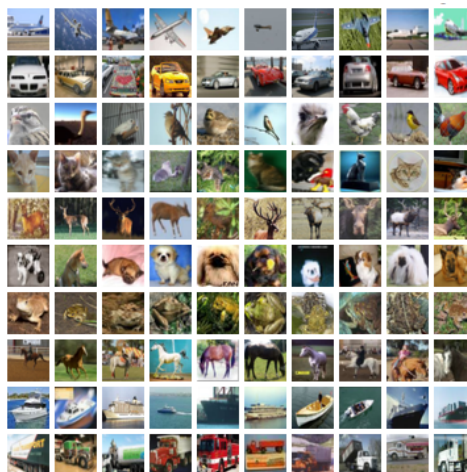


Figure 3.4: Some samples of the 10 classes of the CIFAR-10 dataset.

MNIST

The MNIST dataset (LeCun *et al.*, 1999) consists of 70,000 handwritten digits from 0 to 9, centered on a 28×28 square canvas (see Figure 3.3 for some samples). Each pixel value represents the grayscale intensity in the range $[0, 255]$.² It is customary to split this dataset into 50,000 training samples, 10,000 validation samples and 10,000 test samples. For a fair comparison, the results reported in Section 3.3.4 were obtained following the standard split.

²Each pixel has been normalized to $[0, 1]$ by dividing it with 255.



Figure 3.5: Some samples of housing numbers from the SVHN dataset.

CIFAR-10

The CIFAR-10 dataset (Krizhevsky and Hinton, 2009) is a curated subset of the 80 million tiny images dataset (see Figure 3.4 for some samples), originally released by Torralba *et al.* (2008). CIFAR-10 contains 60,000 images each of which belongs to one of ten categories: airplane, automobile, bird, cat, deer, dog, frog, horse, ship and truck. Each image is 32 pixels wide and 32 pixels high with 3 color channels (red, green and blue.) Following the standard procedure, in the reported experiments the dataset was split into 40,000 training, 10,000 validation and 10,000 test samples. Furthermore, zero-phase component analysis (ZCA) was applied and each pixel was normalized to have zero-mean and unit-variance across the training samples, as suggested by Krizhevsky and Hinton (2009).

Street View House Numbers

The Street View House Numbers dataset (Netzer *et al.*, 2011) consists of cropped images representing house numbers captured by Google StreetView vehicles as a part of the Google Maps mapping effort. These images consist of digits 0 through 9 with values in the range of [0, 255] in each of 3 red-green-blue color channels (see Figure 3.5 for some samples). Each image is 32 pixels wide and 32 pixels high giving a sample dimensionality (32, 32, 3). The number of samples used for the training, validation, and test sets is 543,949, 60,439, and 26,032 respectively. Every channel in each pixel was normalized to have zero-mean and unit-variance across the training samples.

3.3.2 Data Augmentation

It has been long known that augmenting training data often leads to better generalization (see, e.g., Krizhevsky *et al.*, 2012a). Many of the reported SOTA results were obtained using a mix of these techniques, for example (Goodfellow *et al.*, 2013) reports a 1.52% improvement on CIFAR10 by adding translation and reflections; (Simard *et al.*, 2003)

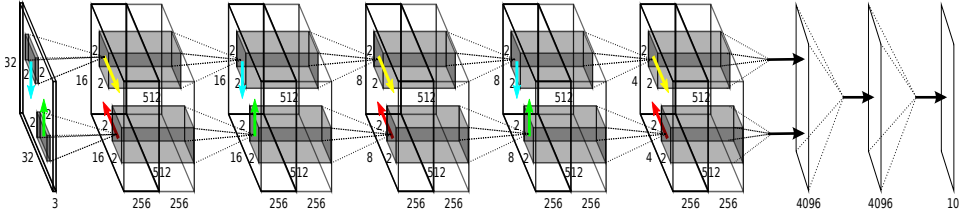


Figure 3.6: The ReNet network used for SVHN classification.

uses elastic distortion on MNIST; (Wan *et al.*, 2013) applies cropping, flipping, scaling, rotating on SVHN and CIFAR10. The results reported in Section 3.3.4 were all obtained employing two primary data augmentations: *flipping* and *shifting*.

For the flipping data augmentation, the model was presented with samples that were either flipped horizontally with 25% chance, or vertically with 25% chance, or left unchanged. This technique allows the model to observe “mirror images” of the original images of the dataset during training, increasing the amount of training data. On SVHN and MNIST only horizontal flipping was used to prevent the case where an image labelled 6 is flipped in both directions, becoming a 9.

In the case of shifting two policies were adopted. The images were either shifted by 2 pixels to the left (25% chance), 2 pixels to the right (25% chance) or left as they were. After this first processing, the images were further shifted either by 2 pixels to the top (25% chance), 2 pixels to the bottom (25% chance) or left as they were. This two-step procedure makes the model more robust to slight shifting of an object in the image. The shifting was done without pre-padding the borders of the image, but rather preserving the original size by dropping the pixels which are shifted out of the input and shifting in zeros on the opposite side.

Exploiting data augmentation techniques with the ReNet model led to a 16% improvement in test performance on MNIST and to less pronounced gains on the other datasets. The choice of whether to apply these augmentation procedures on each dataset was chosen on a per-case basis in order to maximize validation performance.

3.3.3 Experimental settings

The principal parameters that define the architecture of the ReNet model are the number of ReNet layers (N_{RE}), their corresponding receptive field sizes ($w_p \times h_p$) and feature dimensionality (d_{RE}), the number of fully-connected layers (N_{FC}) and their corresponding numbers (d_{FC}) and types (f_{FC}) of hidden units. Table 3.1 summarizes the settings of the hyperparameters that performed best on the validation set of the studied datasets. Figure 3.6 is a graphical illustration of the model selected by cross-validating on the validation set for the SVHN dataset.

Training

All the networks have been trained using a recently proposed adaptive learning rate algorithm, called Adam (Kingma and Ba, 2014b). In order to reduce overfitting dropout (Srivastava *et al.*, 2014) was applied after each layer, including both the ReNet layers (after

	MNIST	CIFAR-10	SVHN
N_{RE}	2	3	3
$w_p \times h_p$	[2 × 2]–[2 × 2]	[2 × 2]–[2 × 2]–[2 × 2]	[2 × 2]–[2 × 2]–[2 × 2]
d_{RE}	256–256	320–320–320	256–256–256
N_{FC}	2	1	2
d_{FC}	4096–4096	4096	4096–4096
f_{FC}	$\max(0, x)$	$\max(0, x)$	$\max(0, x)$
Flipping	no	yes	no
Shifting	yes	yes	yes

Table 3.1: Model architectures used in the experiments. Each row shows respectively the number of ReNet layers, the size of the patches, the number of neurons of each ReNet layer, the number of fully connected layers, the number of neurons of the fully connected layers, their activation function and the data augmentation procedure employed.

the horizontal and vertical sweeps) and the fully-connected layers. The input layer was also corrupted by masking out each pixel with probability 0.2. Finally, each optimization run was early stopped based on validation error.

Note that the results reported in Section 3.3.4 were obtained without retraining on the joint training and validation sets. This is a common technique exploited by many works in the literature to boost the performance of the best model, selected after a full training on the training set and early stopping on the validation performance. There is no reason not to think that this would further improve the reported results, but this work was mainly conceived as a proof of concept rather than to stress on the absolute performance achievable on the selected datasets. This, as well as e.g., ensembling multiple models, can be seen as one of the many potential areas of exploration for further work in case maximum performance is sought.

3.3.4 Results

Table 3.2, presents the results of ReNet on three datasets, along with previously reported results. It is clear that ReNet performs comparably to deep convolutional neural networks which are the *de facto* standard for object recognition. This suggests that ReNet is a viable alternative to convolutional neural networks (CNN), even on tasks where CNNs have historically dominated. However, it is important to notice that ReNet does not outperform state-of-the-art convolutional neural networks on any of the three benchmark datasets, which calls for more research in the future.

3.4 Discussion

The ReNet model successfully proved that RNN-based model can and should be explored also in contexts where traditional CNN-based model have established the state of the art for a long time, such as object recognition. Many aspects of RNN-based models applied to this context remain to be studied in more depth, some of which will be outlined in the

Test Error	Model	Test Error	Model
0.28%	(Wan <i>et al.</i> , 2013)★	4.5%	(Graham, 2014a)★
0.31%	(Graham, 2014b)★	6.28%	(Graham, 2014b)★
0.35%	(Ciresan <i>et al.</i> , 2010)	8.8%	(Lin <i>et al.</i> , 2014a)★
0.39%	(Mairal <i>et al.</i> , 2014)★	9.35%	(Goodfellow <i>et al.</i> , 2013)★
0.39%	(Lee <i>et al.</i> , 2014)★	9.39%	(Springenberg and Riedmiller, 2013)★
0.4%	(Simard <i>et al.</i> , 2003)★	9.5%	(Snoek <i>et al.</i> , 2012)★
0.44%	(Graham, 2014a)★	11%	(Krizhevsky <i>et al.</i> , 2012a)★
0.45%	(Goodfellow <i>et al.</i> , 2013)★	11.10%	(Wan <i>et al.</i> , 2013)★
0.45%	ReNet	12.35%	ReNet
0.47%	(Lin <i>et al.</i> , 2014a)★	15.13%	(Zeiler and Fergus, 2013)★
0.52%	(Azzopardi and Petkov, 2013)	15.6%	(Hinton <i>et al.</i> , 2012)★
(a) MNIST		(b) CIFAR-10	
		Table 3.2: Generalization errors obtained by the proposed ReNet along with those reported by previous works on each of the three datasets. For a fair comparison, only results obtained by a single model are listed, i.e., no ensembling of multiple models is reported. In the case of SVHN, only models trained on the Format 2 (cropped digits) dataset are reported. ★ denotes a convolutional neural network.	
Test Error	Model		
1.92%	(Lee <i>et al.</i> , 2014)★		
2.23%	(Wan <i>et al.</i> , 2013)★		
2.35%	(Lin <i>et al.</i> , 2014a)★		
2.38%	ReNet		
2.47%	(Goodfellow <i>et al.</i> , 2013)★		
2.8%	(Zeiler and Fergus, 2013)★		
(c) SVHN			

rest of this section.

Choice of recurrent units

The proposed architecture is independent of the chosen recurrent units. The preliminary experiments on this model showed that gated recurrent units, either the GRU or the LSTM, outperform a usual sigmoidal unit (affine transformation followed by an element-wise sigmoid function.) This indirectly confirms that the model exploits long-term dependencies across an input image, and the gated recurrent units help capture these dependencies.

Choice of the topology

A similar but less effective architecture would have been to flatten the matrix of patches into a vector and process them with a singular bidirectional RNN from the top-left patch to the bottom-right one. This alternative presents two shortcomings: first, the network would have had to learn the dependency between vertically adjacent pixels implicitly – a much harder task than capturing the dependency between pixels explicitly close in the input provided to the layer; second, after a successful training, the network would have implicitly learned the size of its input (i.e., that every J patches are correlated), thus constraining the trained model to work at inference time on images of the exact same resolution.

Analysis of the trained ReNet

The ReNet model has been only evaluated in a quantitative fashion. However, the accuracy values on the test sets do not reveal what kind of image structures the ReNet has captured in order to perform object recognition. Due to the large differences between ReNet and LeNet discussed in Section 3.2.1, it can be expected that the internal behavior of ReNet will differ from that of LeNet significantly. Further investigation along the line of (Zeiler and Fergus, 2014b) is needed, as well as exploring ensembles that combine RNNs and CNNs for bagged prediction.

Computationally Efficient Implementation

As discussed in Section 3.2.1, the proposed ReNet is less parallelizable due to the sequential nature of the recurrent neural network (RNN). Although this sequential nature cannot be addressed directly, our construction of ReNet allows the forward and backward RNNs to be run independently from each other, which allows for parallel computation. Furthermore, it is possible to exploit the many parallelization tricks widely used for training convolutional neural networks such as parallelizing fully-connected layers (Krizhevsky, 2014), having separate sets of kernels/features in different processors (Krizhevsky *et al.*, 2012a) and exploiting data parallelism.

CHAPTER 4

Recurrent Neural Networks for Semantic Segmentation

Chapter 3 introduced the ReNet model, an RNN-based model for object recognition. The ReNet model scans the image horizontally and vertically with 4 RNNs at each layer and is able to capture the full context of the input with just one layer thanks to a sophisticated interaction of the inner RNNs. This allows activations to be local yet conditioned on global information, an ideal setting for semantic segmentation.

Semantic segmentation is the task of labeling each pixel of an image with the class it belongs to. In an urban scene scenario, this would mean, e.g., to label all the pixels of all the cars in the image as belonging to the "car class", every pixel of all the pedestrians in the image as belonging to the pedestrian class, and so on.

This is a very difficult task for many reasons: classifying pixels requires to acquire both a global understanding of the scene, as well as a very detailed and spatially precise characterization of each object; drawing segmentation masks is very time consuming, which makes it difficult and expensive to collect big datasets; labels are often subject to personal judgement, in fact different people tend to have different degrees of accuracy on small details and contours and at the same time, it is hard to define a clear separation path between the object and the background sometimes (e.g., the leafs of a tree)

Segmentation is of paramount importance in many fields that range from autonomous driving – where the objects in the scene have to be correctly and precisely detected to allow the navigation in the environment – to medical applications such as magnetic resonance (MR) images analysis, ultrasonography, surgery robots control or polyps detection

Chapter 4. Recurrent Neural Networks for Semantic Segmentation

in colonoscopies.

Semantic segmentation is a broad area of research that encompasses many subtasks, which depend on the kind of images at hand as well as on the domain of application. The input is usually an image that can be in grayscale or colors. In some cases it is required to segment a single image, while sometimes the task is simplified by the presence of stereo images pairs that allow to exploit the disparity information, i.e., the difference between the two images due to the displacement of the cameras. This extra information can be used to compute a (usually noisy) depth map that can be very helpful to distinguish between objects that are overlapping in the 2D image, but can be easily separated on the depth axis. Similarly, depth sensors that produce RGB-D data can be used in this fashion to improve the segmentation in some domains. An analogous but slightly different case is that of sparse 3D data, where the depth information of some points is provided but the measurements are not densely placed in the input space. Finally, a related yet distinct setting is the one of cosegmentation, where multiple images of the same scene have to be segmented. Ideally one would want the segmentation masks to be consistent across different images. This extra constraint can be used as a prior to improve those parts that are difficult to segment in one image but trivial in another.

Historically the computer vision community has tackled this problem by building very specialized hand-engineered algorithms that relied heavily on very specific domain knowledge. Many of these methods addressed the segmentation problem looking for highly discriminative local and global features, such as pixel color (possibly in multiple color spaces, see e.g., (Cheng *et al.*, 2001)); histogram of oriented gradients (HoG) (Dalal and Triggs, 2005; Bourdev *et al.*, 2010; Felzenszwalb *et al.*, 2010) – where the input space is described with a discrete function that maps locations to colors and the gradient on the two axes is used to produce a histogram representation of each patch – or the similar bag of visual words (BOV) (Csurka *et al.*, 2004); the many local patch descriptors such as SIFT (Lowe, 2004), SURF (Bay *et al.*, 2008), Kaze (Alcantarilla *et al.*, 2012), CenSurE (Agrawal *et al.*, 2008), BRISK (Leutenegger *et al.*, 2011); poselets (Brox *et al.*, 2011; Bourdev *et al.*, 2010), that annotate keypoints of the object to be detected; dimensionality reduction methods (see e.g., principal components analysis (PCA) (Smith, 2002; Shlens, 2014; Chen *et al.*, 2011) and ZCA whitening (see e.g., (Krizhevsky and Hinton, 2009) for a good introduction)).

Other classical methods for semantic segmentation include clustering algorithms (see e.g., Hartigan, 1975; Chen *et al.*, 1998), that group pixels in clusters based on some metrics; graph-based methods that build a graph with pixels as nodes and some measure of dissimilarity as weight for the edges (see e.g., Carreira and Sminchisescu, 2010; Felzenszwalb and Huttenlocher, 2004); active contour models (ACMs) that segment the image roughly along edges and minimize an energy function that imposes a smoothness prior on the segmentation (see e.g., Atkins and Mackiewich, 1998; Kass *et al.*, 1988); watershed segmentation, that takes the intensity values of grayscale images as a height map and imagines to drop water on it, filling regions with similar heights until the rise of the water connects two basins and a watershed is found (see e.g., Roerdink and Meijster, 2000). Finally, many segmentation strategies base on two very well known and studied algorithms in the literature, namely random decision forests (Ho, 1995; Shotton *et al.*, 2008) and support vector machines (SVMs) (Burges, 1998; Yang *et al.*, 2012).

Many of these methods rely on a sliding-window approach, i.e., a classifier that seg-

ments a window of fixed size that moves across the image processing it in every location. The downside of this approach is that the classification is performed locally and the full context is usually not captured easily.

The typical strategy to contrast this lack of high level consistency is to pair the segmentation algorithm with a Markov Random Field (MRF) (see e.g., Blake *et al.*, 2011; Murphy, 2012; Moser *et al.*, 2012) or a Conditional Random Field (CRF) (see e.g., Russell *et al.*, 2009; He *et al.*, 2004; Shotton *et al.*, 2006). These methods can be implemented in several ways, but usually impose a local prior on each location and consistency constraints on pairs or sets of positions. The underlying intuition of these methods is that the prediction in every location should be consistent with the one of the neighbouring locations. The pattern of these dependencies can vary across different implementations and is usually defined based on specific domain knowledge. For a complete survey on segmentation, see (Thoma, 2016).

This chapter introduces the second main contribution of this work. The ReSeg model (Visin *et al.*, 2016) builds on ReNet (see Chapter 3) to tackle the task of semantic segmentation. The primary motivation behind ReSeg is to exploit the peculiar structure of ReNet in order to capture the underlying semantic of the input image and use it to drive the prediction in each location, i.e., pixel. Thanks to the strong lateral connections built in the model, ReSeg is able to capture the *global* scene depicted in the image and exploit it to perform fine, high resolution, semantic segmentation focusing on *local* details.

This work extends the preliminary results of (Visin *et al.*, 2015) modifying and extending the ReNet model to the more ambitious task of object segmentation. The performance of the proposed model are tested on some of the historically most used datasets in this field, namely the Weizmann Horse dataset (Borenstein, 2004), the Oxford Flowers 17 dataset (Nilsback and Zisserman, 2006) and the more recent and challenging Camvid dataset (Brostow *et al.*, 2009, 2008). The first two are tackled in a foreground/background segmentation setting as a proof of concept for the proposed ReSeg architecture. The performance of the model is then tested on the full segmentation task on Camvid, a standard benchmark of urban scenes.

The experiments show that the proposed adaptation of the ReNet for pixel-level object segmentation performs successfully on the object segmentation task achieving state-of-the-art performance in all three datasets and may have further applications in other structured prediction problems.¹ Furthermore, the ReNet and ReSeg architectures could be easily merged into a joint network to perform both tasks at the same time, sharing most of the computation. This could be interesting in application domains where object classification and segmentation have to be performed simultaneously, e.g., autonomous driving and object retrieval.

In the following of the chapter, Section 4.1 motivates the model in the context of the state of the art at the time it was conceived, Section 4.2 describe the ReSeg model in detail and Section 4.3 presents the results of the experiments.

¹ Subsequent but independent work (Yan *et al.*, 2016) further confirmed the effectiveness of ReSeg, combining a variation of it with CRFs and reporting state of the art results on Pascal VOC (Everingham *et al.*, 2015).

4.1 Motivation

In recent years, CNNs have become the *de facto* standard in many computer vision tasks, such as image classification and object detection (Krizhevsky *et al.*, 2012a; Erhan *et al.*, 2014). Top performing image classification architectures usually involve *very* deep CNN trained in a supervised fashion on large datasets (Lin *et al.*, 2014a; Simonyan and Zisserman, 2015; Szegedy *et al.*, 2014a) and have been shown to produce generic hierarchical visual representations that perform well on a wide variety of vision tasks.

Similarly, in the semantic segmentation panorama there is a tendency to convert the standard deep CNN classifier into Fully Convolutional Networks (FCN) (see e.g., (Long *et al.*, 2015b; Noh *et al.*, 2015; Badrinarayanan *et al.*, 2015a; Ronneberger *et al.*, 2015)) to obtain coarse image representations, which are subsequently upsampled to recover the lost resolution. However, these deep CNNs heavily reduce the input resolution through successive applications of pooling or subsampling layers. While these layers seem to contribute significantly to the desirable invariance properties of deep CNNs, they also make it challenging to use these pre-trained CNNs for tasks such as semantic segmentation, where a per pixel prediction is required.

The problem of recovering pixel level information from the inner layers of a CNN has been tackled in a large variety of ways. For instance, (Eigen and Fergus, 2015) proposed a multi-scale architecture that extracts coarse predictions, which are then refined using finer scales. Farabet *et al.* (2013) introduced a multi-scale CNN architecture; Hariharan *et al.* (2015a) combine the information distributed over all layers to make accurate predictions. Other methods such as (Long *et al.*, 2015b; Badrinarayanan *et al.*, 2015a) use simple bi-linear interpolation to upsample the feature maps of increasingly abstract layers and Ronneberger *et al.* (2015) concatenate the feature maps of the downsampling layers with the feature maps of the upsampling layers to help recover finer information. Finally, more sophisticated upsampling methods, such as unpooling (Noh *et al.*, 2015; Badrinarayanan *et al.*, 2015a) or deconvolution (Long *et al.*, 2015b) are now well established in the literature.

One common issue of all these methods is that they are not specifically designed to take into account and preserve both *local* and *global* contextual dependencies, which have shown to be useful for semantic segmentation tasks (Singh and Kosecka, 2013; Gatta *et al.*, 2014). Rather, these models often employ Conditional Random Fields (CRFs) as a post-processing step to locally smooth the model predictions, but how to tackle long-range contextual dependencies remains relatively unexplored.

Recurrent neural networks have been used in a variety of tasks for years and have been particularly successful in natural language processing (see, e.g., Mikolov, 2012; Sutskever *et al.*, 2014; Cho *et al.*, 2014a), handwriting recognition and generation (see, e.g., Graves and Schmidhuber, 2009; Graves *et al.*, 2008; Graves, 2013) and speech recognition (see, e.g., Chorowski *et al.*, 2014; Graves and Jaitly, 2014). Only recently RNN and RNN-like models have become popular in the semantic segmentation literature to capture long distance pixel dependencies with the goal to improve semantic segmentation (Pinheiro and Collobert, 2014; Gatta *et al.*, 2014; Chen *et al.*, 2015; Byeon *et al.*, 2015; Stollenga *et al.*, 2015).

For instance, in (Pinheiro and Collobert, 2014; Gatta *et al.*, 2014), CNN are unrolled through different time steps to include semantic feedback connections. In (Byeon *et al.*,

2015), 2-dimensional Long Short Term Memory, which consist of 4 LSTM blocks scanning all directions of an image (left-bottom, left-top, right-top, right-bottom), are introduced to learn long range spatial dependencies. Following a similar direction, in (Stollenga *et al.*, 2015), multi-dimensional LSTM are swept along different image directions; however, in this case, computations are re-arranged in a pyramidal fashion for efficiency reasons. Finally, in (Visin *et al.*, 2015), ReNet is proposed to model pixel dependencies in the context of image classification. It is worth noting that an important consequence of the adoption of the ReNet spatial sequences is that they are even more easily parallelizable, as each RNN is dependent only along a horizontal or vertical sequence of pixels; i.e., all rows/columns of pixels can be processed at the same time.

The ReSeg model, that is the subject of this chapter, aims to be an *efficient* application of recurrent Neural networks to retrieve contextual information from images. The goal of this model is to extend the ReNet architecture (Visin *et al.*, 2015), originally designed for image classification, to deal with the more ambitious task of semantic segmentation.

As explained in Chapter 3 the ReNet layers can efficiently capture contextual dependencies from images by first sweeping the image horizontally, and then sweeping vertically the feature maps produced by the horizontal processing. The output of a ReNet layer is therefore implicitly encoding the local features at each pixel position with respect to the whole input image, providing a rich feature map of local features conditioned on global information. The intuition behind the proposed ReSeg model is that this can be exploited for more fine detailed tasks than the object recognition originally proposed in ReNet, such as to address the pixel-level task of semantic segmentation.

To decrease the training time and benefit from generic local features, the ReSeg model first preprocesses the input with a FCN, i.e., the intermediate convolutional output of VGG-16 (Simonyan and Zisserman, 2015) is given as an input to the recurrent part of the network. Multiple ReNet layers then work on this generic feature map to extract meaningful local and global pixel dependencies. The resulting structured prediction architecture exploits the local generic features extracted by the CNNs and the ability of RNNs to retrieve distant dependencies to produce a rich encoding of the input. Finally, one or more transposed convolutional layer are stacked on top of the ReNet layers to upsample the intermediate feature maps back to the image size, in order to allow predictions at the pixel level.

The ReSeg architecture is efficient, flexible and suitable for a variety of pixel-level, fine grained tasks, e.g., detecting road signs, cars and pedestrians in autonomous navigation settings; detecting tumors in fMRI scans or surgical videos; guide autonomous surgical robots by detecting medical instruments in operations; detect faces and other parts of the human body for end users applications such as interactive games or camera autofocus. The ReSeg source code and model hyperparameters are available on <https://github.com/fvisin/reseg>.

4.2 Model Description

ReSeg builds on top of ReNet, described in Chapter 3 and extends it to address the task of semantic segmentation. The model pipeline involves multiple stages. First, the input image is processed with the VGG-16 (Simonyan and Zisserman, 2015) network, pre-trained on ImageNet (Deng *et al.*, 2009) without further fine-tuning. By design, only the first

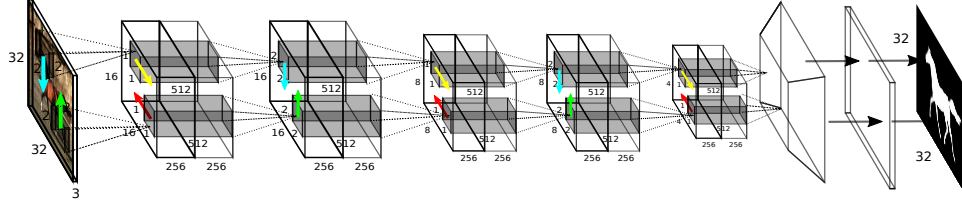


Figure 4.1: The ReSeg network. For space reasons the pretrained VGG-16 convolutional layers used to preprocess the input to ReSeg are not represented. The first 2 RNNs (blue and green) are applied on $2 \times 2 \times 3$ patches of the image. Since the patches are non-overlapping, this has the effect of halving the resolution. The resulting $16 \times 16 \times 256$ feature maps are concatenated and fed as input to the next two RNNs (red and yellow) which read $1 \times 1 \times 512$ patches and emit the output of the first ReNet layer. Two similar ReNet layers are stacked, followed by an upsampling layer and a softmax nonlinearity.

layers of VGG-16 have been used to prevent the resolution of the intermediate feature maps to become too small. The result of this preprocessing is then fed into one or more *ReNet layers* that sweep over the image horizontally and vertically. Finally, one or more *upsampling layers* are employed to resize the last feature maps to the same resolution as the input and a softmax non-linearity is applied to predict the probability distribution over the classes for each pixel. The following sections analyze in detail each component of the processing pipeline.

4.2.1 ReNet layer

As in the ReNet model, each recurrent layer is composed by 4 RNNs coupled together in such a way to capture the local and global spatial structure of the input data. Specifically, the model takes as an input an image (or the feature map of the previous layer) \mathbf{X} of elements $x \in \mathbb{R}^{H \times W \times C}$, where H , W and C are respectively the height, width and number of channels (or features) and splits it into $I \times J$ flattened non-overlapping patches $\mathbf{p}_{i,j} \in \mathbb{R}^{H_p \times W_p \times C}$. It then sweeps along each of its columns $\mathbf{p}_{i,:}$ vertically a first time with two RNNs f^\downarrow and f^\uparrow , with U recurrent units each, that move top-down and bottom-up respectively. Note that the processing of each column is independent and can be done in parallel. This is a very important performance difference of the ReSeg model with respect to other architectures in the literature that enforce to handle the data in a more constrainedly sequential nature.

At every time step each RNN reads the next non-overlapping patch $\mathbf{p}_{i,j}$ and, based on its previous state, emits a projection $\mathbf{o}_{i,j}^*$ and updates its state $\mathbf{c}_{i,j}^*$:

$$\mathbf{o}_{i,j}^\downarrow = f^\downarrow(\mathbf{c}_{i-1,j}^\downarrow, \mathbf{p}_{i,j}), \text{ for } i = 1, \dots, I, \quad (4.1)$$

$$\mathbf{o}_{i,j}^\uparrow = f^\uparrow(\mathbf{c}_{i+1,j}^\uparrow, \mathbf{p}_{i,j}), \text{ for } i = I, \dots, 1. \quad (4.2)$$

It has to be stressed that the decision to read non-overlapping patches is a modeling choice to increase the image scan speed and lower the memory usage, but is not a limitation of the architecture.

Once the first two vertical RNNs have processed the whole input \mathbf{X} in parallel, their projections $\mathbf{o}_{i,j}^\downarrow$ and $\mathbf{o}_{i,j}^\uparrow$ are concatenated to obtain a composite feature map \mathbf{O}^\ddagger whose elements $\mathbf{o}_{i,j}^\ddagger \in \mathbb{R}^{2U}$ can be seen as the activation of a feature detector at the location (i, j) with respect to all the patches in the j -th column of the input. For simplicity, in the rest of this manuscript this part of the model will be referred to as *vertical recurrent sublayer*.

After obtaining the concatenated feature map \mathbf{O}^\ddagger , the model sweeps over each of its rows with a pair of new RNNs f^\rightarrow and f^\leftarrow . Each element of \mathbf{O}^\ddagger is processed individually, rather than grouping them into patches as was done in the vertical recurrent sublayer. This was chosen so that the second recurrent sublayer has the same spatial granularity as the first one, but this is not a constraint of the model and different architectures can be explored.

With a similar procedure as the one adopted for the first sublayer, but in the horizontal direction, the network reads one element of the intermediate feature map $\mathbf{o}_{i,j}^\uparrow$ at each step and emits two activations coming from two new RNNs that are concatenated into a unique feature map $\mathbf{O}^{\leftrightarrow} = \{\mathbf{o}_{i,j}^{\leftrightarrow}\}_{i=1..I}^{j=1..J}$, with $\mathbf{o}_{i,j}^{\leftrightarrow} \in \mathbb{R}^{2U}$. Each element $\mathbf{o}_{i,j}^{\leftrightarrow}$ of this *horizontal recurrent sublayer* represents the features of one of the input image patches $\mathbf{p}_{i,j}$ with contextual information from the whole image.

It is trivial to note that it is possible to concatenate many recurrent layers $\mathbf{O}^{(1\cdots L)}$ one after the other and train them with any optimization algorithm that performs gradient descent, as the composite model is a smooth, continuous function.

The recurrent layers that are the core of this architecture, can be either implemented as vanilla tanh RNN layers, Gated Recurrent Unit (GRU) layers (Cho *et al.*, 2014a) or LSTM layers (Hochreiter and Schmidhuber, 1997). Previous work has shown that the ReNet model can perform well with little concern for the specific recurrent unit used (Visin *et al.*, 2015). The ReSeg model was tested choosing GRU units over alternative implementations, as they strike a good balance between memory usage and computational power, but nothing prevents from using different kinds of RNN layers.

4.2.2 Upsampling layer

Since by design each recurrent layer processes non-overlapping patches, the size of the last composite feature map is smaller than the size of the initial input \mathbf{X} , whenever the patch size is greater than one. To be able to compute a segmentation mask at the same resolution as the ground truth, the prediction has to be expanded back before applying the softmax non-linearity.

Several different methods can be used to this end, e.g., fully connected layers, full convolutions and transposed convolutions. The first is not a good candidate in this domain as it does not take into account the topology of the input, which is essential for this task; the second is not optimal either, as it would require large kernels and stride sizes to upsample by the required factor. Transposed convolutions are both memory and computation efficient, and are the ideal method to tackle this problem.

Transposed convolutions (introduced in Section 2.2.7) – also known as *fractionally strided convolutions* – have been employed in many works in recent literature (Zeiler *et al.*, 2011a; Zeiler and Fergus, 2014b; Long *et al.*, 2015a; Radford *et al.*, 2015; Im *et al.*, 2016). This method is based on the observation that direct convolutions can be expressed as a dot product between the flattened input and a sparse matrix, whose non-zero elements are

elements of the convolutional kernel. The equivalence with the convolution is granted by the connectivity pattern defined by the matrix.

Transposed convolutions apply the transpose of this transformation matrix to the input, resulting in an operation whose input and output shapes are inverted with respect to the original direct convolution. A very efficient implementation of this operation can be obtained exploiting the gradient operation of the convolution – whose optimized implementation can be found in many of the most popular libraries for neural networks. For an in-depth and comprehensive analysis of each alternative, see Section 2.2.7.

4.3 Experiments

4.3.1 Datasets

The ReSeg architecture has been evaluated on several benchmark datasets. The model has been first tested on the easier case of background/foreground segmentation, where the algorithm is only requested to distinguish between the main subject in the scene and the rest of the image. These preliminary experiments were conducted on the Weizmann Horse and the Oxford Flowers datasets, to then focus on the full task of semantic segmentation on the more challenging Camvid dataset. The rest of this section proceeds as follows: each dataset is briefly introduced, the settings of each experiment are then outlined and finally the results are presented and discussed.

Weizmann Horse

The Weizmann Horse dataset, introduced in (Borenstein, 2004)², is an image segmentation dataset consisting of 329 variable size images in both RGB and gray scale format, matched with an equal number of groundtruth segmentation images, of the same size as the corresponding image. The groundtruth segmentations contain a foreground/background mask of the focused horse, encoded as a real-value between 0 and 255. To convert this into a boolean mask, the data has been thresholded in the center of the range setting all smaller values to 0, and all greater values to 1. See Figure 4.2 for some segmentation samples.

Oxford Flowers 17

The Oxford Flowers 17 class dataset from (Nilsback and Zisserman, 2006)³ contains 1363 variable size RGB images, with 848 image segmentations maps associated with a subset of the RGB images. There are 8 unique segmentation classes defined over all maps, including flower, sky, and grass. To build a foreground/background mask, the original segmentation maps have been merged together setting any pixel not marked as class 38 (the flower class) to 0, and setting all the flower class pixels to 1. This binary segmentation task for Oxford Flowers 17 is described in detail in (Wu and Kashino, 2014). See Figure 4.3 for some segmentation samples.

²<http://www.msri.org/people/members/eranb/>

³<http://www.robots.ox.ac.uk/~vgg/data/flowers/>

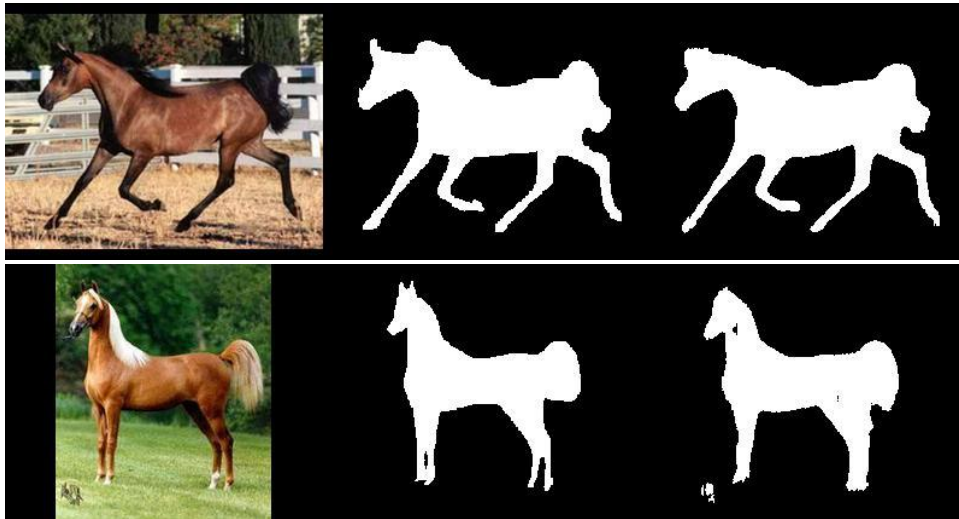


Figure 4.2: *ReSeg Weizmann Horse segmentation samples. Left: Input image, Center: Ground truth segmentation, Right: ReSeg predicted segmentation.*

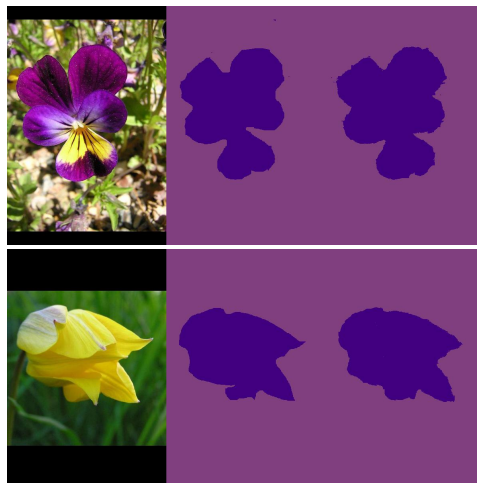


Figure 4.3: *ReSeg Oxford Flowers segmentation samples. Left: Input image, Center: Ground truth segmentation, Right: ReSeg predicted segmentation.*

CamVid Dataset

The Cambridge-driving Labeled Video Database (CamVid) (Brostow *et al.*, 2009)⁴ is a real-world dataset which consists of images recorded from a car with an internally mounted camera, capturing frames of 960×720 RGB pixels per frame, with a recording frame rate of 30 frames per second. A total of ten minutes of video was recorded, and approximately

⁴<http://mi.eng.cam.ac.uk/research/projects/VideoRec/CamVid/>

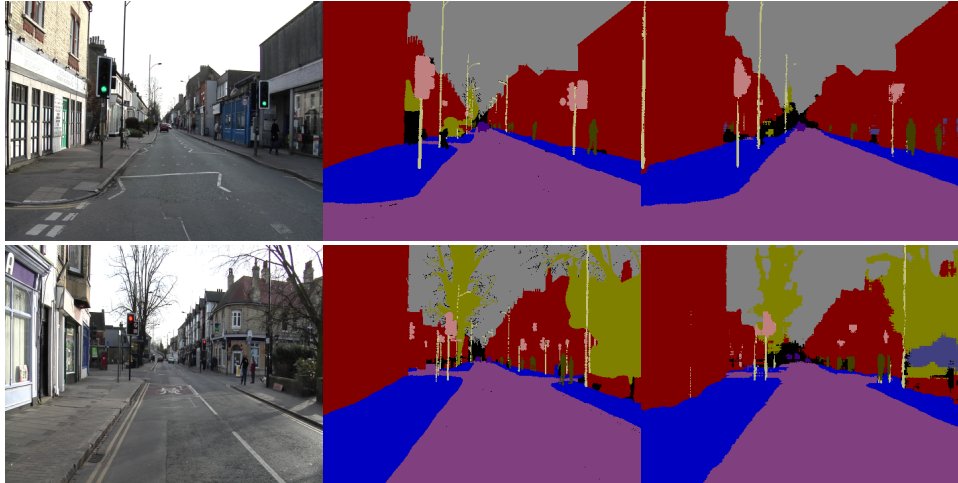


Figure 4.4: *ReSeg CamVid segmentation samples. Left: Input image, Center: Ground truth segmentation, Right: ReSeg predicted segmentation.*

one frame per second has been manually annotated with per pixel class labels, from one of 32 possible classes. A small number of pixels were labeled as void in the original dataset. These do not belong to any of the 32 classes prescribed in the original data, and are ignored during evaluation. The CamVid dataset is split into 367 training, 101 validation and 233 test images for a total of 701 images with corresponding annotations. The results presented in this section were obtained on a preprocessed version of the dataset that downsampled the images to a resolution of 480×360 and used a subset of the original labels that comprises 11 class categories. This experimental setup was chosen to be able to compare the results of the model to those reported in (Badrinarayanan *et al.*, 2015a). See Figure 4.4 for some segmentation samples.

4.3.2 Data augmentation and preprocessing

The ReNet model adopted some data augmentation methods to enlarge the dataset by adding synthetic data obtained by randomly flipping and shifting the images. In ReSeg instead, this kind of data augmentation were not employed.

The only data augmentation technique exploited was to randomly change the colors by inverting the intensity values of the whole image with probability 0.5. This kind of data augmentation technique is only meaningful when working with gray-scale images and was employed for the Weizmann Horse dataset only to improve the segmentation performance on light colored horses. In that dataset in fact the light-colored horses are much less represented than the dark ones and the network did not perform very well on the former without data augmentation. Its introduction allowed to significantly improve the performance on the Weizmann Horse dataset, probably because the misclassification of the few light-colored horses impacted severely on the total score due to the very limited number of images of the dataset. The same technique would probably not be as effective on bigger and more balanced datasets.

In the *training* phase, all the images have been resized to the average resolution of the training set, by computing the mean width and height over the training set in case of images with variable size. To keep the aspect ratio of the images unmodified, each image has been first resized to match the shortest dimension and then center-padded with zeros on the remaining axis to reach the desired resolution. It should be noted that all transformations that involve changes in dimensionality or position must also be applied in the same form to the segmentation mask, and great care must be taken (especially during resizing/shifting) not to introduce unexpected errors. It is particularly important to resize the network prediction to the original size of the ground truth and not the opposite, not to misrepresent the segmentation accuracy. This is not a problem for validation and test, as the images are not resized in those cases.

This resizing strategy was adopted for the Weizmann Horse and Oxford Flowers dataset, while in the Camvid dataset case no resize was needed, apart from the one reported in Section 4.3.1. This strategy allowed to train on batches of multiple images, with the effect of speeding up the training fully exploiting the parallel computation allowed by GPU-computing. The performance loss due to the difference in training and validation/test size was negligible, probably thanks to the adoption of the pretrained VGG-16 layers that can extract meaningful features from the typical size of the images in the adopted datasets. On the contrary, training benefitted a little from resizing the images on some of the datasets, probably because eliminating unnecessary and easily explained variance can help the model focus on harder characteristics, which generally leads to better performance on the task at hand.

4.3.3 Experimental settings

To gain confidence with the sensitivity of the model to the different hyperparameters, Re-Seg was first evaluated on the Weissman Horse and Oxford Flowers datasets on a binary foreground/background segmentation task. Once a good initial setting of the hyperparameters was found, most of the efforts were spent on the more challenging semantic segmentation task on the CamVid dataset.

The number of hyperparameters of this model is potentially very high, as for each ReNet layer different implementations are possible (namely vanilla RNN, GRU or LSTM), each one with its specific parameters. Furthermore, the number of features, the size of the patches and the initialization scheme have to be defined for each ReNet layer as well as for each transposed convolutional layer. To make it feasible to explore the hyperparameter space, some of the hyperparameters have been fixed by design and the remaining have been finetuned. In the rest of this section, the architectural choices for both sets of parameters will be detailed.

Initial experiments on upsampling showed that transposed convolutional layers seem to provide a better performance with respect to less sophisticated (not learned) tiling strategies such as nearest neighbor tiling or bilinear interpolation when there is enough data to learn the transformation. All the transposed convolution upsampling layers were followed by a ReLU (Krizhevsky *et al.*, 2012c) non-linearity and initialized with the fan-in plus fan-out initialization scheme described in (Glorot and Bengio, 2010). The recurrent weight matrices were instead initialized to be orthonormal, following the procedure defined in (Saxe *et al.*, 2014). Finally, the stride of the upsampling transposed convolutional layers was constrained to be tied to their filter size.

One specificity of the segmentation task is that each training image carries classification information for all of its pixels. Differently from the image classification task, small batch sizes already provide the model with a large amount of information with sufficient variance to learn and generalize well. The ReSeg model was tested with various values of batch size, going as low as processing a single image at a time, obtaining comparable results in terms of performance. Many experiments were performed using a minibatch size of 1. When computational resources allowed, larger batch sizes were used, e.g., 5, 10, 20, 35, and 50. Larger batch sizes smoothed learning (as expected), and removed some issues related to spurious occurrences in the datasets such as misaligned or poorly segmented groundtruth masks. This had a bigger impact on the smaller datasets than on Camvid, where the batch size was kept fixed to the value of 5, as a compromise between training speed and memory usage.

All the experiments, used L2 regularization (Krogh and Hertz, 1992) with a weight decay factor of 0.001 to avoid instability at the end of training. Also, all the models were trained with the Adam (Kingma and Ba, 2014a) optimization algorithm, that does not require a specific hyperparameter tuning. The effect of batch normalization in RNNs has been a focus of attention (Laurent *et al.*, 2015), but it does not seem yet to provide a reliable improvement in performance, so it was not adopted.

The adaptive learning rate algorithm known as Adam (Kingma and Ba, 2014b) was a key ingredient to stable learning, though others such as Adadelta (Zeiler, 2012) were useful during model development. In addition, gradient norm rescaling was also utilized to help with the problems described in (Bengio *et al.*, 2013). Regularization proved to be another important part of the process on the smaller Weizmann Horse and Oxford flowers datasets. For those two, weight noise, as described in (Graves, 2011), with a scale of 0.075 was applied to all weight matrices before each forward pass in all the experiments. Dropout (Srivastava *et al.*, 2014) on each forward connection with drop probability of 0.2 on the input, and/or with drop probability of 0.5 on the hidden projections was applied too.

The experiments mainly focused on varying the number of ReNet layers and the number of upsampling transposed convolutional layers, as well as tuning their respective parameters, such as the number of features $d_{\text{RE}}(l)$ and $d_{\text{UP}}(l)$ respectively, and the size of the input patches (or equivalently of the filters) $ps_{\text{RE}}(l)$ and $fs_{\text{UP}}(l)$. The best parameters are reported in Table 4.2.

4.3.4 Results

The metrics reported on all the datasets are the per-pixel accuracy (*Global acc*), computed as the percentage of true positives with respect to the total number of pixels in the image, as well as the average per-class Intersection over Union (*Avg IoU*), computed on each class as true positive divided by the sum of true positives, false positives and false negatives and then averaged. In the full semantic segmentation setting the per-class accuracy and the average per-class accuracy (*Avg class acc*) are also reported.

Table 4.3 reports the results on the Weizmann Horse dataset. On this dataset, the assumption that processing the input image with some pre-trained convolutional layers from VGG-16 could ease the learning was verified. Specifically, the experiments were restricted to only using the first 7 convolutional layers from VGG, as the goal was to extract some low-level generic features only and learn the task-specific high-level features with the ReNet layers. The results indeed show an increase in terms of average Intersection

4.3. Experiments

Method	Building	Tree	Sky	Car	Sign-Symbol	Road	Pedestrian	Fence	Column-Pole	Side-walk	Bicyclist	Avg class acc	Global acc	Avg IoU
<i>Segmentation models</i>														
Super Parsing (Tighe and Lazebnik, 2013)	87.0	67.1	96.9	62.7	30.1	95.9	14.7	17.9	1.7	70.0	19.4	51.2	83.3	n/a
Boosting+Higher order (Sturgess <i>et al.</i> , 2009)	84.5	72.6	97.5	72.7	34.1	95.3	34.2	45.7	8.1	77.6	28.5	59.2	83.8	n/a
Boosting+Detectors+CRF (Ladicky <i>et al.</i> , 2010)	81.5	76.6	96.2	78.7	40.2	93.9	43.0	47.6	14.3	81.5	33.9	62.5	83.8	n/a
<i>Neural Network based segmentation models</i>														
SegNet-Basic (layer-wise training (Badrinarayanan <i>et al.</i> , 2015b))	75.0	84.6	91.2	82.7	36.9	93.3	55.0	37.5	44.8	74.1	16.0	62.9	84.3	n/a
SegNet-Basic (Badrinarayanan <i>et al.</i> , 2015a)	80.6	72.0	93.0	78.5	21.0	94.0	62.5	31.4	36.6	74.0	42.5	62.3	82.8	46.3
SegNet (Badrinarayanan <i>et al.</i> , 2015a)	88.0	87.3	92.3	80.0	29.5	97.6	57.2	49.4	27.8	84.8	30.7	65.9	88.6	50.2
ReSeg + Class Balance	70.6	84.6	89.6	81.1	61.0	95.1	80.4	35.6	60.6	86.3	60.0	73.2	83.5	53.7
ReSeg	86.8	84.7	93.0	87.3	48.6	98.0	63.3	20.9	35.6	87.3	43.5	68.1	88.7	58.8
<i>Sub-model averaging</i>														
Bayesian SegNet-Basic (Kendall <i>et al.</i> , 2015)	75.1	68.8	91.4	77.7	52.0	92.5	71.5	44.9	52.9	79.1	69.6	70.5	81.6	55.8
Bayesian SegNet (Kendall <i>et al.</i> , 2015)	80.4	85.5	90.1	86.4	67.9	93.8	73.8	64.5	50.8	91.7	54.6	76.3	86.9	63.1

Table 4.1: CamVid. The table reports the per-class accuracy, the average per-class accuracy, the global accuracy and the average intersection over union (higher is better). The best values and the values within 1 point from the best are highlighted in bold for each column. For completeness the Bayesian Segnet models are reported even if they are not directly comparable to the others as they perform a form of model averaging.

Model	p_{SE}	d_{RE}	f_{SE}	d_{UP}	Building	Tree	Sky	Car	Sign-Symbol	Road	Pedestrian	Fence	Column-Pole	Side-walk	Bicyclist	Avg class acc	Global acc	Avg IoU
ReSeg + LCN	(2 × 2), (1 × 1)	(100, 100)	(2 × 2)	(50, 50)	81.5	80.3	94.7	78.1	42.8	97.4	53.5	34.3	36.8	68.9	47.9	65.1	84.8	52.6
ReSeg + Class Balance	(2 × 2), (1 × 1)	(100, 100)	(2 × 2)	(50, 50)	70.6	84.6	89.6	81.1	61.0	80.4	35.6	60.6	86.3	60.0	73.2	83.5	53.7	
ReSeg	(2 × 2), (1 × 1)	(100, 100)	(2 × 2)	(50, 50)	86.8	84.7	93.0	87.3	48.6	98.0	63.3	20.9	35.6	87.3	43.5	68.1	88.7	58.8

Table 4.2: Comparison of the performance of different hyperparameter on CamVid.

over Union (IoU) when these layers are being used, confirming that the ReNet layers can learn good high-level features from generic convolutional features detected by a pretrained VGG model.

Another variant of the network that was tested on the Weizmann Horse dataset used intermediate predictions to help the gradient flow in the early layers of the network as depicted in Figure 4.5. In this scenario, the feature maps of some of the intermediate layers were passed to an upsampling layer followed by a softmax and the corresponding classification error was backpropagated to improve the learning of the early layers. The experiments with this setup were not conclusive, as in some cases the intermediate layers helped the training while in others they did not seem to help or were even harmful. Overall, the potential performance improvement was not significant enough in the positive cases to justify the increase of complexity and of training time, so it was decided not to employ them in the following experiments. Recent techniques, such as the use of residual connections (He *et al.*, 2015; Srivastava *et al.*, 2015c) are most probably more effective at speeding up the training of early layers of the network.

Table 4.4 shows the results for Oxford Flowers dataset, when using the full ReSeg architecture (i.e., including VGG convolutional layers). As shown in the table, this method clearly outperforms the state-of-the-art both in terms of global accuracy and average IoU.

Finally, Table 4.1 presents the results on CamVid dataset using the full ReSeg architecture. This model exhibits state-of-the-art performance in terms of IoU when compared to both standard segmentation methods and neural network based methods, showing an increase of 17% with respect to the recent SegNet model. It is worth highlighting that

Method	Global	Avg IoU
All foreground baseline	25.4	79.9
All background baseline	74.7	0.0
Kernelized structural SVM (Bertelli <i>et al.</i> , 2011)	94.6	80.1
ReSeg (no VGG)	94.9	79.9
CRF learning (Liu <i>et al.</i> , 2015a)	95.7	84.0
PatchCut (Yang <i>et al.</i> , 2015)	95.8	84.0
ReSeg	96.8	91.6

Table 4.3: Weizmann Horses. Per pixel accuracy and average IoU are reported (higher is better).

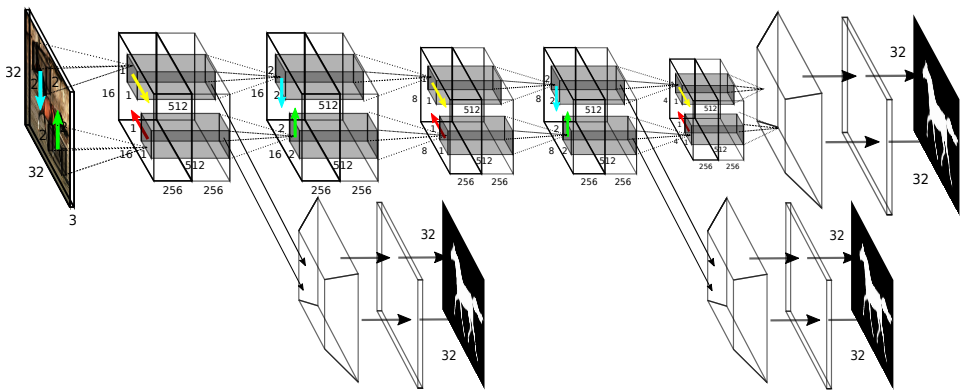


Figure 4.5: A ReSeg network with intermediate predictions.

incorporating sub-model averaging to SegNet model, as in (Kendall *et al.*, 2015), boosts the original model performance, as expected. Therefore, introducing sub-model averaging to ReSeg could also presumably result in significant performance increase. However, this remains to be tested.

4.4 Discussion

As pointed out earlier, the experiments on the Weizmann Horse dataset were treated as a test playground to acquire knowledge on the sensitivity of the model with respect to the preprocessing and the hyperparameters. The preliminary experiments show that processing the input images with the first layers of the VGG-16 pre-trained network improves the results. Other image manipulation techniques, such as pre-processing the input with Local Contrast Normalization (LCN), do not seem to improve the performance of the model (see Table 4.2) and were therefore not used in the following experiments.

While the Weizmann Horse and the Oxford Flowers datasets were tackled in a binary background/foreground segmentation setting, on the CamVid dataset the full semantic segmentation task was addressed. In this setting, when the dataset is highly imbalanced, the segmentation performance of some classes can drop significantly as the network tries to maximize the score on the high-occurring classes, *de facto* ignoring the least occurring

Method	Global	Avg IoU
All background baseline	71.0	0.0
All foreground baseline	29.0	29.2
GrabCut (Rother <i>et al.</i> , 2004)	95.9	89.3
Tri-map (Wu and Kashino, 2014)	96.7	91.7
ReSeg	98	93.7

Table 4.4: Oxford Flowers. Per pixel accuracy and average IoU are reported (higher is better).

ones. To overcome this behaviour, a class-balancing term was added to the cross-entropy loss to bias the prediction towards the less represented classes. Specifically, *median frequency balancing* (Eigen and Fergus, 2015) was employed, which re-weights the class predictions by the ratio between the median of the frequencies of the classes (computed on the training set) and the frequency of each class:

$$\alpha(c) = \text{median_frequency}/f(c), \quad (4.3)$$

where $f(c)$, the frequency of the class c , is computed dividing the number of pixels of the class c by the total number of pixels in the images where c is present, and *median_frequency* is the median of the frequencies of all the classes. The final cross-entropy loss for one image, rescaled by the rebalancing term is then

$$\text{cost} = -\frac{1}{N} \sum_{i=0}^N \sum_{c=0}^C P(p_i = c) \cdot \log Q(p_i = c) \cdot \alpha(c), \quad (4.4)$$

with N the number of pixels in the image, C the number of classes of the dataset, $P(p_i = c)$ the ground-truth probability of the i -th pixel belonging to the class c and $Q(p_i = c)$ its probability as estimated by the model. Note that since the ground truth probability of the wrong classes is usually 0, the cross-entropy is equivalent to the negative log likelihood of the correct class under the model’s distribution.

Consider the classes ordered by frequency. This rebalancing term assigns a unitary weight to the central class (i.e., it does not modify its predicted probability) lower than 1 to the first half and a weight higher than 1 to the second half. The final effect of class balancing is to increase the score of the low frequency classes (see Table 4.2) at the price of a more noisy segmentation mask, as the probability of the underrepresented classes is overestimated and can lead to an increase in misclassified pixels in the output segmentation mask. This behavior is clearly visible in Figure 4.6.

Notably, it is sufficient to process the input images with just a few layers of VGG-16 for the ReSeg model to gracefully handle the semantic segmentation task, confirming its ability to encode contextual information and long term dependencies. The dimensionality reduction that derives from halving the resolution at each encoding layer to expand it back in the upsampling layers can be expected to cause some loss of spacial precision, especially on fine-grained details. It is conceivable to imagine that the model could gain from the introduction of skip connections, a fairly recent technique that consists in providing higher resolution information from the lower layers to the upsampling ones. This is described

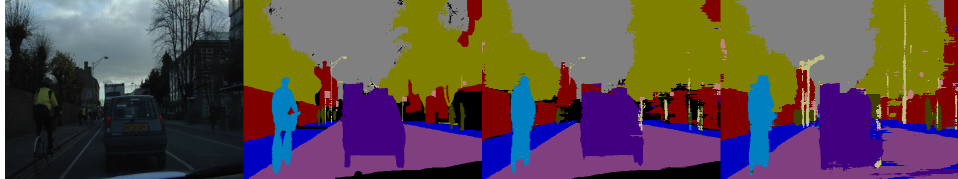


Figure 4.6: Camvid segmentation example with and without class balancing. From the left: input image, ground truth segmentation, ReSeg segmentation, ReSeg segmentation with class balancing. Class balancing improves the low frequency classes, e.g., the street poles, at the price of a worse overall segmentation.

in Section 5.2.4 and adopted in the model that will be the main subject of the following chapter.

The experiments proved the flexibility of ReSeg in the foreground-background segmentation as well as the full semantic segmentation tasks on multiple datasets. The model achieves state of the art on all the datasets it was tested on and generates convincing segmentation masks, as shown in Figures 4.2, 4.3, 4.4 and 4.6.

CHAPTER 5

Convolutional RNNs for Video Semantic Segmentation

The previous chapter introduced the task of semantic segmentation, where the model is requested to produce a semantic mask, i.e., to classify every pixel of an input image. Rather than presenting the algorithm with a single image, a variant of the segmentation task, called cosegmentation, provides it with multiple images usually taken at different locations in the same scene (potentially by different cameras). In this setting the model can exploit the information that the images potentially share to improve the single image prediction and consequently improve the global score at the same time.

In many ways, *video segmentation* can be seen as an extreme version of cosegmentation, where the model is asked to segment multiple frames of a video. As opposed to cosegmentation, where the images depict the same scene from different angles and in moments potentially very far away in time, in videos images come in a seamless fashion and their correlation through time can be exploited to increase the performance.

The main problem of this task is that, if labeling images for semantic segmentation is expensive, the time required to label all the frames of a video is even more dramatic. One typical way to alleviate this issue is to label only a subset of the frames, either by dropping most of the frames and providing only a few of them with their corresponding mask, or by providing all the input frames with only a subset of them annotated. Another way to reduce the labeling effort is to just label the main subject of each frame or to reduce the number of classes (to the limit case of foreground/background separation).

Applying machine learning techniques to this class of problems is challenging due to

the lack of large amounts of labeled data, as well as the huge amount of time required to train these kind of models; this calls for non-trivial technological solutions. For instance, the time spent on operations that are not strictly related to training, such as loading and preprocessing the data, saving the weights on disk, saving samples and generating plots to monitor the progress of the algorithm, has to be minimized. Furthermore, a recent trend in this field is to resort to multi-GPU training; this introduces an almost linear speedup (up to a certain numbers of GPUs) (Theano Development Team, 2016; Ma *et al.*, 2016), but increases the complexity of the algorithm, is often subject to constraints (e.g., the GPUs might have to be hosted by the same machine or node of a cluster), and makes debugging much less cumbersome in many cases.

Chapter 4 introduced ReSeg (Visin *et al.*, 2016), an RNN-based model for image semantic segmentation. One of the main strengths of ReSeg comes from the coupling of fast general-purpose CNN feature extractors with stateful RNNs able to carry the information extracted by the CNNs through various steps of computation, showing the effectiveness of RNNs applied to the spatial domain. This approach can be taken a step further, allowing the RNNs to jointly process space and time information in videos by placing the CNNs directly into the inner computation of the recursive layer. This chapter introduces a novel architecture that aims to overcome the task separation traditionally enforced by the CNN-RNN dichotomy. This is achieved by processing the temporal and the spatial information jointly, mixing the two architectures at each layer of the recurrent-convolutional hierarchy.

5.1 Motivation

In the last few years, convolutional neural networks have been successfully applied to address many computer vision tasks, such as image classification (Krizhevsky *et al.*, 2012c; Simonyan and Zisserman, 2015; Szegedy *et al.*, 2014b) and object detection (Girshick *et al.*, 2013; Sermanet *et al.*, 2013a) and their application has become ubiquitous in many widely used commercial products, such as face and smile detectors in digital cameras, people recognition in social networks and street signals recognition in cars.

Recently, pixel-wise prediction of still images has enjoyed the attention of the computer vision community. In contrast to image classification and object detection this *structured prediction* problem requires each pixel to be classified, which demands for a more detailed understanding of the image, as well as consistency in the prediction. In this domain, many state of the art architectures successfully coupled classification models trained on ImageNet (Simonyan and Zisserman, 2014b; Szegedy *et al.*, 2015) with various upsampling strategies, to address the challenging image segmentation and scene parsing task (see e.g., Long *et al.*, 2015b; Noh *et al.*, 2015) in a trainable end-to-end fashion.

The success witnessed on still images has rapidly reached the video domain, achieving remarkable results in tasks such as video action recognition (Simonyan and Zisserman, 2014a; Karpathy *et al.*, 2014), event detection in videos (Yeung *et al.*, 2015) and video captioning (Yao *et al.*, 2015a). Along this direction, some effort has been devoted lately to address the more challenging task of end to end video semantic segmentation (Tran *et al.*, 2015).

While many computer vision video-related tasks involve predicting only a single or a few output per video, some of them – such as video semantic segmentation, change detection, and object tracking – require a *per temporal "voxel"* prediction. As an analogy

to 3D voxels, where a volumetric pixel (or voxel) is used to describe a local portion of the data that extends across space in three dimensions, temporal voxels refer to 3D portions of the data that span over a contiguous two-dimensional space and over a one-dimensional sequence in the temporal domain. Works in this direction usually define a fixed *a priori* window on the temporal dimension to obtain a voxel-wise prediction (Tran *et al.*, 2015).

The most common way to address video related tasks with neural network approaches is to combine CNNs with RNNs in a sequential fashion, by first applying a (possibly pre-trained) CNN on each frame and then interpreting the resulting feature maps in a temporal consistent way by processing them with an RNN (Donahue *et al.*, 2014; Vinyals *et al.*, 2015; Karpathy and Li, 2015; Venugopalan *et al.*, 2015). While this is an effective way to exploit the temporal information, the two pipelines do not completely benefit from each other, since the temporal consistency is enforced only in the last step. Furthermore, the spatial relations are mostly ignored by the state of the RNN as they are taken into account only through the encoding coming from the CNNs.

On this note, Shi *et al.* (2015) propose an interesting approach that deeply entangles the convolution operator with the state-to-state and input-to-state transitions of the RNN itself, rather than encoding each frame independently with CNNs and then processing the spatial encodings timewise with an RNN. The model presented in this chapter, called Decoder Encoder Convolutional LSTM (DEConvLSTM), builds on top of Shi *et al.* (2015) and extends their work in two ways: i) replacing the convolution operator in input-to-state transitions with a full multi-layer convolutional subnetwork ii) introducing a novel recurrent-convolutional-upsampling layer that learns how to leverage the spatio-temporal dimensions jointly to produce an upsampled feature map that respects the 2D topology of the input feature map and at the same time maintains its time consistency. The full model mimics the conventional 2D semantic segmentation encoder-decoder architecture, but is able to jointly capture spatio-temporal information, using the internal memory of RNNs instead of a fixed window over time.

5.2 Model description

Videos can be interpreted as a set of frames that interlace spatial information through time. The supporting idea of the proposed DEConvLSTM model builds on this, with the claim that space and time cannot be processed sequentially – as done by much of the past ML literature – but rather the two should be mixed together in a coherent and joint architecture. The DEConvLSTM intertwines space with time at each step of the hierarchy (see Figure 5.1), taking inspiration from the convolutional LSTM (ConvLSTM) model described by (Shi *et al.*, 2015). As many successful models for semantic segmentation on static images, the DEConvLSTM couples an encoding and a decoding pathway, that respectively shrink the resolution of the intermediate feature maps, encoding a rich representation of the input, and upsample it to recover the resolution of the input video.

This section will introduce the novelties of the DEConvLSTM model, starting with a description of the encoding pathway that builds on the ConvLSTM model and then building on that to uncover the novelties of the proposed model.

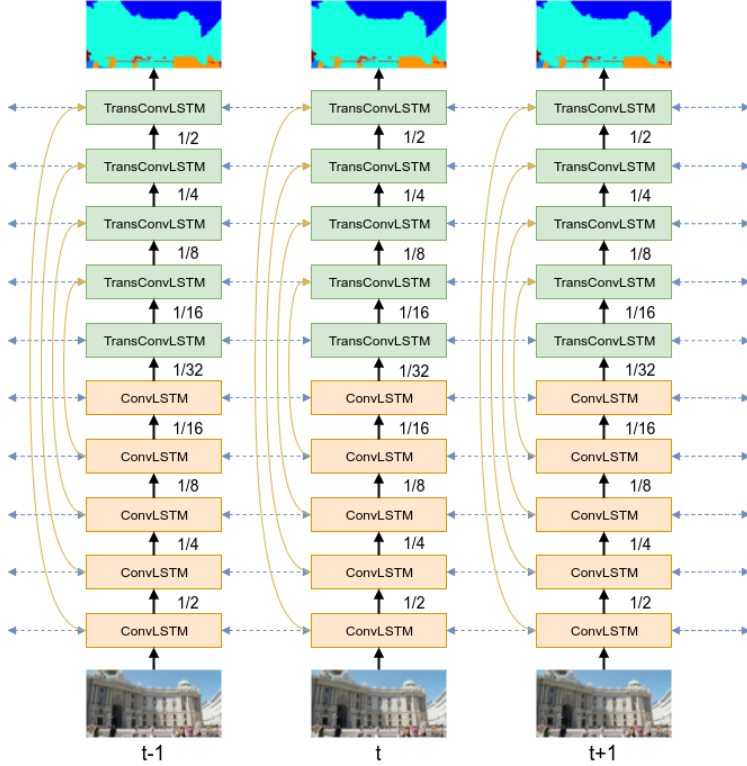


Figure 5.1: The DEConvLSTM architecture. The input (bottom) to the model is a sequence of video frames and the output (top) is a sequence of segmentation maps. The rectangles represent ConvLSTM and TransConvLSTM layers. The inner convolutions of these layers are not represented for space reasons. The black solid arrows represent connections between layers in the hierarchy, the dashed arrows represent the recursive connections in the time domain. Finally the yellow arrows are the skip connections.

5.2.1 Convolutional LSTM

In (Shi *et al.*, 2015) the authors propose the ConvLSTM model that is a modification of the well-known LSTM with peephole connections. To allow for a more convenient comparison, the equations of the vanilla LSTM with peephole connections (that were defined in Equation 2.25) are reported here

$$\begin{aligned}
 i_t &= \sigma (\mathbf{W}_{ih} \cdot \mathbf{h}_{t-1} + \mathbf{W}_{ix} \cdot \mathbf{x}_t + \mathbf{W}_{ic} \odot \mathbf{c}_{t-1} + \mathbf{b}_i), \\
 f_t &= \sigma (\mathbf{W}_{fh} \cdot \mathbf{h}_{t-1} + \mathbf{W}_{fx} \cdot \mathbf{x}_t + \mathbf{W}_{fc} \odot \mathbf{c}_{t-1} + \mathbf{b}_f), \\
 \tilde{\mathbf{c}}_t &= \tanh (\mathbf{W}_{ch} \cdot \mathbf{h}_{t-1} + \mathbf{W}_{cx} \cdot \mathbf{x}_t + \mathbf{b}_c), \\
 \mathbf{c}_t &= \mathbf{f}_t \odot \mathbf{c}_{t-1} + \mathbf{i}_t \odot \tilde{\mathbf{c}}_t, \\
 \mathbf{o}_t &= \sigma (\mathbf{W}_{oh} \cdot \mathbf{h}_{t-1} + \mathbf{W}_{ox} \cdot \mathbf{x}_t + \mathbf{W}_{oc} \odot \mathbf{c}_{t-1} + \mathbf{b}_o), \\
 \mathbf{h}_t &= \mathbf{o}_t \odot \tanh (\mathbf{c}_t),
 \end{aligned} \tag{2.25 revisited}$$

where \mathbf{x}_t and \mathbf{h}_t are the input and output feature maps respectively at time t ; \mathbf{c}_t is the state of the cell (or memory) of the recurrent unit at time t ; \mathbf{i}_t , \mathbf{f}_t , \mathbf{o}_t are respectively the states of the input gate, the forget gate, and the output gate, i.e., the gates that control the behavior of the recurrent unit given the input and its state at each time step t . σ is the logistic function, \mathbf{W}_\star^1 , the weights and \odot the Hadamard product.

The convolutional LSTM of (Shi *et al.*, 2015) replaces the dot products with convolutions, leading to the following formulation

$$\begin{aligned}\mathbf{i}_t &= \sigma(\mathbf{W}_{ih} * \mathbf{h}_{t-1} + \mathbf{W}_{ix} * \mathbf{x}_t + \mathbf{W}_{ic} \odot \mathbf{c}_{t-1} + \mathbf{b}_i), \\ \mathbf{f}_t &= \sigma(\mathbf{W}_{fh} * \mathbf{h}_{t-1} + \mathbf{W}_{fx} * \mathbf{x}_t + \mathbf{W}_{fc} \odot \mathbf{c}_{t-1} + \mathbf{b}_f), \\ \tilde{\mathbf{c}}_t &= \tanh(\mathbf{W}_{ch} * \mathbf{h}_{t-1} + \mathbf{W}_{cx} * \mathbf{x}_t + \mathbf{b}_c), \\ \mathbf{c}_t &= \mathbf{f}_t \odot \mathbf{c}_{t-1} + \mathbf{i}_t \odot \tilde{\mathbf{c}}_t, \\ \mathbf{o}_t &= \sigma(\mathbf{W}_{oh} * \mathbf{h}_{t-1} + \mathbf{W}_{ox} * \mathbf{x}_t + \mathbf{W}_{oc} \odot \mathbf{c}_{t-1} + \mathbf{b}_o), \\ \mathbf{h}_t &= \mathbf{o}_t \odot \tanh(\mathbf{c}_t),\end{aligned}\tag{5.1}$$

where $*$ is the convolution operator. Notably, as opposed to classical recurrent architectures, all gates and states here have *spatial dimensions* as they are the result of the application of convolutions on the input of the layer.

The encoding pathway of our DeconvLSTM model builds on this, with two modifications: i) it introduces a full, multi-layered, CNN, in place of the convolution operator; ii) it replaces the Hadamard product with a convolution. This is expressed in Equation 5.2

$$\begin{aligned}\mathbf{i}_t &= \sigma\left(\mathbf{W}_{ix}^{(L)} * \dots * \rho \mathbf{W}_{ix}^{(1)} * \rho \mathbf{W}_{ix}^{(0)} * \mathbf{x}_t + \mathbf{W}_{ih} * \mathbf{h}_{t-1} + \mathbf{W}_{ic} * \mathbf{c}_{t-1} + \mathbf{b}_i\right), \\ \mathbf{f}_t &= \sigma\left(\mathbf{W}_{fx}^{(L)} * \dots * \rho \mathbf{W}_{fx}^{(1)} * \rho \mathbf{W}_{fx}^{(0)} * \mathbf{x}_t + \mathbf{W}_{fh} * \mathbf{h}_{t-1} + \mathbf{W}_{fc} * \mathbf{c}_{t-1} + \mathbf{b}_f\right), \\ \tilde{\mathbf{c}}_t &= \tanh\left(\mathbf{W}_{cx}^{(L)} * \dots * \rho \mathbf{W}_{cx}^{(1)} * \rho \mathbf{W}_{cx}^{(0)} * \mathbf{x}_t + \mathbf{W}_{ch} * \mathbf{h}_{t-1} + \mathbf{b}_c\right), \\ \mathbf{c}_t &= \mathbf{f}_t \odot \mathbf{c}_{t-1} + \mathbf{i}_t \odot \tilde{\mathbf{c}}_t, \\ \mathbf{o}_t &= \sigma\left(\mathbf{W}_{ox}^{(L)} * \dots * \rho \mathbf{W}_{ox}^{(1)} * \rho \mathbf{W}_{ox}^{(0)} * \mathbf{x}_t + \mathbf{W}_{oh} * \mathbf{h}_{t-1} + \mathbf{W}_{oc} * \mathbf{c}_{t-1} + \mathbf{b}_o\right), \\ \mathbf{h}_t &= \mathbf{o}_t \odot \tanh(\mathbf{c}_t).\end{aligned}\tag{5.2}$$

A *ReLU* nonlinearity ρ follows every convolution on the input $\mathbf{W}_{\star x}^{(l \in 1, \dots, L)}$ apart from the last ones $\mathbf{W}_{\star x}^{(L)}$, since the usual σ nonlinearity is already applied to the output of the layer to keep the typical LSTM behavior intact. The last convolutions $\mathbf{W}_\star^{(L)}$ are also followed by a pooling layer (not expressed in the equations) to reduce the dimensionality of the intermediate feature maps before the nonlinearity is applied.

The substitution of the Hadamard products with convolutions reduces the number of parameters and is consistent with the idea of retaining the spatial structure in the internal state and gates of the LSTM. It also allows the network to process videos with a different resolution than the one it was trained on, which is often a convenient property.

¹ The \star notation here is used as a placeholder to represent any letter or string. In this particular case it takes the place of i, f, c and o .

5.2.2 Transposed Convolutional LSTM

It has become common to address the problem of segmenting still images with architectures that first shrink the resolution of the feature maps to produce a lower-dimensionality yet rich encoding, and then upsample the intermediate feature maps back to the original image size in order to emit a per-pixel prediction (see Chapter 4). This kind of structure has proven to be very effective to segment 2D images.

Transferring this knowledge to the video segmentation task, the DEConvLSTM model introduces a novel Transposed Convolutional LSTM (TransConvLSTM) layer that exploits transposed convolutions to recover the resolution lost due to the pooling layers. In the same fashion as for the ConvLSTM layer, the TransConvLSTM layer inserts a transposed CNN *inside* the state update function of an LSTM with peephole connections

$$\begin{aligned}
 \mathbf{i}_t &= \sigma \left(\mathbf{W}_{ix}^{(L)} \circledast \cdots \circledast \rho \mathbf{W}_{ix}^{(1)} \circledast \rho \mathbf{W}_{ix}^{(0)} \circledast \mathbf{x}_t + \mathbf{W}_{ih} * \mathbf{h}_{t-1} + \mathbf{W}_{ic} * \mathbf{c}_{t-1} + \mathbf{b}_i \right), \\
 \mathbf{f}_t &= \sigma \left(\mathbf{W}_{fx}^{(L)} \circledast \cdots \circledast \rho \mathbf{W}_{fx}^{(1)} \circledast \rho \mathbf{W}_{fx}^{(0)} \circledast \mathbf{x}_t + \mathbf{W}_{fh} * \mathbf{h}_{t-1} + \mathbf{W}_{fc} * \mathbf{c}_{t-1} + \mathbf{b}_f \right), \\
 \tilde{\mathbf{c}}_t &= \tanh \left(\mathbf{W}_{cx}^{(L)} \circledast \cdots \circledast \rho \mathbf{W}_{cx}^{(1)} \circledast \rho \mathbf{W}_{cx}^{(0)} \circledast \mathbf{x}_t + \mathbf{W}_{ch} * \mathbf{h}_{t-1} + \mathbf{b}_c \right), \\
 \mathbf{c}_t &= \mathbf{f}_t \odot \mathbf{c}_{t-1} + \mathbf{i}_t \odot \tilde{\mathbf{c}}_t, \\
 \mathbf{o}_t &= \sigma \left(\mathbf{W}_{ox}^{(L)} \circledast \cdots \circledast \rho \mathbf{W}_{ox}^{(1)} \circledast \rho \mathbf{W}_{ox}^{(0)} \circledast \mathbf{x}_t + \mathbf{W}_{oh} * \mathbf{h}_{t-1} + \mathbf{W}_{oc} * \mathbf{c}_{t-1} + \mathbf{b}_o \right), \\
 \mathbf{h}_t &= \mathbf{o}_t \odot \tanh(\mathbf{c}_t).
 \end{aligned} \tag{5.3}$$

The TransConvLSTM applies multiple layers of transposed convolutions (\circledast) with unit stride and "same" padding, followed by a last transposed convolution whose stride is a hyperparameter of the model and whose output shape is fixed to be the same as the one of the corresponding ConvLSTM in the encoding pathway (when stride > 1 multiple output shapes are possible, see the a parameter in Relationship 14 in Chapter 2). Finally, as was done for the encoding pathway, every convolution on the input apart from the last one is followed by a *ReLU* nonlinearity to keep the typical LSTM behavior intact.

5.2.3 Bidirectional RNNs

Bidirectional RNNs (Bi-RNNs) (Schuster and Paliwal, 1997) have been successfully employed in the literature for image and video related tasks (Graves and Schmidhuber, 2009; Visin *et al.*, 2015; Du *et al.*, 2015; Visin *et al.*, 2016). Given an input sequence, Bi-RNNs move over it in both directions at the same time, i.e., from the first element forwards and from the last element backwards. This allows them to integrate information coming from previous and following elements at each position of the sequence. In videos, this ensures a smoother temporal consistency in the predictions. In contrast with (Shi *et al.*, 2015), the DEConvLSTM model exploits bidirectional LSTMs to enforce temporal coherence in the predictions.

The forward and backward passes can be combined at each time step either via concatenation over the feature maps axis, as initially suggested by (Schuster and Paliwal, 1997), or by summing them elementwise. Both alternatives have been explored in the

early exploratory experiments for the DEConvLSTM model, including a variant of the sum that learns the parameters of a weighted sum rather than performing an arithmetic mean

$$RNN_t^{\leftrightarrow} = \alpha_t RNN_t^{\leftarrow} + (1 - \alpha_t) RNN_t^{\rightarrow}, \quad \text{for } \forall t \text{ in sequence,} \quad (5.4)$$

and an alternative variant with the same parameter α shared across all the time steps. Concatenation seems to give slightly better performance and has therefore been selected as combination method for the rest of the experiments. However, as a future work, it could be interesting to assess whether the accuracy gain justifies the higher memory consumption.

5.2.4 Skip Connections

One very popular component of many recent ANN-based architectures are skip connections (see e.g., Sermanet *et al.*, 2013b; Liu *et al.*, 2015b; Long *et al.*, 2015a; Srivastava *et al.*, 2015b; Bell *et al.*, 2015; He *et al.*, 2015; Hariharan *et al.*, 2015b; Honari *et al.*, 2016), which add a connection between earlier layers in the hierarchy and downstream layer *skipping* the intermediate ones. This has the desirable property of ensuring a gradient flow to the early layers of the architecture even in very deep models and has been proven to improve the performance of many tasks. Furthermore, skip connections are especially useful when high resolution spatial information is needed in the last stages. When it comes to images and videos semantic segmentation this is a crucial element to recover detailed informations on where the objects are, and this improves the upsampling precision of the decoding pathway.

The DEConvLSTM model follows this well-established practice as well. The TransConvLSTM layers are parametrized so that they emit a feature map of the same resolution as the corresponding encoding layer (see Figure 5.1). The skip connections reflect this shape pattern linking the encoding layers to the decoding layers with the same resolution. Similarly to the case of bidirectional RNNs (see Section 5.2.3), concatenating the skipped feature maps with the corresponding upsampled feature maps rather than summing them together seems to give the best results. The reason for this might be that the elementwise sum of the feature maps constrains the model to be conservative in the upsampling pathway not to overcome the information coming from the early layers. On the contrary, by concatenating the feature maps together the model has complete freedom on the values and the magnitude of the upsampled feature maps and the information coming from the skipped connections is always preserved.

5.3 Experiments

5.3.1 Datasets

CamVid: Motion-based Video Segmentation

The Cambridge-driving Labeled Video Database (CamVid) (Brostow *et al.*, 2009)² has been introduced in Section 4.3.1. It is a motion based video segmentation dataset composed by three sequences captured from the perspective of a person driving a vehicle, with

²<http://mi.eng.cam.ac.uk/research/projects/VideoRec/CamVid/>

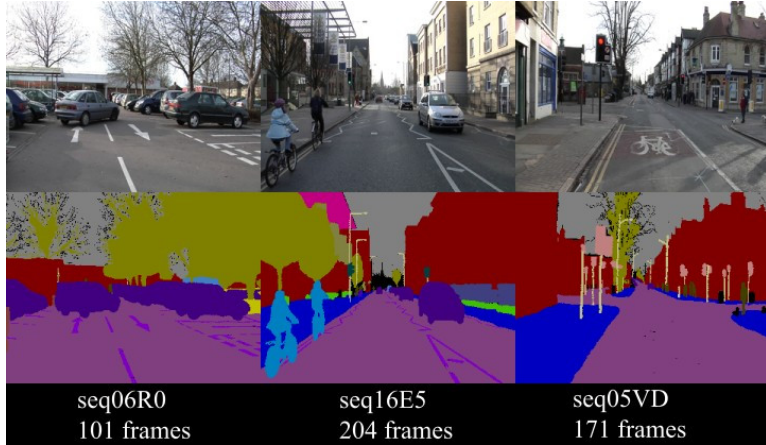


Figure 5.2: An example of ground truth segmentation for the CamVid dataset.

resolution 960×720 pixels, at 30 frames per second. The dataset contains 32 classes and a small number of pixels have been labeled as "void", when it was not possible to find a proper match with any of the 32 classes. The CamVid dataset consists of 367 training, 101 validation, and 233 test images, for a total of 701 images and corresponding annotations. The DEConvLSTM model has been trained on the same variant of the dataset as the one used by (Badrinarayanan *et al.*, 2015a), that consists of a subset of 11 class categories and downsamples the images by a factor of 2 resulting in a final 480×360 resolution. The dataset contains video sequences, but in the literature it has mostly been used for still image semantic segmentation. See Figure 5.2 for a sample with ground truth from each of the three sequences.

Gatech: Geometric Context Video Segmentation

The Gatech dataset (Raza *et al.*, 2013)³ is a geometric scene understanding dataset, which consists of 63 videos for training/validation and 38 for testing. Each video has between 50 and 300 frames (with an average of 190). A pixel-wise segmentation map is provided for each frame. There are 8 classes in the dataset: *sky*, *ground*, *buildings*, *porous*, *humans*, *cars*, *vertical mix* and *general mix*. The dataset was originally built to learn 3D geometric structure of outdoor video scenes. A sample with ground truth segmentation taken from the Gatech dataset can be seen in Figure 5.3.

DAVIS: Densely Annotated Video Segmentation

The DAVIS dataset (Perazzi *et al.*, 2016)⁴ has been made publicly available very recently. It contains 50 high-resolution Full HD video sequences, with all the frames densely labeled. The sequences have been carefully chosen to contain the typical major challenges of video segmentation and the dataset comes with a comprehensive benchmark of many

³<http://www.cc.gatech.edu/cpl/projects/videogeometriccontext/>

⁴ <https://graphics.ethz.ch/perazzif/davis/>

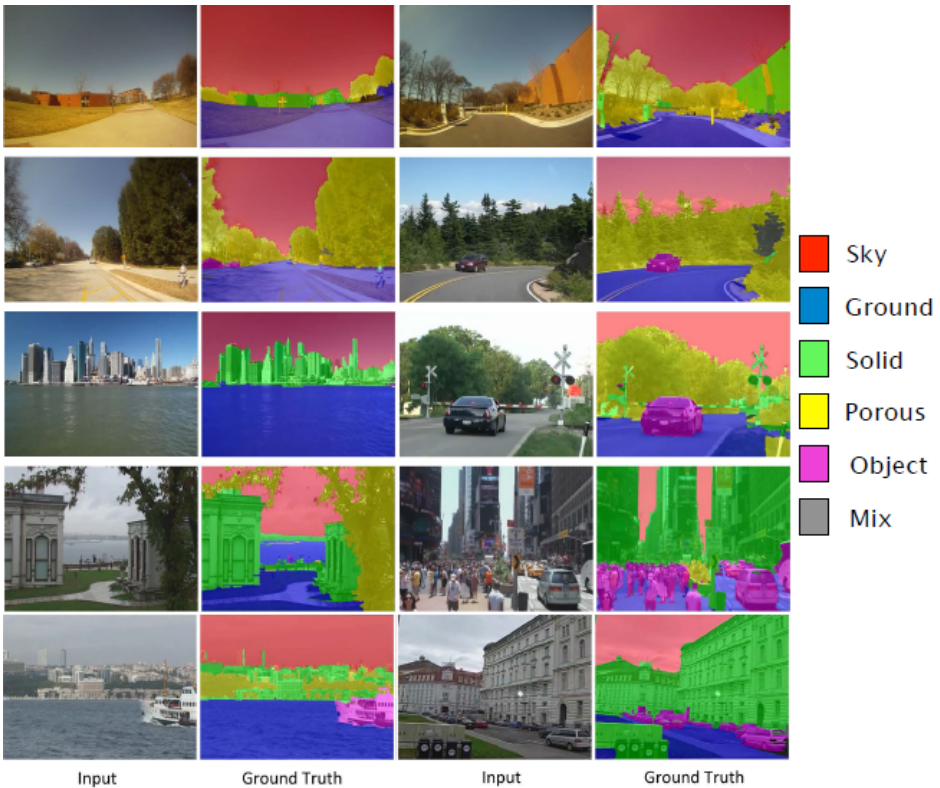


Figure 5.3: An example of ground truth segmentation for the Gatech dataset.

state-of-the-art methods on three complementary metrics that measure the spatial accuracy of the segmentation, the quality of the silhouette and the temporal coherence. Due to memory restrictions, these tests were run on a version of the dataset downsampled at 480p resolution. To make it possible to compare with this state-of-the-art, the DEConvLSTM has been trained on the resized version too. Finally, the videos are annotated with attributes such as *occlusion*, *non-linear deformation* and *motion blur*. These annotations were not taken into account when training the DEConvLSTM model on this dataset. A ground truth segmentation example for the DAVIS dataset can be seen in Figure 5.4.

5.3.2 Data augmentation and preprocessing

Training on video semantic segmentation datasets is very time consuming, in fact the prediction of a segmentation mask requires to densely process a temporal window for each frame. This limits the size of the batches that can be processed and slows down training.

With the goal of collecting a preliminary assessment of the performance of the model and of its flexibility in tackling different kinds of datasets, we chose to keep the training time as contained as possible without resorting to data augmentation techniques. However, it has to be pointed out that some degree of improvement can be expected from the



Figure 5.4: An example of ground truth segmentation for the DAVIS dataset.

introduction of some data augmentation, e.g., by distorting the frames with affine transformations, by flipping and rotating them or by shifting the intensity values of all the pixels by a random value.

In the same spirit, the only preprocessing technique adopted – apart from resizing the videos to allow a comparison with the state-of-the-art (see Section 5.3.1) – was to crop the frames randomly selecting an image patch of (224, 224) resolution during training to reduce the memory usage and speed up the training.

5.3.3 Experimental settings

A first exploratory phase allowed to test several different architectures on the relatively small CamVid dataset in order to select a suitable starting point for the rest of the experiments. The principal hyperparameters of the DEConvLSTM model are the number of encoding and decoding layers, as well as the depth of their inner convolutions. As explained in Section 5.2.4, we chose to constrain, by design, the number of decoding layers to be the same as the number of encoding layers, to allow for the skip connections structure to be symmetrical with respect to the middle feature map resolution of the network. The number of encoding (and therefore decoding) layers that empirically appeared to be optimal is 5, and has been used consistently throughout the experiments. Similarly, the number of inner convolutions and transposed convolutions has been set to 2 (per layer) and their hyperparameters – namely the number of filters per sublayer (**nf**), filters size per sublayer (**fs**) and stride per sublayer (**st**) – have been fixed as shown in Table 5.1 and Table 5.2.

Throughout the experiments a light Dropout (Srivastava *et al.*, 2014) with drop probability 0.2 was used as regularization technique, as well as a regularization of magnitude 0.0001 for both the neural network weights and the batch normalization. Optimization was carried out with RMSProp (Tieleman and Hinton, 2012) with learning rate $1e^{-4}$ and gradient clipping of 10. Finally, feature-wise batch normalization was applied before each

5.3. Experiments

Layers	1	2	3	4	5
nf	[64, 64]	[128, 128]	[256, 256]	[384, 384]	[512, 512]
fs	[1x1, 3x3]				
st	[2, 2]	[2, 2]	[2, 2]	[2, 2]	[2, 2]

Table 5.1: ConvLSTM hyperparameters. Number of filters per sublayer (**nf**), filters size per sublayer (**fs**) and stride per sublayer (**st**).

Layers	1	2	3	4	5
nf	[384, 384]	[256, 256]	[128, 128]	[64, 64]	[64, 64]
fs	[1x1, 3x3]				
st	[2, 2]	[2, 2]	[2, 2]	[2, 2]	[2, 2]

Table 5.2: TransConvLSTM hyperparameters. Number of filters per sublayer (**nf**), filters size per sublayer (**fs**) and stride per sublayer (**st**).

layer with an amount of momentum that varied from dataset to dataset.

5.3.4 Results

The DEConvLSTM model has been studied on three different datasets. A first set of experiments was run on CamVid to fix some of the hyperparameters of the model. Afterwards, the bigger Gatech and DAVIS datasets were taken into account.

All the experiments on CamVid were run with batch size 5, training on cropped patches of 224×224 . The learning procedure was interrupted with early stopping on the average Intersection over Union (IoU) of the validation set. The main goal of these experiments was not to reach state-of-the-art performance, but rather to assess the sensitivity of the model to different hyperparameters. Table 5.4 reports the results of some of these preliminary experiments with different optimizers and various sequence lengths. The models suffer from some generalization issues on this dataset. This is not too surprising given the limited number of images in the CamVid dataset, as will be discussed in more detail in Section 5.4.

The results of the DEConvLSTM model with sequences of length 3, fine-tuned for 100 epochs on images at full resolution is compared in Table 5.3 with the state-of-the-art on CamVid. The model performs comparably to the state-of-the-art of the last year; there is a margin for improvement, which could be probably gained, at least in part, by reducing the generalization issues with stronger regularization and relying on data augmentation to diminish the overfitting. However not too much effort was spent on hyperparameters tuning on this dataset, as the main goal was to gain confidence with the model rather than to reach the state-of-the-art.

Most of the training effort was spent on the Gatech dataset, a well known dataset for structured prediction. The performance of the DEConvLSTM model on this dataset is remarkable, as reported in Table 5.5. The model aligns with the state-of-the-art without resorting to data augmentation techniques, or finetuning on full resolution (i.e., without cropping the frames), which can be expected to further improve the result, setting a new state-of-the-art for this dataset. Figure 5.5 presents some samples on the Gatech dataset. Although the model is usually able to produce precise segmentation even on fine-grained

Method	Global accuracy	Avg IoU
SegNet-Basic (Badrinarayanan <i>et al.</i> , 2015a)	82.8	46.3
SegNet (Badrinarayanan <i>et al.</i> , 2015a)	88.6	50.2
ReSeg (Visin <i>et al.</i> , 2016)	88.7	58.8
Dilation (Yu and Koltun, 2015)	n/a	65.3
Dilation + FSO - DiscreteFlow (Kundu <i>et al.</i> , 2016)	n/a	66.1
<i>DEConvLSTM (finetuned)</i>	87.0	53.9

Table 5.3: Results on the CamVid dataset. Pixel accuracy and average Intersection over Union (IoU) are reported. Higher is better.

Optimizer	Sequence length	Global accuracy			Avg IoU		
		Test	Validation	Train	Test	Validation	Train
RMSProp	3	78.0	90.2	91.5	37.8	58.4	60.3
Adam	3	78.8	90.3	91.4	38.2	58.3	59.8
RMSProp	1	84.5	94.2	96.5	50.7	72.1	84.7

Table 5.4: The results of the experiments on the effects of time correlation on the CamVid dataset. Pixel accuracy and average Intersection over Union (Avg. IoU) are reported. The model seems to fail to generalize properly.

details of the most represented classes, such as sky and solid (the buildings), it can suffer on the less frequent ones, such as humans and cars. A more in-depth discussion on this issue will be provided in the following section.

The research carried out on this dataset allowed to evaluate the effectiveness of the proposed architecture in non-trivial settings where the time component has to be exploited to obtain convincing predictions. The results on the Gatech dataset show that the proposed architecture can address successfully the video segmentation task and suggest to carry on experimentation, e.g., adding data augmentation and finetuning the network on full resolution sequences, to further improve the state of the art.

Encouraged by the good results on Gatech, we also tested the network on the recently introduced DAVIS dataset for dense semantic segmentation. With only cursory hyperparameter search around the settings that worked best on the Gatech dataset, the DEConvLSTM obtains results comparable with the state-of-the-art of a few years ago. Table 5.6 reports the results of the initial experiments with the DEConvLSTM model on this dataset and Figure 5.6 shows an example of prediction made by the model.

The experiments conducted on this dataset are not enough to draw final conclusions, but one failure mode of the DEConvLSTM model on this task seems to be not to recognize the goal properly. The task in DAVIS is to segment only the main element in the scene and by inspecting the segmentation samples (see, e.g., Figure 5.7) it appears that sometimes the network has a hard time identifying what to segment and what to ignore and ends up focusing too much on the background, heavily decreasing the overall segmentation performance. More experiments have to be conducted to address this issue; one option could be to increase the capacity of the temporal pathway to rely more on the temporal information to segment the main element of the scene that in these datasets is usually the one that moves and changes the most. This early result is very encouraging and calls for more thorough experiments on this dataset.

5.3. Experiments

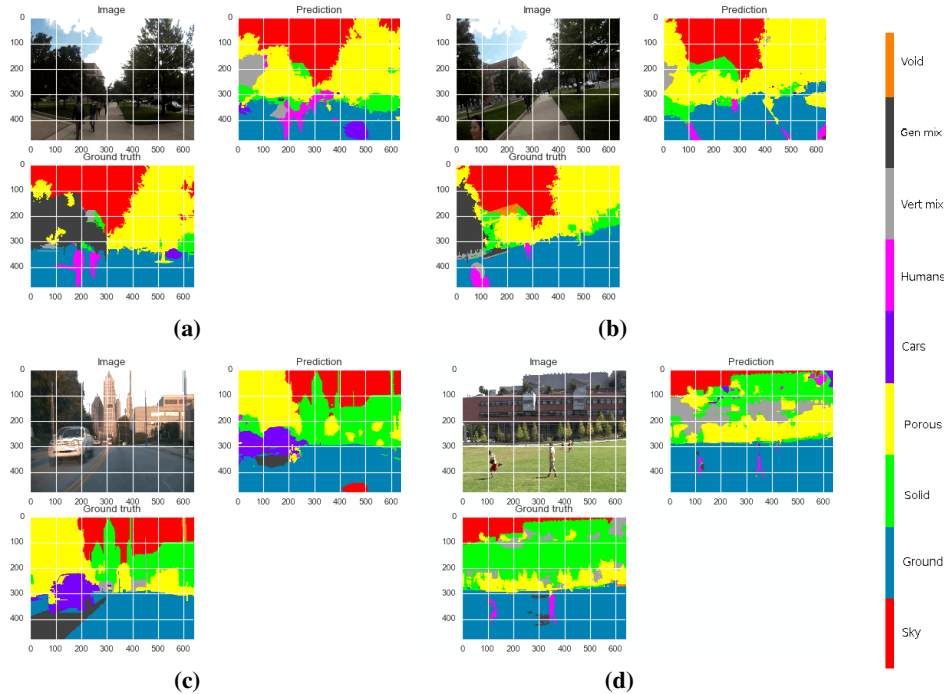


Figure 5.5: Segmentation samples on the Gatech dataset.

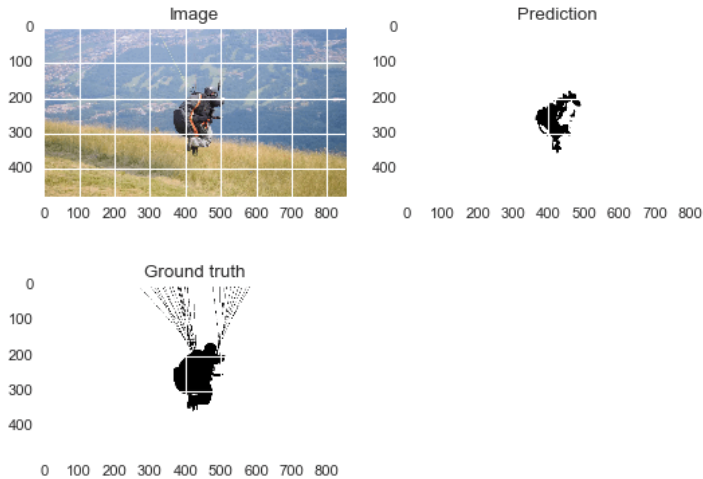


Figure 5.6: An example of proper segmentation produced by the DEConvLSTM model on the DAVIS dataset.

Method	Global accuracy
2D-V2V (Tran <i>et al.</i> , 2015)	55.7
V2V-0 (Tran <i>et al.</i> , 2015)	66.7
Conv3b + Up (Tran <i>et al.</i> , 2015)	69.7
Conv4b + Up (Tran <i>et al.</i> , 2015)	72.7
Conv5b + Up (Tran <i>et al.</i> , 2015)	72.1
V2V (Tran <i>et al.</i> , 2015)	76.0
DEConvLSTM	76.1

Table 5.5: Results on the Gatech dataset. Pixel accuracy is reported (higher is better). IoU is not reported as customary in the literature for this dataset.

Method	Avg IoU
Temporal superpixels (Chang <i>et al.</i> , 2013)	35.8
SeamSeg (Ramakanth and Babu, 2014)	55.6
Efficient hierarchical graph-based video segmentation (Grundmann <i>et al.</i> , 2010)	59.6
Jumpcut (Fan <i>et al.</i> , 2015)	60.7
Fully Connected Object Proposals for Video Segmentation (Perazzi <i>et al.</i> , 2015)	63.1
Bilateral space video segmentation (Märki <i>et al.</i> , 2016)	66.5
<i>DEConvLSTM</i>	56.8

Table 5.6: Results on the Davis dataset. Average Intersection over Union (IoU) is reported. We compare to⁵, where pixel accuracy is not reported.

5.4 Discussion

One of the first goals of the experiments with the DEConvLSTM model was to assess its effectiveness in exploiting the temporal correlation among frames in the task of video spatial segmentation. To this end, several tests were run on CamVid, training the same model with different lengths of the sequence.

CamVid has been mostly used in the literature in a single image segmentation setting, rather than considering the frames altogether as a video. Indeed, on this dataset the model performed better when the sequence length was set to 1, i.e., when the temporal correlation was not taken into account. This is not too surprising, since this dataset is composed by frames captured at 30 fps, but only one frame out of approximately 30 is annotated and available for training. The experiments show that trying to exploit temporal correlation at 1 Hz is very non-trivial, and results in a massive drop of performance as emerges clearly from the results reported in Table 5.4. Another aspect that clearly emerges from the results is the performance drop between the test set and the other sets. Overfitting is an important problem when training on the CamVid dataset, due to the size of the training set that is quite small, especially for big models like the DEConvLSTM.

On the contrary, there is evidence in the literature that exploiting the temporal correlation between frames improves performance on the Gatech dataset (Tran *et al.*, 2015). The results reported in Table 5.5 show that the DEConvLSTM model is an interesting architecture for the video semantic segmentation task. Furthermore, generalization seems to be much better on Gatech with respect to CamVid, in fact the drop in performance be-

⁵https://graphics.ethz.ch/~perazzif/davis/soa_compare.php

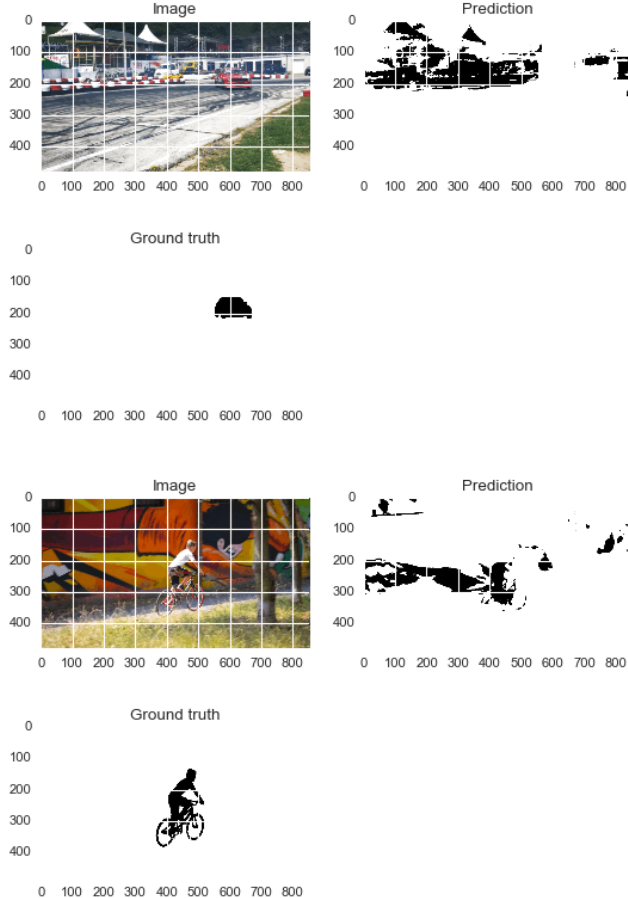


Figure 5.7: A frequent failure mode of the model on the DAVIS dataset is to focus on segmenting the background rather than the main element in the scene.

tween the validation and the test set is remarkably contained around 2%, as opposed to the 10 – 15% drop typically experienced in CamVid.

By analyzing some of the segmentation samples (see Figure 5.5) it is evident that the model learns a good representation of the most represented objects of the dataset (e.g., the buildings (labeled as solid) and the sky), and is able to segment fine-grained details such as the leaves of the trees (Figure 5.5a) and, although not perfectly, far away people (such as those in Figure 5.5d). There are still some imperfections in the segmentation which could be caused by misleading ground truth labels that could be making it less clear for the model to distinguish between some of the classes. Take for example Figures 5.5a and 5.5b, where the ground truth label for some of the trees is "porous" and for some other is "vertical mix"; similarly in Figure 5.5c part of the street is labeled as "ground" and some of it as "general mix", even if there is no apparent difference between the two

parts of the street in the image. These kind of unclear semantic is a probable cause for the uncertainty of the model in some cases, such as the mixed segmentation of the building in the background in Figure 5.5d.

Unfortunately the model did not perform as well when trained *using the same hyperparameters* on the Davis dataset. The results on this dataset are not conclusive as the dataset is fairly new and not enough experimentation has been conducted to draw any conclusion. It seems that the model could benefit from an exploration of the hyperparameters that best push it to focus more on the main object of the scene. This could of course also be obtained by more invasive modifications of the model, e.g., the addition of an attention mechanism or of a spatial prior that could be learned by a CRF, or in a more trivial way just by adding a hand-engineered spatial prior, as the object of interest tends to be centered in the frames. Nevertheless, since our interest lies more in assessing the learning capabilities of the model rather than in obtaining the absolute performance value, we plan to focus mostly on the study of variations of the current architecture rather than on relying on hand engineered solutions to improve the final score.

One interesting discovery, valid for all the experiments ran so far, is that using the per-batch statistics for batch normalization at test time (rather than the more common strategy of re-using the running statistics collected during training) significantly improved the results on all the three datasets. In this setting the statistics to perform the feature-wise normalization of the activations of the network are computed on the test minibatch under exam, as opposed to using the statistics collected on the whole training set. This seems to suggest a difference in the distributions of the data in the training and the test set or, more likely, a higher-than-usual variance of the images of the dataset. Bigger dataset would likely not suffer from this issues.

Another crucial factor to achieve a good optimization is to select the right amount of momentum in the computation of the batch normalization statistics. We argue that the reason for both behaviors lies in the high variance of the input data. The datasets are in fact composed by sequences of frames coming from different videos that can vary consistently in terms of, e.g., brightness, scale and noise. Relying too heavily on past statistics in this setting can be harmful.

Video semantic segmentation is a hard task to tackle. CNNs are known to be data hungry, as proved by the great performance leap that followed the introduction of large datasets for object classification (Russakovsky *et al.*, 2014). The next milestone for computer vision research is reaching a good understanding of videos in structured prediction related tasks. Good datasets with large amounts of densely annotated video data are still missing, even if the community is beginning to make an effort to fill in the gap (see e.g., Perazzi *et al.*, 2016; Lin *et al.*, 2014b). More work is needed to speed up the models, study new loss functions that allow to optimize more closely non-derivable metrics such as IoU and reuse computation exploiting similarity in consecutive frames. Nonetheless it is already possible to challenge non-neural methods and reach reasonable results - when not state-of-the-art performance. Indeed the results obtained with DEConvLSTM show that coupling CNNs, transposed CNNs and LSTMs can be an effective way to tackle structured prediction problems in video, building on the speed of CNNs to process spatial information and on the ability of RNNs to retain information through several steps of computation.

CHAPTER 6

Conclusion

Machine Learning is a thrilling field of research to work in. The industrial revolutions changed the way work was intended, shifting the burden of hard physical labour from animals and humans to machines and making habits that were common a few years ago, now unconceivable. Machine Learning has the same potential impact on society, ideally freeing people from boring, repetitive yet extremely important works (think for instance to house keeping, streets cleaning, garbage collection, video surveillance and customer service) to let us focus on more stimulating and self-improving tasks. The potential of this technology may seem endless, yet our understanding of many of its inner mechanisms is still partial and it is easy to underestimate the non-trivial amount of knowledge and experience required to be successful. Nonetheless, the field is advancing very fast in a number of exciting directions and ML already established the state-of-the-art in many areas of application.

I am particularly interested in applying ML to vision problems because we, as humans, rely heavily on vision for our daily operations. Improvements in the technology at our disposal to interpret visual data can have a direct and remarkably rapid impact on many practical applications such as detecting street signs, pedestrians, cars and other key landmarks to assist or automate driving; automatically analyze medical images detecting, e.g., anomalies, tumors, ulcers and bleeding; aid surgeons during surgeries; retrieve images and videos given a description or some keywords; automatically caption images and videos; assist humans in all those repetitive, yet critical tasks such as video surveillance and counter-terrorism; improve human-machine interaction; improve the quality of life for visually impaired people, and much more.

Chapter 6. Conclusion

I focused my research on Recurrent Neural Networks and RNN-based models for their ability to store, retrieve and update information across subsequent steps of computation. I believe one of the key factors to interpret images is to process them in an iterative fashion, keeping trace of every element that can be needed for the interpretation of unseen parts of the image. If this is important with still images, being able to compress and store information to fully understand the semantic of videos is even more crucial.

I firstly addressed the problem of object classification, introducing ReNet, a novel model that, in contrast with most of the literature at the time, is based on 4 intertwined RNNs. The carefully designed interaction between these RNNs allowed the model to capture the full context of the image already at the first layer. Driven by the positive results and the encouraging interest of the community, I addressed the much more challenging task of semantic segmentation, moving from classifying one image with a single label to classifying each single pixel of the image as being part of one out of a set of potential categories. The proposed ReSeg model takes advantage from a similar inner structure as ReNet, further improved by the adoption of pretrained CNNs to extract rich local descriptors from the images, as well as the addition of transposed convolutional layers to upsample the intermediate feature maps in a trainable end-to-end fashion. This model was selected by the organizers of the DeepVision Workshop at CVPR 2016 to receive the best paper award. Moreover, an extended version of the ReSeg paper with more experiments and more in-depth analysis of the properties of the model will become a chapter of the upcoming book on the CVPR 2016 DeepVision Workshop.

To conclude my analysis of RNN-based model applied to visual data I moved from semantic segmentation in images, to semantic segmentation in videos. The complexity of the problem in this case is dramatically increased by the lack of large amounts of labeled data that makes it more challenging to beat ad-hoc hand-engineered classical computer vision methods. Moreover, the training time on these datasets is considerably longer and makes experimenting with large models slow and in some cases unfeasible. Dealing with video segmentation required a very careful inspection of every component of the model and an accurate planning of the experiments. To address this task I proposed a model that merges direct convolutions, transposed convolutions and RNNs in a unique coherent structure. The proposed DEConvLSTM model exploits the speed of CNNs to process spatial information and the ability of RNNs to retain information through several steps of computation. This model proved to be a valid architecture for video semantic segmentation, pairing the state of the art on one of the historically most used benchmarks and achieving results aligned with the state-of-the-art of the last year on two other datasets with just cursory hyperparameters exploration.

Video semantic segmentation is a hard task to solve, yet it is clearly the next milestone for computer vision research. The advancement in hardware and software technologies will impact the training speed, which currently represents a big impediment to a quick experimentation of ideas in many fields, including video semantic segmentation. Moreover, CNNs are known to be data hungry, as proved by the great performance leap that followed the introduction of large datasets for object classification (Russakovsky *et al.*, 2014). Good datasets with large amounts of densely annotated video data are still missing, even if the community is beginning to make an effort to fill the gap (see e.g., Perazzi *et al.*, 2016; Lin *et al.*, 2014b).

To compensate for the lack of data, a direction of research I intend to investigate is

the initialization of the internal direct convolutions of the DEConvLSTM model with pre-trained VGG-16 weights, modifying the shape of the ConvLSTM layers to mimic those of the VGG-16 model. The performance of the DEConvLSTM model could be also improved by finetuning on full resolution images, as opposed to cropped patches, as done during the rest of the training to keep the training time within reasonable limits. Other possible improvements are the addition of data augmentation, to partially address the lack of training data, the introduction of new loss functions to optimize more closely non-derivable metrics such as IoU, and the reuse of computation exploiting similarity in consecutive frames. Finally an interesting improvement could be the addition of skip-connections between the convolutions and the transposed convolutions *inside* the ConvLSTM and TransConvLSTM layers (i.e., connecting the inner convolution of one ConvLSTM layer to the inner transposed convolution of the corresponding TransConvLSTM layer). This is unfortunately non-trivial to implement in most of current frameworks for ML, due to very optimized, yet not always flexible, implementation of loops, which are a core part of RNNs.

There are many other exciting possible directions of research in this field, such as the introduction of temporal attention mechanisms, to decouple a coarse high-level analysis of the frame from a fine-scale detailed computation inside the detected areas of interest; the study of much deeper architecture such as the ones currently used in image classification (see, e.g., Szegedy *et al.*, 2016; He *et al.*, 2015); the study of optimization techniques that better propagate the gradient through many layers (see, e.g., He *et al.*, 2015; Huang *et al.*, 2016; Gulcehre *et al.*, 2016); the study on how to help the network to better model the input data distribution introducing a next frame prediction secondary task (see, e.g., Mahjourian *et al.*, 2016); training in a multi-objective setting, e.g., trying to predict the video segmentation and a caption describing the video sequence at the same time; the use of hierarchical LSTMs (see, e.g., Koutnik *et al.*, 2014; Chung *et al.*, 2016) to better capture the time dependencies between far away frames.

Bibliography

- Abdel-Hamid, O., Mohamed, A., Jiang, H., and Penn, G. (2012). Applying convolutional neural networks concepts to hybrid nn-hmm model for speech recognition. In *Acoustics, Speech and Signal Processing (ICASSP), 2012 IEEE International Conference on*.
- Agrawal, M., Konolige, K., and Blas, M. R. (2008). Censure: Center surround extrema for realtime feature detection and matching. In *European Conference on Computer Vision*, pages 102–115. Springer.
- Alcantarilla, P. F., Bartoli, A., and Davison, A. J. (2012). Kaze features. In *European Conference on Computer Vision*, pages 214–227. Springer.
- Arpit, D., Zhou, Y., Kota, B. U., and Govindaraju, V. (2016). Normalization propagation: A parametric technique for removing internal covariate shift in deep networks. *arXiv preprint arXiv:1603.01431*.
- Atkins, M. S. and Mackiewich, B. T. (1998). Fully automatic segmentation of the brain in mri. *IEEE transactions on medical imaging*, **17**(1), 98–107.
- Azzopardi, G. and Petkov, N. (2013). Trainable COSFIRE filters for keypoint detection and pattern recognition. *IEEE Trans. Pattern Anal. Mach. Intell.*, **35**(2), 490–503.
- Badrinarayanan, V., Handa, A., and Cipolla, R. (2015a). SegNet: A Deep Convolutional Encoder-Decoder Architecture for Image Segmentation. page 5.
- Badrinarayanan, V., Handa, A., and Cipolla, R. (2015b). SegNet: A Deep Convolutional Encoder-Decoder Architecture for Robust Semantic Pixel-Wise Labelling.
- Bahdanau, D., Cho, K., and Bengio, Y. (2014). Neural machine translation by jointly learning to align and translate. Technical report, arXiv:1409.0473.
- Bahdanau, D., Cho, K., and Bengio, Y. (2015). Neural machine translation by jointly learning to align and translate. In *International Conference on Learning Representations (ICLR 2015)*.
- Bay, H., Ess, A., Tuytelaars, T., and Van Gool, L. (2008). Speeded-up robust features (surf). *Computer vision and image understanding*, **110**(3), 346–359.

Bibliography

- Bell, S., Zitnick, C. L., Bala, K., and Girshick, R. (2015). Inside-outside net: Detecting objects in context with skip pooling and recurrent neural networks. *arXiv preprint arXiv:1512.04143*.
- Belongie, S., Malik, J., and Puzicha, J. (2002). Shape matching and object recognition using shape contexts. *IEEE transactions on pattern analysis and machine intelligence*, **24**(4), 509–522.
- Bengio, Y., Simard, P., and Frasconi, P. (1994). Learning long-term dependencies with gradient descent is difficult. *IEEE Transactions on Neural Networks*, **5**(2), 157–166.
- Bengio, Y., Boulanger-Lewandowski, N., and Pascanu, R. (2013). Advances in optimizing recurrent networks. In *Acoustics, Speech and Signal Processing (ICASSP), 2013 IEEE International Conference on*, pages 8624–8628. IEEE.
- Bertelli, L., Yu, T., Vu, D., and Gokturk, B. (2011). Kernelized structural svm learning for supervised object segmentation. In *Computer Vision and Pattern Recognition (CVPR), 2011 IEEE Conference on*, pages 2153–2160. IEEE.
- Bishop, C. M. (2006). *Pattern Recognition and Machine Learning*. Springer.
- Blake, A., Kohli, P., and Rother, C. (2011). *Markov random fields for vision and image processing*. Mit Press.
- Borenstein, E. (2004). Combining top-down and bottom-up segmentation. In *In Proceedings IEEE workshop on Perceptual Organization in Computer Vision, CVPR*, page 46.
- Bourdev, L., Maji, S., Brox, T., and Malik, J. (2010). Detecting people using mutually consistent poselet activations. In *European conference on computer vision*, pages 168–181. Springer.
- Boureau, Y., Bach, F., LeCun, Y., and Ponce, J. (2010a). Learning mid-level features for recognition. In *Proc. International Conference on Computer Vision and Pattern Recognition (CVPR'10)*. IEEE.
- Boureau, Y., Ponce, J., and LeCun, Y. (2010b). A theoretical analysis of feature pooling in vision algorithms. In *Proc. International Conference on Machine learning (ICML'10)*.
- Boureau, Y., Le Roux, N., Bach, F., Ponce, J., and LeCun, Y. (2011). Ask the locals: multi-way local pooling for image recognition. In *Proc. International Conference on Computer Vision (ICCV'11)*. IEEE.
- Brostow, G. J., Shotton, J., Fauqueur, J., and Cipolla, R. (2008). Segmentation and recognition using structure from motion point clouds. In *ECCV (1)*, pages 44–57.
- Brostow, G. J., Fauqueur, J., and Cipolla, R. (2009). Semantic object classes in video: A high-definition ground truth database. *Pattern Recognition Letters*, **30**(2), 88–97.
- Brox, T., Bourdev, L., Maji, S., and Malik, J. (2011). Object segmentation by alignment of poselet activations to image contours. In *Computer Vision and Pattern Recognition (CVPR), 2011 IEEE Conference on*, pages 2225–2232. IEEE.
- Burges, C. J. (1998). A tutorial on support vector machines for pattern recognition. *Data mining and knowledge discovery*, **2**(2), 121–167.
- Byeon, W., Breuel, T. M., Raue, F., and Liwicki, M. (2015). Scene labeling with lstm recurrent neural networks. In *Proceedings of the IEEE Conference on Computer Vision and Pattern Recognition*, pages 3547–3555.

- Carreira, J. and Sminchisescu, C. (2010). Constrained parametric min-cuts for automatic object segmentation. In *Computer Vision and Pattern Recognition (CVPR), 2010 IEEE Conference on*, pages 3241–3248. IEEE.
- Chang, J., Wei, D., and Fisher, J. W. (2013). A video representation using temporal superpixels. In *Proceedings of the IEEE Conference on Computer Vision and Pattern Recognition*, pages 2051–2058.
- Chen, C., Ozolek, J. A., Wang, W., and Rohde, G. K. (2011). A pixel classification system for segmenting biomedical images using intensity neighborhoods and dimension reduction. In *2011 IEEE International Symposium on Biomedical Imaging: From Nano to Macro*, pages 1649–1652. IEEE.
- Chen, C. W., Luo, J., and Parker, K. J. (1998). Image segmentation via adaptive k-mean clustering and knowledge-based morphological operations with biomedical applications. *IEEE Transactions on Image Processing*, **7**(12), 1673–1683.
- Chen, L.-C., Barron, J. T., Papandreou, G., Murphy, K., and Yuille, A. L. (2015). Semantic image segmentation with task-specific edge detection using cnns and a discriminatively trained domain transform. *arXiv preprint arXiv:1511.03328*.
- Cheng, H.-D., Jiang, X., Sun, Y., and Wang, J. (2001). Color image segmentation: advances and prospects. *Pattern recognition*, **34**(12), 2259–2281.
- Cho, K., van Merriënboer, B., Gulcehre, C., Bougares, F., Schwenk, H., and Bengio, Y. (2014a). Learning phrase representations using RNN encoder-decoder for statistical machine translation. In *Proceedings of the Empirical Methods in Natural Language Processing (EMNLP 2014)*. to appear.
- Cho, K., van Merriënboer, B., Bahdanau, D., and Bengio, Y. (2014b). On the properties of neural machine translation: Encoder–Decoder approaches. In *Eighth Workshop on Syntax, Semantics and Structure in Statistical Translation*.
- Chorowski, J., Bahdanau, D., Cho, K., and Bengio, Y. (2014). End-to-end continuous speech recognition using attention-based recurrent nn: First results. *arXiv:1412.1602*.
- Chung, J., Gulcehre, C., Cho, K., and Bengio, Y. (2014). Empirical evaluation of gated recurrent neural networks on sequence modeling. NIPS’2014 Deep Learning workshop, *arXiv 1412.3555*.
- Chung, J., Ahn, S., and Bengio, Y. (2016). Hierarchical multiscale recurrent neural networks. *arXiv preprint arXiv:1609.01704*.
- Ciresan, D., Meier, U., Masci, J., and Schmidhuber, J. (2012a). Multi-column deep neural network for traffic sign classification. *Neural Networks*, **32**, 333–338.
- Ciresan, D., Meier, U., and Schmidhuber, J. (2012b). Multi-column deep neural networks for image classification. Technical report, *arXiv:1202.2745*.
- Ciresan, D. C., Meier, U., Gambardella, L. M., and Schmidhuber, J. (2010). Deep big simple neural nets excel on handwritten digit recognition. *arXiv*, **abs/1003.0358**.
- Cooijmans, T., Ballas, N., Laurent, C., and Courville, A. (2016). Recurrent batch normalization. *arXiv preprint arXiv:1603.09025*.

Bibliography

- Csurka, G., Dance, C., Fan, L., Willamowski, J., and Bray, C. (2004). Visual categorization with bags of keypoints. In *Workshop on statistical learning in computer vision, ECCV*, number 1–22, pages 1–2. Prague.
- Dalal, N. and Triggs, B. (2005). Histograms of oriented gradients for human detection. *CVPR*.
- Deng, J., Dong, W., Socher, R., Li, L.-J., Li, K., and Fei-Fei, L. (2009). ImageNet: A Large-Scale Hierarchical Image Database. In *CVPR09*.
- Donahue, J., Hendricks, L. A., Guadarrama, S., Rohrbach, M., Venugopalan, S., Saenko, K., and Darrell, T. (2014). Long-term recurrent convolutional networks for visual recognition and description. *arXiv:1411.4389*.
- Drachman, D. A. (2005). Do we have brain to spare? *Neurology*, **64**(12), 2004–2005.
- Du, Y., Wang, W., and Wang, L. (2015). Hierarchical recurrent neural network for skeleton based action recognition. In *The IEEE Conference on Computer Vision and Pattern Recognition (CVPR)*.
- Dufournaud, Y., Schmid, C., and Horaud, R. (2000). Matching images with different resolutions. In *Computer Vision and Pattern Recognition, 2000. Proceedings. IEEE Conference on*, volume 1, pages 612–618. IEEE.
- Dumoulin, V. and Visin, F. (2016). A guide to convolution arithmetic for deep learning. *arXiv preprint arXiv:1603.07285*.
- Eigen, D. and Fergus, R. (2015). Predicting depth, surface normals and semantic labels with a common multi-scale convolutional architecture. In *Proceedings of the IEEE International Conference on Computer Vision*, pages 2650–2658.
- Erhan, D., Szegedy, C., Toshev, A., and Anguelov, D. (2014). Scalable object detection using deep neural networks. In *Proceedings of the 2014 IEEE Conference on Computer Vision and Pattern Recognition, CVPR '14*, pages 2155–2162, Washington, DC, USA. IEEE Computer Society.
- Everingham, M., Eslami, S. M. A., Van Gool, L., Williams, C. K. I., Winn, J., and Zisserman, A. (2015). The pascal visual object classes challenge: A retrospective. *International Journal of Computer Vision*, **111**(1), 98–136.
- Fan, Q., Zhong, F., Lischinski, D., Cohen-Or, D., and Chen, B. (2015). Jumpcut: non-successive mask transfer and interpolation for video cutout. *ACM Transactions on Graphics (TOG)*, **34**(6), 195.
- Farabet, C., Couprie, C., Najman, L., and LeCun, Y. (2013). Learning hierarchical features for scene labeling. *IEEE TPAMI*, **35**(8), 1915–1929.
- Felzenszwalb, P. F. and Huttenlocher, D. P. (2004). Efficient graph-based image segmentation. *International Journal of Computer Vision*, **59**(2), 167–181.
- Felzenszwalb, P. F., Girshick, R. B., McAllester, D., and Ramanan, D. (2010). Object detection with discriminatively trained part-based models. *IEEE transactions on pattern analysis and machine intelligence*, **32**(9), 1627–1645.
- Fukushima, K. (1980). Neocognitron: A self-organizing neural network model for a mechanism of pattern recognition unaffected by shift in position. *Biological Cybernetics*, **36**, 193–202.

- Gatta, C., Romero, A., and van de Weijer, J. (2014). Unrolling loopy top-down semantic feedback in convolutional deep networks. In *IEEE Conference on Computer Vision and Pattern Recognition, CVPR Workshops 2014, Columbus, OH, USA, June 23-28, 2014*, pages 504–511.
- Gers, F. A. and Schmidhuber, J. (2000). Recurrent nets that time and count. In *Neural Networks, 2000. IJCNN 2000. Proceedings of the IEEE-INNS-ENNS International Joint Conference on*, volume 3, pages 189–194. IEEE.
- Girshick, R., Donahue, J., Darrell, T., and Malik, J. (2013). Rich feature hierarchies for accurate object detection and semantic segmentation. Technical report, arXiv:1311.2524.
- Glorot, X. and Bengio, Y. (2010). Understanding the difficulty of training deep feedforward neural networks. In *International conference on artificial intelligence and statistics*, pages 249–256.
- Glorot, X., Bordes, A., and Bengio, Y. (2011). Deep sparse rectifier neural networks. In *AISTATS'2011*.
- Goodfellow, I., Warde-Farley, D., Mirza, M., Courville, A., and Bengio, Y. (2013). Maxout networks. In *Proceedings of The 30th International Conference on Machine Learning*, pages 1319–1327.
- Goodfellow, I., Bengio, Y., and Courville, A. (2016). Deep learning. Book in preparation for MIT Press.
- Goodfellow, I. J., Bulatov, Y., Ibarz, J., Arnoud, S., and Shet, V. (2014). Multi-digit number recognition from Street View imagery using deep convolutional neural networks. In *International Conference on Learning Representations*.
- Graham, B. (2014a). Fractional max-pooling. *arXiv*, **abs/1412.6071**.
- Graham, B. (2014b). Spatially-sparse convolutional neural networks. *arXiv*, **abs/1409.6070**.
- Graves, A. (2011). Practical variational inference for neural networks. In J. Shawe-Taylor, R. Zemel, P. Bartlett, F. Pereira, and K. Weinberger, editors, *Advances in Neural Information Processing Systems 24*, pages 2348–2356.
- Graves, A. (2013). Generating sequences with recurrent neural networks. Technical report, arXiv:1308.0850.
- Graves, A. and Jaitly, N. (2014). Towards end-to-end speech recognition with recurrent neural networks. In *ICML'2014*.
- Graves, A. and Schmidhuber, J. (2009). Offline handwriting recognition with multidimensional recurrent neural networks. In D. Koller, D. Schuurmans, Y. Bengio, and L. Bottou, editors, *NIPS'2008*, pages 545–552.
- Graves, A., Liwicki, M., Bunke, H., Schmidhuber, J., and Fernández, S. (2008). Unconstrained on-line handwriting recognition with recurrent neural networks. In J. Platt, D. Koller, Y. Singer, and S. Roweis, editors, *NIPS'2007*, pages 577–584.
- Greff, K., Srivastava, R. K., KoutnÃk, J., Steunebrink, B. R., and Schmidhuber, J. (2015). LSTM: a search space odyssey. *arXiv preprint arXiv:1503.04069*.
- Grundmann, M., Kwatra, V., Han, M., and Essa, I. (2010). Efficient hierarchical graph-based video segmentation. In *Computer Vision and Pattern Recognition (CVPR), 2010 IEEE Conference on*, pages 2141–2148. IEEE.

Bibliography

- Gulcehre, C., Moczulski, M., Visin, F., and Bengio, Y. (2016). Mollifying networks. *arXiv preprint arXiv:1608.04980*.
- Hariharan, B., Arbeláez, P., Girshick, R., and Malik, J. (2015a). Hypercolumns for object segmentation and fine-grained localization. In *Computer Vision and Pattern Recognition (CVPR)*.
- Hariharan, B., Arbeláez, P., Girshick, R., and Malik, J. (2015b). Hypercolumns for object segmentation and fine-grained localization. In *Proceedings of the IEEE Conference on Computer Vision and Pattern Recognition*, pages 447–456.
- Harris, C. and Stephens, M. (1988). A combined corner and edge detector. In *Alvey vision conference*, volume 15, page 50. Citeseer.
- Hartigan, J. A. (1975). *Clustering algorithms*.
- He, K., Zhang, X., Ren, S., and Sun, J. (2015). Deep residual learning for image recognition. *arXiv preprint arXiv:1512.03385*.
- He, X., Zemel, R. S., and Carreira-Perpiñán, M. Á. (2004). Multiscale conditional random fields for image labeling. In *Computer vision and pattern recognition, 2004. CVPR 2004. Proceedings of the 2004 IEEE computer society conference on*, volume 2, pages II–695. IEEE.
- Hebb, D. O. (1949). *The Organization of Behavior*. Wiley, New York.
- Hinton, G. E., Srivastava, N., Krizhevsky, A., Sutskever, I., and Salakhutdinov, R. (2012). Improving neural networks by preventing co-adaptation of feature detectors. *arXiv, abs/1207.0580*.
- Ho, T. K. (1995). Random decision forests. In *Document Analysis and Recognition, 1995., Proceedings of the Third International Conference on*, volume 1, pages 278–282. IEEE.
- Hochreiter, S. (1991). Untersuchungen zu dynamischen neuronalen Netzen. Diploma thesis, Institut für Informatik, Lehrstuhl Prof. Brauer, Technische Universität München.
- Hochreiter, S. and Schmidhuber, J. (1997). Long short-term memory. *Neural Computation*, **9**(8), 1735–1780.
- Honari, S., Yosinski, J., Vincent, P., and Pal, C. (2016). Recombinator networks: Learning coarse-to-fine feature aggregation. In *Proceedings of the IEEE Conference on Computer Vision and Pattern Recognition*, pages 5743–5752.
- Huang, G., Sun, Y., Liu, Z., Sedra, D., and Weinberger, K. Q. (2016). Deep networks with stochastic depth. In *European Conference on Computer Vision*, pages 646–661. Springer.
- Im, D. J., Kim, C. D., Jiang, H., and Memisevic, R. (2016). Generating images with recurrent adversarial networks. *arXiv preprint arXiv:1602.05110*.
- Ioffe, S. and Szegedy, C. (2015). Batch normalization: Accelerating deep network training by reducing internal covariate shift.
- Jarrett, K., Kavukcuoglu, K., Ranzato, M., and LeCun, Y. (2009). What is the best multi-stage architecture for object recognition? In *ICCV'09*.
- Karpathy, A. and Li, F.-F. (2015). Deep visual-semantic alignments for generating image descriptions. In *CVPR'2015*. arXiv:1412.2306.

- Karpathy, A., Toderici, G., Shetty, S., Leung, T., Sukthankar, R., and Fei-Fei, L. (2014). Large-scale video classification with convolutional neural networks. In *Proceedings of the IEEE conference on Computer Vision and Pattern Recognition*, pages 1725–1732.
- Kass, M., Witkin, A., and Terzopoulos, D. (1988). Snakes: Active contour models. *International journal of computer vision*, **1**(4), 321–331.
- Kendall, A., Badrinarayanan, V., and Cipolla, R. (2015). Bayesian SegNet: Model Uncertainty in Deep Convolutional Encoder-Decoder Architectures for Scene Understanding.
- Kingma, D. and Ba, J. (2014a). Adam: A method for stochastic optimization. *arXiv preprint arXiv:1412.6980*.
- Kingma, D. P. and Ba, J. (2014b). Adam: A Method for Stochastic Optimization. *arXiv:1412.6980 [cs.LG]*.
- Kingma, D. P. and Welling, M. (2014). Auto-encoding variational bayes. In *Proceedings of the International Conference on Learning Representations (ICLR)*.
- Koutnik, J., Greff, K., Gomez, F., and Schmidhuber, J. (2014). A clockwork RNN. In *ICML’2014*.
- Krizhevsky, A. (2014). One weird trick for parallelizing convolutional neural networks. *arXiv preprint arXiv:1404.5997*.
- Krizhevsky, A. and Hinton, G. (2009). Learning multiple layers of features from tiny images. Technical report, University of Toronto.
- Krizhevsky, A., Sutskever, I., and Hinton, G. E. (2012a). Imagenet classification with deep convolutional neural networks. In *Advances in neural information processing systems*, pages 1097–1105.
- Krizhevsky, A., Sutskever, I., and Hinton, G. E. (2012b). Imagenet classification with deep convolutional neural networks. In *Advances in neural information processing systems*, pages 1097–1105.
- Krizhevsky, A., Sutskever, I., and Hinton, G. E. (2012c). Imagenet classification with deep convolutional neural networks. In F. Pereira, C. J. C. Burges, L. Bottou, and K. Q. Weinberger, editors, *Advances in Neural Information Processing Systems 25*, pages 1097–1105. Curran Associates, Inc.
- Krogh, A. and Hertz, J. A. (1992). A simple weight decay can improve generalization. In *ADVANCES IN NEURAL INFORMATION PROCESSING SYSTEMS 4*, pages 950–957. Morgan Kaufmann.
- Kundu, A., Vineet, V., and Koltun, V. (2016). Feature space optimization for semantic video segmentation. *CVPR*.
- Ladický, L., Sturges, P., Alahari, K., Russell, C., and Torr, P. H. S. (2010). What, where and how many? Combining object detectors and CRFs. *Lecture Notes in Computer Science (including subseries Lecture Notes in Artificial Intelligence and Lecture Notes in Bioinformatics)*, **6314 LNCS(PART 4)**, 424–437.
- Laurent, C., Pereyra, G., Brakel, P., Zhang, Y., and Bengio, Y. (2015). Batch normalized recurrent neural networks. *CoRR*, **abs/1510.01378**.
- Le Cun, Y., Bottou, L., and Bengio, Y. (1997). Reading checks with multilayer graph transformer networks. In *Acoustics, Speech, and Signal Processing, 1997. ICASSP-97., 1997 IEEE International Conference on*, volume 1, pages 151–154. IEEE.

Bibliography

- LeCun, Y., Boser, B., Denker, J. S., Henderson, D., Howard, R. E., Hubbard, W., and Jackel, L. D. (1989). Backpropagation applied to handwritten zip code recognition. *Neural Computation*, **1**(4), 541–551.
- LeCun, Y., Haffner, P., Bottou, L., and Bengio, Y. (1999). Object recognition with gradient-based learning. In *Shape, Contour and Grouping in Computer Vision*, pages 319–345. Springer.
- LeCun, Y., Bengio, Y., and Hinton, G. (2015). Deep learning. *Nature*, **521**, 436–444.
- Lee, C., Xie, S., Gallagher, P., Zhang, Z., and Tu, Z. (2014). Deeply-supervised nets. *arXiv*, [abs/1409.5185](#).
- Leutenegger, S., Chli, M., and Siegwart, R. Y. (2011). Brisk: Binary robust invariant scalable keypoints. In *2011 International conference on computer vision*, pages 2548–2555. IEEE.
- Lin, M., Chen, Q., and Yan, S. (2014a). Network in network. In *Proceedings of the Second International Conference on Learning Representations (ICLR 2014)*.
- Lin, T.-Y., Maire, M., Belongie, S., Hays, J., Perona, P., Ramanan, D., Dollár, P., and Zitnick, C. L. (2014b). Microsoft coco: Common objects in context. In *European Conference on Computer Vision*, pages 740–755. Springer.
- Linnainmaa, S. (1970). *The representation of the cumulative rounding error of an algorithm as a Taylor expansion of the local rounding errors*. Master’s thesis, Univ. Helsinki.
- Liu, F., Lin, G., and Shen, C. (2015a). Crf learning with cnn features for image segmentation. *Pattern Recognition*.
- Liu, W., Rabinovich, A., and Berg, A. C. (2015b). Parsenet: Looking wider to see better. *arXiv preprint arXiv:1506.04579*.
- Long, J., Shelhamer, E., and Darrell, T. (2015a). Fully convolutional networks for semantic segmentation. In *Proceedings of the IEEE Conference on Computer Vision and Pattern Recognition*, pages 3431–3440.
- Long, J., Shelhamer, E., and Darrell, T. (2015b). Fully convolutional networks for semantic segmentation. *CVPR (to appear)*.
- Lowe, D. G. (1999). Object recognition from local scale-invariant features. In *Computer vision, 1999. The proceedings of the seventh IEEE international conference on*, volume 2, pages 1150–1157. Ieee.
- Lowe, D. G. (2004). Distinctive image features from scale-invariant keypoints. *International journal of computer vision*, **60**(2), 91–110.
- Ma, H., Mao, F., and Taylor, G. W. (2016). Theano-mpi: a theano-based distributed training framework. *arXiv preprint arXiv:1605.08325*.
- Mahjourian, R., Wicke, M., and Angelova, A. (2016). Geometry-based next frame prediction from monocular video. *arXiv preprint arXiv:1609.06377*.
- Mairal, J., Koniusz, P., Harchaoui, Z., and Schmid, C. (2014). Convolutional kernel networks. In *Advances in Neural Information Processing Systems 27: Annual Conference on Neural Information Processing Systems 2014, December 8-13 2014, Montreal, Quebec, Canada*, pages 2627–2635.

- Märki, N., Perazzi, F., Wang, O., and Sorkine-Hornung, A. (2016). Bilateral space video segmentation. In *Proceedings of the IEEE Conference on Computer Vision and Pattern Recognition*, pages 743–751.
- Martens, J. and Sutskever, I. (2011). Learning recurrent neural networks with Hessian-free optimization. In *Proc. ICML'2011*. ACM.
- McCulloch, W. S. and Pitts, W. (1943). A logical calculus of ideas immanent in nervous activity. *The bulletin of mathematical biophysics*, **5**, 115–133.
- Mikolajczyk, K. and Schmid, C. (2001). Indexing based on scale invariant interest points. In *Computer Vision, 2001. ICCV 2001. Proceedings. Eighth IEEE International Conference on*, volume 1, pages 525–531. IEEE.
- Mikolajczyk, K. and Schmid, C. (2005). A performance evaluation of local descriptors. *IEEE transactions on pattern analysis and machine intelligence*, **27**(10), 1615–1630.
- Mikolov, T. (2012). *Statistical Language Models based on Neural Networks*. Ph.D. thesis, Brno University of Technology.
- Minsky, M. L. and Papert, S. A. (1969). *Perceptrons*. MIT Press, Cambridge.
- Moser, G., Serpico, S. B., and Benediktsson, J. A. (2012). Markov random field models for supervised land cover classification from very high resolution multispectral remote sensing images. In *Advances in Radar and Remote Sensing (TyWRRS), 2012 Tyrrhenian Workshop on*, pages 235–242. IEEE.
- Murphy, K. P. (2012). *Machine Learning: a Probabilistic Perspective*. MIT Press, Cambridge, MA, USA.
- Nair, V. and Hinton, G. E. (2010). Rectified linear units improve restricted Boltzmann machines. In *Proc. 27th International Conference on Machine Learning*.
- Netzer, Y., Wang, T., Coates, A., Bissacco, A., Wu, B., and Ng, A. Y. (2011). Reading digits in natural images with unsupervised feature learning. Deep Learning and Unsupervised Feature Learning Workshop, NIPS.
- Nilsback, M.-E. and Zisserman, A. (2006). A visual vocabulary for flower classification. In *Proceedings of the IEEE Conference on Computer Vision and Pattern Recognition*, volume 2, pages 1447–1454.
- Noh, H., Hong, S., and Han, B. (2015). Learning deconvolution network for semantic segmentation. *arXiv preprint arXiv:1505.04366*.
- Olah, C. (2015). Understanding lstm networks. <http://colah.github.io/posts/2015-08-Understanding-LSTMs/>.
- Pascanu, R., Mikolov, T., and Bengio, Y. (2013). On the difficulty of training recurrent neural networks. In *ICML'2013*.
- Pascanu, R., Gulcehre, C., Cho, K., and Bengio, Y. (2014). How to construct deep recurrent neural networks. In *ICLR*.
- Perazzi, F., Wang, O., Gross, M., and Sorkine-Hornung, A. (2015). Fully connected object proposals for video segmentation. In *Proceedings of the IEEE International Conference on Computer Vision*, pages 3227–3234.

Bibliography

- Perazzi, F., Pont-Tuset, J., McWilliams, B., Gool, L. V., Gross, M., and Sorkine-Hornung, A. (2016). A benchmark dataset and evaluation methodology for video object segmentation. In *Computer Vision and Pattern Recognition*.
- Pinheiro, P. and Collobert, R. (2014). Recurrent convolutional neural networks for scene labeling. *JMLR*, **1**(32), 82–90.
- Radford, A., Metz, L., and Chintala, S. (2015). Unsupervised representation learning with deep convolutional generative adversarial networks. *arXiv preprint arXiv:1511.06434*.
- Ramakanth, S. A. and Babu, R. V. (2014). Seamseg: Video object segmentation using patch seams. In *2014 IEEE Conference on Computer Vision and Pattern Recognition*, pages 376–383. IEEE.
- Raza, S. H., Grundmann, M., and Essa, I. (2013). Geometric context from video. In *IEEE Conference on Computer Vision and Pattern Recognition*.
- Roerdink, J. B. and Meijster, A. (2000). The watershed transform: Definitions, algorithms and parallelization strategies. *Fundamenta informaticae*, **41**(1, 2), 187–228.
- Ronneberger, O., P.Fischer, and Brox, T. (2015). U-net: Convolutional networks for biomedical image segmentation. In *Medical Image Computing and Computer-Assisted Intervention (MICCAI)*, volume 9351 of *LNCS*, pages 234–241. Springer. (available on arXiv:1505.04597 [cs.CV]).
- Rosenblatt, F. (1957). The perceptron — a perceiving and recognizing automaton. Technical Report 85-460-1, Cornell Aeronautical Laboratory, Ithaca, N.Y.
- Rother, C., Kolmogorov, V., and Blake, A. (2004). Grabcut: Interactive foreground extraction using iterated graph cuts. *ACM Transactions on Graphics (TOG)*, **23**(3), 309–314.
- Rumelhart, D. E., Hinton, G. E., and Williams, R. J. (1986a). Learning representations by back-propagating errors. *Nature*, **323**, 533–536.
- Rumelhart, D. E., Hinton, G. E., and Williams, R. J. (1986b). Learning representations by back-propagating errors. *Nature*, **323**(6088), 533–536.
- Russakovsky, O., Deng, J., Su, H., Krause, J., Satheesh, S., Ma, S., Huang, Z., Karpathy, A., Khosla, A., Bernstein, M., Berg, A. C., and Fei-Fei, L. (2014). ImageNet Large Scale Visual Recognition Challenge.
- Russell, C., Kohli, P., Torr, P. H., et al. (2009). Associative hierarchical crfs for object class image segmentation. In *2009 IEEE 12th International Conference on Computer Vision*, pages 739–746. IEEE.
- Sainath, T. N., Mohamed, A.-r., Kingsbury, B., and Ramabhadran, B. (2013). Deep convolutional neural networks for lvcsr. In *Acoustics, Speech and Signal Processing (ICASSP), 2013 IEEE International Conference on*, pages 8614–8618. IEEE.
- Sainath, T. N., Vinyals, O., Senior, A., and Sak, H. (2015). Convolutional, long short-term memory, fully connected deep neural networks. In *Acoustics, Speech and Signal Processing (ICASSP), 2015 IEEE International Conference on*.
- Saxe, A., Koh, P. W., Chen, Z., Bhand, M., Suresh, B., and Ng, A. (2011). On random weights and unsupervised feature learning. In L. Getoor and T. Scheffer, editors, *Proceedings of the 28th International Conference on Machine Learning (ICML-11)*, ICML '11, pages 1089–1096, New York, NY, USA. ACM.

- Saxe, A. M., McClelland, J. L., and Ganguli, S. (2014). Exact solutions to the nonlinear dynamics of learning in deep linear neural networks. In *Proceedings of the Second International Conference on Learning Representations (ICLR 2014)*.
- Schuster, M. and Paliwal, K. (1997). Bidirectional recurrent neural networks. *Trans. Sig. Proc.*, **45**(11), 2673–2681.
- Sermanet, P., Eigen, D., Zhang, X., Mathieu, M., Fergus, R., and LeCun, Y. (2013a). Overfeat: Integrated recognition, localization and detection using convolutional networks. *CoRR*, **abs/1312.6229**.
- Sermanet, P., Kavukcuoglu, K., Chintala, S., and LeCun, Y. (2013b). Pedestrian detection with unsupervised multi-stage feature learning. In *Proc. International Conference on Computer Vision and Pattern Recognition (CVPR'13)*. IEEE.
- Sermanet, P., Eigen, D., Zhang, X., Mathieu, M., Fergus, R., and LeCun, Y. (2014). Overfeat: Integrated recognition, localization and detection using convolutional networks. *International Conference on Learning Representations*.
- Shi, X., Chen, Z., Wang, H., Yeung, D., Wong, W., and Woo, W. (2015). Convolutional LSTM network: A machine learning approach for precipitation nowcasting. *CoRR*, **abs/1506.04214**.
- Shlens, J. (2014). A tutorial on principal component analysis. *arXiv preprint arXiv:1404.1100*.
- Shotton, J., Winn, J., Rother, C., and Criminisi, A. (2006). Textonboost: Joint appearance, shape and context modeling for multi-class object recognition and segmentation. In *European conference on computer vision*, pages 1–15. Springer.
- Shotton, J., Johnson, M., and Cipolla, R. (2008). Semantic texton forests for image categorization and segmentation. In *Computer vision and pattern recognition, 2008. CVPR 2008. IEEE Conference on*, pages 1–8. IEEE.
- Silver, D. and Hassabis, D. (2016). Alphago: Mastering the ancient game of go with machine learning. *Research Blog*.
- Simard, P. Y., Steinkraus, D., and Platt, J. C. (2003). Best practices for convolutional neural networks applied to visual document analysis. In *7th International Conference on Document Analysis and Recognition (ICDAR 2003), 2-Volume Set, 3-6 August 2003, Edinburgh, Scotland, UK*, pages 958–962.
- Simonyan, K. and Zisserman, A. (2014a). Two-stream convolutional networks for action recognition in videos. In *Advances in Neural Information Processing Systems*, pages 568–576.
- Simonyan, K. and Zisserman, A. (2014b). Very deep convolutional networks for large-scale image recognition. *CoRR*, **abs/1409.1556**.
- Simonyan, K. and Zisserman, A. (2015). Very deep convolutional networks for large-scale image recognition. In *ICLR*.
- Singh, G. and Kosecka, J. (2013). Nonparametric scene parsing with adaptive feature relevance and semantic context. In *2013 IEEE Conference on Computer Vision and Pattern Recognition, Portland, OR, USA, June 23-28, 2013*, pages 3151–3157.
- Smith, L. I. (2002). A tutorial on principal components analysis. *Cornell University, USA*, **51**, 52.

Bibliography

- Snoek, J., Larochelle, H., and Adams, R. P. (2012). Practical bayesian optimization of machine learning algorithms. In *Advances in Neural Information Processing Systems 25: 26th Annual Conference on Neural Information Processing Systems 2012. Proceedings of a meeting held December 3-6, 2012, Lake Tahoe, Nevada, United States.*, pages 2960–2968.
- Springenberg, J. T. and Riedmiller, M. A. (2013). Improving deep neural networks with probabilistic maxout units. *arXiv*, **abs/1312.6116**.
- Springenberg, J. T., Dosovitskiy, A., Brox, T., and Riedmiller, M. (2014). Striving for simplicity: The all convolutional net. *arXiv preprint arXiv:1412.6806*.
- Srivastava, N., Hinton, G., Krizhevsky, A., Sutskever, I., and Salakhutdinov, R. (2014). Dropout: A simple way to prevent neural networks from overfitting. *Journal of Machine Learning Research*, **15**, 1929–1958.
- Srivastava, N., Mansimov, E., and Salakhutdinov, R. (2015a). Unsupervised learning of video representations using lstms. *CoRR*, **abs/1502.04681**, **2**.
- Srivastava, R. K., Greff, K., and Schmidhuber, J. (2015b). Highway networks. *arXiv:1505.00387*.
- Srivastava, R. K., Greff, K., and Schmidhuber, J. (2015c). Training very deep networks. In *Advances in neural information processing systems*, pages 2377–2385.
- Stollenga, M. F., Byeon, W., Liwicki, M., and Schmidhuber, J. (2015). Parallel multi-dimensional lstm, with application to fast biomedical volumetric image segmentation. In *Advances in Neural Information Processing Systems*, pages 2980–2988.
- Sturges, P., Alahari, K., Ladicky, L., and Torr, P. H. S. (2009). Combining Appearance and Structure from Motion Features for Road Scene Understanding. *Proceedings of the British Machine Vision Conference 2009*, pages 62.1–62.11.
- Sutskever, I., Vinyals, O., and Le, Q. V. (2014). Sequence to sequence learning with neural networks. In *NIPS'2014*.
- Szegedy, C., Liu, W., Jia, Y., Sermanet, P., Reed, S., Anguelov, D., Erhan, D., Vanhoucke, V., and Rabinovich, A. (2014a). Going deeper with convolutions. *arXiv preprint arXiv:1409.4842*.
- Szegedy, C., Liu, W., Jia, Y., Sermanet, P., Reed, S., Anguelov, D., Erhan, D., Vanhoucke, V., and Rabinovich, A. (2014b). Going deeper with convolutions. Technical report, arXiv:1409.4842.
- Szegedy, C., Liu, W., Jia, Y., Sermanet, P., Reed, S. E., Anguelov, D., Erhan, D., Vanhoucke, V., and Rabinovich, A. (2015). Going deeper with convolutions. In *IEEE Conference on Computer Vision and Pattern Recognition*, pages 1–9.
- Szegedy, C., Ioffe, S., and Vanhoucke, V. (2016). Inception-v4, inception-resnet and the impact of residual connections on learning. *arXiv preprint arXiv:1602.07261*.
- Theano Development Team (2016). Theano: A Python framework for fast computation of mathematical expressions. *arXiv e-prints*, **abs/1605.02688**.
- Thoma, M. (2016). A survey of semantic segmentation. *arXiv preprint arXiv:1602.06541*.
- Tieleman, T. and Hinton, G. (2012). Lecture 6.5-rmsprop: Divide the gradient by a running average of its recent magnitude. *COURSERA: Neural Networks for Machine Learning*, **4**.

- Tighe, J. and Lazebnik, S. (2013). Superparsing: Scalable nonparametric image parsing with superpixels. *International Journal of Computer Vision*, **101**(2), 329–349.
- Torralba, A., Fergus, R., and Freeman, W. T. (2008). 80 million tiny images: A large dataset for non-parametric object and scene recognition. *IEEE Transactions on Pattern Analysis and Machine Intelligence*, **30**(11), 1958–1970.
- Tóth, L. (2014). Combining time-and frequency-domain convolution in convolutional neural network-based phone recognition. In *Acoustics, Speech and Signal Processing (ICASSP), 2014 IEEE International Conference on*, pages 190–194. IEEE.
- Tran, D., Bourdev, L. D., Fergus, R., Torresani, L., and Paluri, M. (2015). Deep end2end voxel2voxel prediction. *CoRR*, **abs/1511.06681**.
- Venugopalan, S., Rohrbach, M., Donahue, J., Mooney, R., Darrell, T., and Saenko, K. (2015). Sequence to sequence - video to text. In *The IEEE International Conference on Computer Vision (ICCV)*.
- Vinyals, O., Toshev, A., Bengio, S., and Erhan, D. (2014). Show and tell: a neural image caption generator. arXiv 1411.4555.
- Vinyals, O., Toshev, A., Bengio, S., and Erhan, D. (2015). Show and tell: a neural image caption generator. In *CVPR’2015*. arXiv:1411.4555.
- Visin, F., Kastner, K., Cho, K., Matteucci, M., Courville, A., and Bengio, Y. (2015). Renet: A recurrent neural network based alternative to convolutional networks. *arXiv preprint arXiv:1505.00393*.
- Visin, F., Ciccone, M., Romero, A., Kastner, K., Cho, K., Bengio, Y., Matteucci, M., and Courville, A. (2016). Reseg: A recurrent neural network-based model for semantic segmentation. In *The IEEE Conference on Computer Vision and Pattern Recognition (CVPR) Workshops*.
- Wan, L., Zeiler, M. D., Zhang, S., LeCun, Y., and Fergus, R. (2013). Regularization of neural networks using dropconnect. In *Proceedings of the 30th International Conference on Machine Learning, ICML 2013, Atlanta, GA, USA, 16-21 June 2013*, pages 1058–1066.
- Werbos, P. (1974). *Beyond Regression: New Tools for Prediction and Analysis in the Behavioral Sciences*. Ph.D. thesis, Harvard University.
- Wu, X. and Kashino, K. (2014). Tri-map self-validation based on least gibbs energy for foreground segmentation. In *Proceedings of the British Machine Vision Conference*. BMVA Press.
- Xingjian, S., Chen, Z., Wang, H., Yeung, D.-Y., Wong, W.-k., and Woo, W.-c. (2015). Convolutional lstm network: A machine learning approach for precipitation nowcasting. In *Advances in Neural Information Processing Systems*, pages 802–810.
- Xu, K., Ba, J. L., Kiros, R., Cho, K., Courville, A., Salakhutdinov, R., Zemel, R. S., and Bengio, Y. (2015). Show, attend and tell: Neural image caption generation with visual attention. arXiv:1502.03044.
- Yan, Z., Zhang, H., Jia, Y., Breuel, T., and Yu, Y. (2016). Combining the best of convolutional layers and recurrent layers: A hybrid network for semantic segmentation. *CoRR*, **abs/1603.04871**.
- Yang, J., Price, B., Cohen, S., Lin, Z., and Yang, M.-H. (2015). Patchcut: Data-driven object segmentation via local shape transfer. In *Proceedings of the IEEE Conference on Computer Vision and Pattern Recognition*, pages 1770–1778.

Bibliography

- Yang, Y., Hallman, S., Ramanan, D., and Fowlkes, C. C. (2012). Layered object models for image segmentation. *IEEE Transactions on Pattern Analysis and Machine Intelligence*, **34**(9), 1731–1743.
- Yao, L., Torabi, A., Cho, K., Ballas, N., Pal, C., Larochelle, H., and Courville, A. (2015a). Describing videos by exploiting temporal structure. In *Proceedings of the IEEE International Conference on Computer Vision*, pages 4507–4515.
- Yao, L., Torabi, A., Cho, K., Ballas, N., Pal, C., Larochelle, H., and Courville, A. (2015b). Video description generation incorporating spatio-temporal features and a soft-attention mechanism. *arXiv:1502.08029*.
- Yeung, S., Russakovsky, O., Mori, G., and Fei-Fei, L. (2015). End-to-end learning of action detection from frame glimpses in videos. *arXiv preprint arXiv:1511.06984*.
- Yu, F. and Koltun, V. (2015). Multi-scale context aggregation by dilated convolutions. *arXiv preprint arXiv:1511.07122*.
- Zeiler, M., Taylor, G., and Fergus, R. (2011a). Adaptive deconvolutional networks for mid and high level feature learning. In *Proc. International Conference on Computer Vision (ICCV'11)*, pages 2146–2153. IEEE.
- Zeiler, M. D. (2012). ADADELTA: an adaptive learning rate method. Technical report, arXiv 1212.5701.
- Zeiler, M. D. and Fergus, R. (2013). Stochastic pooling for regularization of deep convolutional neural networks. *arXiv, abs/1301.3557*.
- Zeiler, M. D. and Fergus, R. (2014a). Visualizing and understanding convolutional networks. In *Computer vision–ECCV 2014*, pages 818–833. Springer.
- Zeiler, M. D. and Fergus, R. (2014b). Visualizing and understanding convolutional networks. In *ECCV'14*.
- Zeiler, M. D., Taylor, G. W., and Fergus, R. (2011b). Adaptive deconvolutional networks for mid and high level feature learning. In *Computer Vision (ICCV), 2011 IEEE International Conference on*, pages 2018–2025. IEEE.